NMR-BASED MICROPROBES FOR MAGNETIC FIELD MEASUREMENTS

by

Philip Peter Unger

A thesis submitted to the Faculty of Graduate Studies
in partial fulfillment of the requirements for the degree
of

Ph. D

Department of Physics
University of Manitoba
Winnipeg, Manitoba

THE UNIVERSITY OF MANITOBA

FACULTY OF GRADUATE STUDIES

*****

COPYRIGHT PERMISSION

NMR-BASED MICROPROBES FOR MAGNETIC FIELD MEASUREMENTS

BY

PHILIP PETER UNGER

A Thesis/Practicum submitted to the Faculty of Graduate Studies of The University of Manitoba in partial fulfillment of the requirement of the degree

of

DOCTOR OF PHILOSOPHY

University of Manitoba

Abstract

NMR-BASED MICROPROBES FOR MAGNETIC FIELD MEASUREMENTS

by Philip Peter Unger

Chairperson of the Supervisory Committee: Dr. D. I. Hoult
Adjunct Professor, Department of Physics

The thesis considers the problem of measuring magnetic fields to high accuracy using the preferred method of nuclear magnetic resonance (NMR). In chapter one, a brief summary of diverse methods of field measurement is given, and the basic principles of NMR spectroscopy are explained, concentrating on the topics of signal reception, relaxation, line width and magnetic field inhomogeneity. In chapter two, the use of a microprobe for highly-localised NMR measurements of field strength is introduced. Perturbations to the field by the probe, that destroy the accuracy of the measurements, are analysed and the contributions of the various probe components to this problem are discussed. In chapter three, an initial, simple probe design is presented that exploits the symmetries inherent in a description of static magnetic fields to minimise field perturbations. The loss of signal-to-noise ratio associated with the design – long wires parallel to the field direction – is discussed and experimental results are presented that validate the concept. The venerable use of zero-susceptibility wire, with a coaxial structure of metals of opposite magnetic susceptibility, is introduced in chapter four, and the simple first-order recipe, currently used by manufacturers to determine the relative thicknesses of metals, is derived. Deficiencies in current methods of producing such wire are also highlighted. The novel manufacture of zero-susceptibility, copper-plated aluminium conductor is then described in detail. This particular combination of metals is shown to be advantageous and measurements on a long sample confirmed the advantage. However, results obtained with a probe constructed of such wire were mediocre, as described in chapter five, and suspicion is directed toward the simplistic theory currently used. A summary and references conclude the thesis.

TABLE OF CONTENTS

Abstract			i
Acknowledgements			iv
List of Figures			vi
List of Tables			viii
List of Symbols Used			ix
1	Introduction		
	1.1	Motivation and major objectives	1
	1.2	Magnetic field measurement technologies	2
	1.3	NMR as a magnetic field measurement technology	3
	1.4	The NMR experiment	4
	1.5	Description and correction of the base magnetic field	23
	1.6	Chapter Summary	30
2	Micro-Probe Basics		
	2.1	Introduction	32
	2.2	Theory of operation.	32
	2.3	Magnetostatic description	38
	2.4	Chapter Summary	52
3	Probe Design 1. The Aligned Straight Wire		
	3.1	Introduction	54
	3.2	Theory	57
	3.3	Microprobe construction	65
	3.4	NMR experiments	70
	3.5	Chapter Summary	84
4	Probe Design 2. Susceptibility Compensated Wire and the "Hairpin" Loop		
	4.1	Introduction	86
	4.2	Theory	89
	4.3	Manufacture of the wire	100
	4.4	Wire Testing	119
	4.5	Chapter Summary	147
5	Probe Design 3. A Solenoid Winding		
	5.1	Introduction	148
	5.2	Theory	148
	5.3	Microprobe construction	157
	5.4	NMR experiments	159
	5.5	Chapter summary	163
6	Conclusion		165
Bibliography			169

ACKNOWLEDGMENTS

I am grateful to my research supervisor, Dr. David Hoult for introducing me to this interesting research topic and for imparting MR knowledge. I would also like to thank Dr. Piotr Kozlowski (formerly of NRC-Winnipeg). They have both been essential guides for my training on the MR spectrometer.

A large part of this thesis was spent learning the "art" of electroplating. Since most of the knowledge in this field is held within industry, I was starved at times for the knowledge to interpret my electroplating results and plan the next batch of experiments. In this regard, I would like to thank Dr. John Rendell of NRC-Winnipeg for discussions relating to the electroplating process as well as NMR spectroscopy in general. Mr. Bob Chalut and Mr. Jonathan Holland of Enthone-OMI in Toronto provided advice on the use of the commercial electroplating additives that made the plating of copper on high purity aluminium possible. I would also like to thank Mr. Rick Chipindate of The Chrome Pit in Winnipeg for his practical advice on electroplating on aluminium.

Some of the curious results I encountered while electroplating led me to Drs. Doug Thomson (surface phenomenon) and Jack Calhoon (metallurgy including diffusion, phase diagrams and extrusion) at the University of Manitoba, Faculty of Engineering. I appreciate their advice and access to equipment (including the hydrofluoric acid work station). It was a great learning experience.

In the Department of Physics at the University of Manitoba, I wish to acknowledge the help of Mr. Gilles Roy with a series of experiments to vapour plate copper onto aluminium.

I would also like to thank several senior scientists that I met after presenting some of my successful electroplating and related NMR results in Orlando (ENC 1997) and Vancouver (ISMRM 1997) for their advice and encouragement. My first contacts were with Drs. Weston Anderson and Howard Hill, of Varian NMR Systems. Shortly after these initial contacts, Mr. Tom Barbara of Varian sent me a sample length of the zero susceptibility wire that was used to wind their present-day coils. Dr. Bill Edelstein of General Electric Corporate R&D kindly sent me some photocopies from his research logbook on zero susceptibility materials and a sample of zero-susceptibility foil that was produced at GE.

Returning to NRC in Winnipeg, I would like to acknowledge the support of Mr. Tony Wessel for his help in the electronics and machine shop and Mr. Rudy Sebastian for his help with computing resources as well as technical help on the spectrometers. I would also like to thank the NRC library staff at the Canada Institute for Scientific and Technical Information (CISTI). The CISTI library is a students' dream, and allowed me to retrieve documents that simply would have been out of reach by any other practical means. Lastly at NRC, my thanks to the group leaders of the MR Technology Group. They are (in order of present to past during my time in the group), Dr. Boguslaw Tomanek, Dr. Piotr Kozlowski, and Dr. John Saunders. I have appreciated their financial and scientific support.

Saving the best for last, I wish to thank my parents, Agnes and Bill, who have always supported my efforts in higher education. Their encouragement has never wavered through the years of this project. This thesis is dedicated to the memories of my father Peter, and my sister Jacquie.

LIST OF FIGURES

Number *Page*

Fig. 1.1. NMR system diagram 21
Fig. 1.2. Magnetic field plotting coordinate system 27
Fig. 2.1. Schematic drawing of the NMR probe used in all experiments 33
Fig. 2.2. Cross-section of a cylinder 42
Fig. 2.3. Cross section of a co-axial cylinder 42
Fig. 2.4. Multi-layer chip capacitor used in all probes in this work 48
Fig. 2.5. Geometry of the NMR probe used to test susceptibility of the chip capacitors. 50
Fig. 2.6. Fourier transforms for two different test capacitor positions. 51
Fig. 2.7. Spectral data analyzed to obtain the integral width plotted against the position. 52
Fig. 3.1. Basic principle of the aligned parallel probe.. 55
Fig. 3.2. RF coil shapes used in the aligned parallel probe design. 57
Fig. 3.3. The equivalent surface current density 59
Fig. 3.4. NMR probe based on the magnetostatic properties of the aligned straight wire. 61
Fig. 3.5. $\mathbf{B}_1$ field from a pair of current carrying long straight wire 62
Fig. 3.6. Photograph of the long wire version of the aligned wire probe 62
Fig. 3.7. NMR spectra resulting from RF coil design. Fig. 3.2(a) 80
Fig. 3.8. NMR spectra resulting from RF coil design. Fig. 3.2(b) 82
Fig. 3.9. NMR spectra resulting from RF coil design Fig. 3.2(c). 83
Fig. 4.1. Cross-section of a co-axial long wire 88
Fig. 4.2. Hairpin loop RF coil 88
Fig. 4.3. Effective susceptibility of a coaxial wire 90
Fig. 4.4. Diffusion of of metals pairs. 95
Fig. 4.5. Photograph of the apparatus for the electroplating experiments.. 102
Fig. 4.7. A photograph of the arrangement for plating in separate bath stations 103
Fig. 4.8. Constant current supply. 104
Fig. 4.9. First results of electroplating copper from a copper sulphate bath 106
Fig. 4.10. Photograph of the zinc immersion plating station 107
Fig. 4.11. Results from zinc plating in a zinc immersion solution 108
Fig. 4.12. Acid-based copper electroplating results. 109
Fig. 4.13. Electroplating results for 0.5mm diameter aluminium wires 110
Fig. 4.14. Variation of surface appearance for different plating substrates. 114
Fig. 4.15. Plating results from pulse plating experiments. 115
Fig. 4.16. An example of a finished solenoid winding made with copper plated wire 116
Fig. 4.17. Photograph of the bending involved in the test of ductility for finished wires. 119
Fig. 4.18. Photograph of the special NMR probe used to test susceptibility 120
Fig. 4.19. Schematic drawing of the special NMR probe 121
Fig. 4.20. Cross-section of the wire pair in the y-z plane 123
Fig. 4.21. Field points positions for the magnetostatic calculations. 124

Fig. 4.23. Sample spectra from the computer simulation. 127
Fig. 4.24. $B_{1,r}$=0 curves for the computer-simulated spectrum. 129
Fig. 4.25. Demonstration spectra for a water sample in the special NMR test probe 132
Fig. 4.26. Predicted and experimental Integral Width versus Wire Diameter 134
Fig. 4.27. Test results plotting the observed effect of transmit power to the probe 136
Fig. 4.28. Fourier transforms of the free induction decays 137
Fig. 4.29. Data from Table 4.3 plotted with the least-squares fit of Table 4.5 141
Fig. 4.30. Photograph showing the placement of the wire under test. 145
Fig. 4.31. Water spectra at 400MHz from the probe of Fig. 4.30 146
Fig. 5.1. Toroidal coordinate system 149
Fig. 5.2. Two cross sections based on the ring in Fig. 5.1 151
Fig. 5.3. Coefficients from Eq. **(5.15)** and Eq. **(5.16)** 156
Fig. 5.4. Winding geometry for a solenoidal coil.. 157
Fig. 5.5. Installation of the 4-turn solenoid into the special NMR probe 159
Fig. 5.6. Four-turn solenoid coil results 160

LIST OF TABLES

Number *Page*
Table 1.1. Legendre and Associated Legendre functions 26
Table 1.2. Magnetic field plotting coordinates. 28
Table 2.3. Capillary tubes used in this work. 37
Table 3.1. Coil design summary for RF coils based on the aligned parallel wire 69
Table 3.2. Calculated spherical harmonic values for the 9.4T imaging magnet 72
Table 3.3. Matrix representation of the effect of individual shim windings 73
Table 3.4. Aligned straight wire probe linewidth results. 77
Table 4.1. Diffusion-time calculations for diffusion in copper, aluminium, and zinc 96
Table 4.2. Approximate Temperature Coefficients of Volumetric Magnetic Susceptibility 98
Table 4.3. Data from the susceptibility testing experiments 131
Table 4.4. Flip angle and integrated width data. 135
Table 4.5. Least squares parameters, definitions, and values for a weighted fit 140
Table 4.6. Least squares parameters, definitions, and values for a weighted fit. 144
Table 5.1. Solenoid coils experimental results. 161
Table 6.1. Review of probe performance results 167

LIST OF SYMBOLS USED

$\boldsymbol{\alpha}$	curvature matrix
α_e	equivalent surface current density
$\mathbf{B}, \mathbf{H}$	magnetic B and H fields
$\mathbf{B}_0$	static magnetic field of the NMR experiment
B_1	radio frequency magnetic field
χ	volumetric magnetic susceptibility
χ^2, χ^2_ν	chi-squared, reduced chi-squared
C	capacitance
d	coil diameter
D_0	frequency factor
δ	skin depth
$\hat{e}$	unit vector
$\mathbf{E}$	electric field
$\boldsymbol{\epsilon}$	error matrix
ϵ_m	Neumann factor
$\mathscr{E}$, *emf*	electromotive force
ζ	proximity factor
f	frequency
FWHM	full width at half maximum
FID	free induction decay
$\mathbf{F}$	analysed field harmonic set
γ'_p, γ_-	shielded proton gyromagnetic ratio
g	conductivity
h	coil length
H	Fourier transform of the $S(t)$
I	nuclear spin
i	current
$\mathbf{I}$	shim set winding current
$\mathbf{J}_f$	free current density
k_B	Boltzmann constant
L	inductance
$\mathbf{m}$	average dipole moment per atom
$\mathbf{M}_0, M_z$	magnetization or magnetic moment per unit volume
N	number of protons per unit volume
$\boldsymbol{\Phi}$	magnetic scalar potential
ppm	part per million
ppb	part per billion
p	circumference
P_{nm}	Ferrer's associated Legendre polynomial

Q	quality factor
R	resistance
R_{coil}	resistive coil losses
$S(t)$	NMR signal
SNR	signal-to-noise ratio
$\mathbf{S}$	shim matrix
T	temperture
t	time
T_1	longitudinal relaxation
T_2	transverse relaxation
U	potential energy
μ	permeability
μ_0	permeability of free space
μ_I	proton magnetic moment
ΔV	volume
ω	angular frequency
w	weight function
Y_{nm}	spherical harmonics
Z	impedance

Diffusion symbols

D	diffusion concentration
E	energy
$\mathbf{J}_N$	net flux of atom
$\hat{\mathbf{n}}$	normal unit vector

Electroplating symbols

e	electronic charge
I	current
J	current density
M	molar mass
N	number of atoms per unit volume
N_A	Avagadro's number
ρ	density
Q	charge, or number of electrons
V	volume
z	valence number

Chapter 1

INTRODUCTION

1.1 Motivation and major objectives

The work described in this thesis was born of a desire to measure transient ($\sim 10^{-2}$ s) artefacts in the field of a magnetic-resonance-imaging superconducting magnet during switching of magnetic field gradients. Stated briefly, thanks to induced eddy current in the magnet cyrostat, the field in such magnets can vary both in absolute value and in homogeneity following application of a field gradient. To map both the spatial and temporal variations of such disturbances, an array of small nuclear magnetic resonance (NMR) probes was envisaged. To function satisfactorily, a tentative specification for resolution and SNR available from such probes was established by my supervisor and the thesis details efforts to attain these specifications. The detailed functioning of a magnetic resonance imaging device is beyond the scope of this thesis; interested readers may consult a large number of texts, both popular and detailed, that are readily available. (For example, (Callaghan 1991; Ernst, Bodenhausen et al. 1992; Slichter 1992; Hill 1996).)

The major specifications set out at the start of the thesis were the following: Develop a NMR-based microprobe for magnetic field measurements such that;

1. The measurement resolution exceeds 2.5 parts per billion (ppb) relative accuracy,
2. The signal-to-noise ratio (SNR) exceeds 1000:1,

3. The probe should be suitable for use in both homogeneous and inhomogeneous magnetic fields.

The material that is within the scope of the thesis therefore, is how an NMR-based probe works and the efforts made to meet the above specifications. Thus, later in this chapter, there is a description of the NMR experiment, followed by a description of the experimental conditions, specifically the magnetic field to be measured. In chapter 2 the discussion narrows to the design of the NMR-based microprobe itself. Here, the criteria for the ideal, practical probe are laid out, while the remainder of the chapter deals with the problems of achieving this goal. In chapters 3-5, three strategies are presented for understanding and subsequently minimizing the perturbing effect of the probe on the field to be measured. A summary chapter and references conclude the thesis. To begin, however, we briefly survey field measurement technology.

1.2 Magnetic field measurement technologies

In many applications in science and technology, a precise and accurate determination of magnetic field strength is essential. Measurements are routinely made on fields ranging in strength from 1nT to greater than 10T. Magnetic field measurements are divided primarily into two categories, low and high field. Low field measurements are usually related to terrestrial magnetic phenomena, i.e. ~0.1mT. The measurement of strong magnetic fields, i.e. >30mT, is important in various physics disciplines such as accelerator design, mass spectrometry, the measurement of nuclear magnetic moments, and nuclear magnetic resonance.

Several technologies are available for measuring strong magnetic fields. The more popular of these include: magnetic resonance, the Hall effect, rotating coil and vibrating coil fluxmeters, techniques based on forces on current-carrying conductors, the giant

magnetoresistive effect, the Zeeman effect, magneto-optical methods such as rotation of a plane of polarization (Faraday effect) or laser magnetic resonance spectroscopy, and finally the magnetron principle. Typical resolution associated with these methods varies, but the best among them in terms of accuracy and precision is magnetic resonance. The other methods have a typical accuracy of a few tenths of a percent with the relative precision typically approaching 10^{-5}.

The first review article for methods of measuring strong magnetic fields appeared in 1955 (Symonds 1955). The methods described there have not changed significantly in the intervening 50 years except for the introduction of the giant magnetoresistive effect in 1988 by N. M. Bailbich, et. al.. The most recent review article was published in 1963 by C. Germain (Germain 1963).

1.3 NMR as a magnetic field measurement technology

The scientists who discovered the NMR phenomenon, Purcell et. al. (Purcell, Torey et al. 1946) and Bloch et. al. (Bloch, Hansen et al. 1946), realized its potential for measuring magnetic field strength. In his first paper on NMR, Bloch writes "nuclear induction [now called nuclear magnetic resonance] can well be developed as a simple and practical method to calibrate and measure high magnetic fields with great accuracy, and to apply it, for example, in the construction of cyclotrons and mass spectrographs" (Bloch 1946). Purcell also writes in his first paper on the subject, "Incidentally, [as] the apparatus required [for NMR] is rather simple, the method should be useful for standardization of magnetic fields." (Purcell, Torey et al. 1946). Both men saw that with the simplicity of the equipment required, high precision measurement of magnetic field strength would be possible for many investigators.

Interestingly, NMR-based magnetic field measurements are still the most precise method available more than 50 years after the technique was introduced.

The measurement of magnetic field strength by NMR can be performed with a minimum of electronic equipment, and is in fact done so in the commercial version of NMR-based magnetometers. For example, a popular, state of the art, NMR-based tesla meter, manufactured by MetroLab Instruments SA, has a measurement resolution of 5 parts per million (ppm) absolute accuracy with a relative accuracy, or precision, of 0.1 ppm with a measurement time of 1 second. This instrument is therefore unsuitable for measuring transient phenomenon with characteristic times in the tens of millisecond range. If a commercial magnetometer is not available, any working NMR spectrometer in service for spectroscopy or imaging experiments will almost certainly have the necessary hardware and software for making a measurement of field strength. In this work, for all experiments we used an NMR spectrometer normally employed for imaging.

1.4 The NMR experiment

1.4.1 Theory

Consider a sample of ordinary water placed in a uniform magnetic field B_0. The hydrogen nuclei in the sample will become weakly polarized along the direction of the applied field. The small average magnetization that exists can be expressed in the quantum mechanical description using Langevin's theory (Segre 1977)

$$M_0 = N\mu_I^2 \frac{B_0}{3kT}\frac{I+1}{I} = \chi B_0 \tag{1.1}$$

or

$$M_0 = N\gamma^2\hbar^2 \frac{B_0}{3kT} I(I+1), \qquad \text{where } \gamma = \frac{\mu_I}{I\hbar} \tag{1.2}$$

where M_0 is the magnetization or magnetic moment per unit volume, N is the number of number of protons per unit volume, μ_I is the proton magnetic moment, I is the spin of the proton (I=½) , k is the Boltzmann constant, T is temperature, χ is volumetric (nuclear) magnetic susceptibility of the water sample, and γ is the gyromagnetic ratio.

1.4.1.1 Precession

The small average magnetization will precess in the static B_0 field if perturbed from alignment with that field by some external force, as predicted by classical mechanics. The precessional frequency is given by the Larmor equation,

$$\omega_0 = \gamma B_0 , \tag{1.3}$$

where ω_0 is the angular frequency.

1.4.1.2 Excitation

It is common to use a reference system with the z-axis aligned with B_0 and further to introduce a second frame rotating around B_0 with a frequency $\omega \sim \omega_0$. The rotating frame is a useful aid to understanding the motion of the average value of the magnetic moment M_0 when a (smaller) perturbing magnetic field, called the B_1 field, is applied. Field B_1 lies in the xy plane and oscillates at frequency ω. The oscillating field can be decomposed into counter-rotating components, one of which will lie in the $\tilde{x}\tilde{y}$ plane of the rotating frame. In that frame, any magnetisation not aligned with the z-axis, precesses at frequency $\omega_0 - \omega$, and in particular, if $\omega = \omega_0$ the magnetisation will appear stationary. We therefore conclude that in this instance, the effective field in the z-direction has been reduced to zero. It follows that the magnetisation now precesses only about the rotating component of B_1 and its precessional frequency is again

described by the Larmor equation $\omega_1 = \gamma B_1$. As B_1 is in the *xy* plane, aligned magnetisation is therefore displaced: it nutates. The B_1 field is applied briefly (μs to ms) in order to limit the angular displacement, or *flip angle*, of the magnetization from its equilibrium alignment to angles normally less than 90 degrees for simple experiments, i.e. $\theta = \int \omega_1 dt \leq 90°$. The B_1 field is produced by a coil, carrying radiofrequency (RF) currents, which is usually in close proximity to the NMR sample. The "RF coil" and sample are components of the NMR probe as introduced in section 1.4.2.

1.4.1.3 Signal Reception

We may also employ the RF coil to detect the induced magnetization as it precesses (Bloch 1946; Bloch, Hansen et al. 1946; Bloch, Hansen et al. 1946). Using Faraday's Law of Induction, the general case of an induced *emf* $\mathscr{E}$ in a closed loop due to a nearby time-varying magnetic field is given by

$$\mathscr{E}(t) = \oint_C \mathbf{E}'(\mathbf{r},t)\cdot d\mathbf{l} = -\frac{d}{dt}\int_S \mathbf{B}(\mathbf{r},t)\cdot \hat{\mathbf{n}}\, da \tag{1.4}$$

where $\mathbf{E}'$ is the electric field at the element $d\mathbf{l}$ of the circuit C and da is a surface element on the surface S defined by the closed loop C. The induced *emf* is proportional to the *total* time derivative of the flux. Since in magnetic resonance experiments the circuit is stationary, the time derivative can be taken inside the integral where it becomes a partial time derivative. The circuit C can be thought of as any closed path in space, not necessarily coincident with an electric winding.

In our situation, the magnetic field $\mathbf{B}$ arises from the induced dipole moment $\mathbf{M}_0$ in the NMR sample and the unit vector $\hat{\mathbf{n}}$ corresponds to a surface bounded by the perimeter of the coil. Eq. (1.4) then appears as

$$\mathcal{E} = \oint_{C_{coil}} \mathbf{E}'(\mathbf{r},t)\cdot d\mathbf{l} = -\int_{S_{coil}} \frac{\partial}{\partial t} M_0(\mathbf{r},t)\sin\theta\, da \tag{1.5}$$

As an alternative approach, we consider the reciprocal situation where the circuit (or "coil") itself produces a magnetic field $\mathbf{B}_1$ when *constant* current i flows through it. (The $\mathbf{B}_1$ magnetic field is usually an oscillating field. For present purposes, consider the $\mathbf{B}_1$ field to be constant in time.) At the same time, a time-varying magnetic moment $\mathbf{m}$ is present. The potential energy of a moment in the $\mathbf{B}_1$ field is given by $U = -\mathbf{B}_1 \cdot \mathbf{m}$. For the case of an extended dipole moment, e.g. $\mathbf{M}_0$, then the potential energy for the dipole-$\mathbf{B}_1$ interaction becomes

$$U(t) = -\int_{sample} \mathbf{B}_1(\mathbf{r})\cdot\mathbf{M}_0(\mathbf{r},t)\, dV \tag{1.6}$$

where the integration is needed only over the volume of the magnetized material. The flux through the circuit changes due to the distributed magnetic moment and electromotive force $\mathcal{E}$ is induced around it. In order to keep the current constant, the sources of current i must do work. The sources do work to maintain the current at the rate, (Jackson 1975; Hoult and Bhakar 1997).

$$\frac{dU(t)}{dt} = -i\mathcal{E}(t) \qquad \text{or} \qquad \mathcal{E}(t) = -\frac{1}{i}\frac{dU(t)}{dt} \tag{1.7}$$

Therefore we have (Hoult and Richards 1976; Peck, Magin et al. 1995)

$$\mathcal{E}(t) = -\frac{1}{i}\frac{d}{dt}\int_{sample} \mathbf{B}_1(\mathbf{r})\cdot\mathbf{M}_0(\mathbf{r},t)\, dV = -\int_{sample} \frac{\partial}{\partial t}\left\{\left(\frac{\mathbf{B}_1(\mathbf{r})}{i}\right)\cdot\mathbf{M}_0(\mathbf{r},t)\right\} dV \tag{1.8}$$

where dV is a three dimensional volume of integration, and $(\mathbf{B}_1/i)$ is often called the sensitivity of the coil. This is an expression of the Principle of Reciprocity.

We examine Eq. (1.8) in the instance where both $\mathbf{B}_1$ and $\mathbf{M}_0$ are uniform and may be taken out of the integral, and the magnetization $\mathbf{M}_0$ has been moved, or "flipped" by 90° into the same plane as the $\mathbf{B}_1$ field by the application of *alternating* current to the RF coil. Equation (1.8) may then be written as

$$\mathscr{E}(t) = K\omega_0\left(\frac{B_{1\_xy}}{i}\right)M_0\cos(\omega_0 t)\Delta V \tag{1.9}$$

where K is a constant associated with approximations $\mathbf{B}_1(\mathbf{r}) \sim \mathbf{B}_1$ and $\mathbf{M}_0(\mathbf{r},t) \sim \mathbf{M}_0(t)$, B_{1_xy} is the component of $\mathbf{B}_1$ in the *x-y* plane , i.e. the plane perpendicular to the main $\mathbf{B}_0$ field, and ΔV is the sample volume. Note that the phase in Eq. (1.9) has been ignored.

1.4.1.4 Relaxation

In this description, we have not yet considered the interactions that the magnetization may have with its environment. Following the brief application of the oscillating or rotating B_1 field that tips the net magnetization out of alignment with B_0, the spins that make up the net magnetization return to their equilibrium position by a first-order spin-spin relaxation process characterized by a time T_1, the *spin-lattice relaxation time.* In the case of a 90° flip-angle, the heuristic mathematical expression for the relaxation process is given by

$$M_z(t) = M_0\left[1-\exp\left(\frac{-t}{T_1}\right)\right] \tag{1.10}$$

T_1 is dependent on the fluctuating transverse component at he Larmor frequency of the field from nearby nuclei undergoing translational Brownian motion. The precessing spins are also affected by ultra-low frequency fluctuating *axial* field components that essentially introduce random variables in the Larmor frequency ω_0. Thus, over time, random walks

disperse the coherent transverse magnetization into an increasingly incoherent magnetization with smaller and smaller average value. This process is characterized by the time constant T_2 in the heuristic mathematical expression $\exp(-t/T_2)$; $T_2 \leq T_1$ in all cases.

If the NMR sample is located in an inhomogeneous field, the precessing spins are also affected by a pseudo-relaxation process. Nuclei at different parts of the sample experience slightly different values of the field, hence by Eq. (1.3), resonate at slightly different frequencies and the initially coherent average magnetic moment will become dephased as the precession advances. In a very poor exponential decay model, this effect is represented by the time constant T_2^* and is, in principle, reversible. Since perfectly uniform magnetic fields are not achievable, then strictly speaking, the observed free induction decay is always characterized bya decay described by T_2^*. However, for a well shimmed field, the difference between T_2 and T_2^* may be negligible.

The consequence of the relaxation mechanisms in the NMR experiment is that the NMR signal diminishes as a function of time until the signal is at the level of the background noise. However for time interval much less than T_2*, the instantaneous B_1 field strength may be determined from the rate of change of phase of the transverse magneisation (and hence from the voltage induced in the RF coil) – the motication for this thesis described in section 1.1. Most experiments to be described were conducted by the simple sequence of a single alternating field B_1 pulse (~μs) followed by an acquisition of the induced EMF – the free induction decay, or as it is often simply abbreviated, the FID. The full expression for the form of the induced EMF (or FID) is then (Chen and Hoult 1989)

$$\mathcal{E}(t) = CM_0\Delta V \exp(-t/T_2)\cos(\omega_0 t + \phi) \tag{1.11}$$

where C and ϕ are constants, and ΔV is the sample volume. Current state of the art digital-to-analog converters cannot directly digitize our NMR signal with useful resolution if it is at ultra-high frequency (UHF~ 400MHz say) (Walden 1999). Rather, (analogue) phase-sensitive detection is used prior to digitisation. Briefly, in this detection method the NMR signal at frequency ω_0 is fed to phase sensitive detectors that yield two audio frequency output signals that are 90° out of phase with each other (a complex signal) and shifted in frequency to a new frequency $\Delta\omega = \omega_0 - \omega_r$ where ω_r is a reference frequency. The form of the signal is then (Chen and Hoult 1989)

$$S(t) = \alpha C M_0 \exp\left(\frac{-t}{T_2}\right)\exp\left(j[\Delta\omega t + \phi]\right) \tag{1.12}$$

where α and ϕ are constants related to the electronics of the NMR receiver and $j = \sqrt{-1}$.

The relaxation mechanisms presented above are, at best, an introductory note in a subject area that is both deeply complicated and interesting. However, the relaxation parameters that are critical to this work are now identified and the interested reader is referred to some of the basic texts on NMR (see references on page 1) for further information.

1.4.1.5 Line width, resolution and magnetic field inhomogeneity

In this section we discuss the off-line processing of the FID signal that reveals the frequencies present in the complex waveform and their amplitude. The natural linewidth, resolution, and the effect of magnetic field inhomogeneity on the NMR spectra are then investigated. Finally the relationships between NMR sample size, magnetic field inhomogeneity and spectral resolution are discussed.

The primary operation performed is one of Fourier transformation. Thus:

$$H(\omega)=\int_0^{\infty}\alpha\Delta V M_0'\exp\left(\frac{-t}{T_2}\right)\exp\left(j\left[(\Delta\omega-\omega)t+(\phi-\nu)\right]\right)dt$$
$$=\exp\left[i(\phi-\nu)\right]\frac{\alpha\Delta V M_0' T_2}{1-i(\Delta\omega-\omega)T_2}. \tag{1.13}$$

where ω is the frequency variable and the phase ν can be adjusted such that $\nu=\phi$. The real part of Eq. (1.13) is then a Lorentzian absorption curve given by

$$\mathrm{Re}\,H(\omega)=\frac{\alpha\Delta V M_0' T_2}{1+(\Delta\omega-\omega)^2 T_2^2}. \tag{1.14}$$

while the imaginary part of Eq. (1.13) is a dispersion curve given by

$$\mathrm{Im}\,H(\omega)=-\frac{\alpha\Delta V M_0'(\Delta\omega-\omega)T_2^2}{1+(\Delta\omega-\omega)^2 T_2^2} \tag{1.15}$$

The maximum in the Lorentzian absorption curve occurs at $\Delta\omega=\omega$ and the full width at half maximum is $\Delta\omega_{FWHM}=2/T_2$ or $\Delta f_{FWHM}=1/\pi T_2$ expressed in hertz. We define the spectral resolution as

$$\frac{\Delta f_{FWHM}}{f_0} \tag{1.16}$$

Using Eq. (1.16) we can now determine a specification for the relaxation times T_1 and T_2 of a suitable sample material given the major objectives of the thesis. For example, to make a frequency measurement on a 9.4 T magnet (f_0 = 400MHz), at a resolution of 2.5×10^{-9} we require the *FWHM* of the linewidth to be ~1Hz. For a target linewidth of $\leq$1Hz then using the relation $\Delta f_{FWHM}=1/\pi T_2$ we see that the required relaxation time is $T_2\geq 320\text{ms}$. There are several liquids that would suffice. For example, water has a characteristic T_1 on the order of 3 seconds and a T_2 on the order of 1.7 seconds (Abragam 1961) which is more than sufficient

for our purposes. For all experiments presented here, high purity water (ASTM Type 1) was used. The sample can also be doped with paramagnetic salts that effectively reduce the T_1 and T_2 times. This would be needed if the magnetization of the sample had not returned to alignment with B_0 before the next experiment (i.e. RF transmit pulse) for an updated field measurement.

The basic measurement of magnetic field strength and it associated uncertainty can be calculated using the Larmor equation given in Eq. (1.3), solving for B and it associated fractional uncertainty:

We see from Eq. (1.17) that the accuracy of the magnetic field measurement is limited to the known precision of γ and the resolution of the NMR measurement. At the time of Purcell and Bloch's first papers, the gyromagnetic ratio for protons in water molecules, i.e. the shielded proton gyromagnetic ratio γ'_p, was 2.66×10^8 rad-s^{-1}-T^{-1} (Kellogg, Rabi et al. 1939). The value recommended by the Committee on Data for Science and Technology (CODATA 1998) for this ratio is $2.675\ 153\ 41\ (11)\times10^8$ rad-s^{-1}-T^{-1} or $\gamma'_p/2\pi = 42.576\ 3888(11)\times10^8$ MHz-T^{-1} (H_20, sphere, 25°C) where the numbers in parentheses are the numerical value of the standard uncertainty referred to the corresponding last digits of the quoted result. The relative standard uncertainty in this result is 4.2×10^{-8}. In the context of the NMR experiments to follow it is understood that we are always referring to the *shielded* proton gyromagnetic ratio and simply write $\gamma'_p = \gamma$.

If we compare the relative standard uncertainty for γ, 4.2×10^{-8}, and our specification for the resolution of the NMR measurement given earlier, 2.5×10^{-9}, we see that *if* our target

specification NMR resolution is met, then the accuracy of the magnetic field measurement will be limited by the uncertainty in γ. However, if our task is simply to track *changes* in the magnetic field strength to high precision, as would be the case if we were trying to follow the effect of transient eddy currents that may arise in the course of a magnetic resonance imaging experiment, the measurement of the NMR frequency to high precision is still useful.

Up to this point, we have implicitly assumed that experiments are carried out in a uniform magnetic field, i.e. $T_2 = T_2^*$. However, the NMR linewidth can be greatly broadened beyond the natural line width by the presence of magnet field inhomogeneity, i.e. $T_2^* << T_2$. In this case, the spectral peak shape, the position of the peak, and its full width at half maximum in the absorption curve will not have an analytical representation. The absoption curve will now reflect the fact that nuclei at different parts of the sample experience slightly different values of the field, and hence by Eq. (1.3), resonate at slightly different frequencies The width of the peak is simply related to the range of magnetic field strengths experienced in the NMR sample.

We next examine the relationship between magnet field homogeneity and the size of the NMR sample. In the case of the 9.4T magnet used extensively in this work, the basic homogeneity in the useable volume of the magnet (a 10cm diameter spherical region) was 10 parts per million (ppm). The overriding inhomogeneity was a linear (4000Hz/10cm) field gradient. Then inverting this figure, the inverse of the gradient becomes **25μm/1Hz**. Thus the linear dimension of the sample in the direction of field inhomogeneity should be on the order 25μm for a frequency resolution of 1Hz. A 25μm wide liquid sample (long T_2) would be difficult to construct and has not been previously reported in the literature. To date the

smallest coil constructed for NMR-based probe has been 100μm x 100μm (Peck, Magin et al. 1994): in this case for the application of NMR micro-spectroscopy. Fortunately, we were able to take measures, as described in Section 1.5.2, to improve the homogeneity of the magnet field so that a larger and more practical sample volume on the order of 1mm could be used. However, it is now clear that sample size limits the field gradients that can be accommodated while maintaining precise frequency measurements.

After magnetic field corrections are made, the probe itself should not introduce local inhomogeneity in the main magnetic field, which would have the effect of adding additional frequencies to the received NMR signal and of degrading measurement precision. Probe-related field inhomogeneity arises from the diamagnetic or paramagnetic nature of the building materials used in the probe's construction (as will be discussed extensively in chapters 2-5). Note that susceptibility-related inhomogeneity is indistinguishable from magnet-related inhomogeneity in the NMR signal.

1.4.1.6 Signal-to-noise ratio

The SNR is often used as an indicator of overall probe performance in NMR spectroscopy and imaging applications. For the purposes of measuring the magnetic field strength, by collection of the FID followed by Fourier transformation, SNR is usually considered of secondary importance to resolution, only a minimal signal being necessary to reveal the NMR signal above the background. However, if the *instantaneous* Larmor frequency is to be measured from the rate of change of phase of the FID, it is clear that a much greater SNR is needed. The signal amplitude has been given earlier in Eq. (1.8), viz

$$\mathcal{E}(t) = -\int_{sample} \frac{\partial}{\partial t}\left\{\left(\frac{\mathbf{B}_1}{i}\right)\cdot\mathbf{M}_0\right\} dV \qquad (1.18)$$

Both $\mathbf{B}_1(\mathbf{r})$ and $\mathbf{M}_0(\mathbf{r},t)$ need to be evaluated for every RF coil design under study. The expression for the time domain SNR is given simply as

$$\begin{aligned}\text{SNR} &= \frac{\text{peak signal}}{\text{RMS noise}} \\ &= \frac{\left[\int_{sample} \frac{\partial}{\partial t}\left\{\left(\frac{\mathbf{B}_1}{i}\right)\cdot\mathbf{M}_0\right\}dV\right]_{peak}}{\text{RMS noise}}\end{aligned} \tag{1.19}$$

where the RMS noise must also be evaluated for the RF coil design under study.

Concerning ourselves for the moment with the expression for the signal $\mathscr{E}(t)$, we can make the assumption as in Eq. (1.9) that $\mathbf{B}_1$ and $\mathbf{M}_0$ are uniform. Then using Eq. (1.9) and Eq. (1.1) for M_0, the signal amplitude in the form of the peak voltage induced in the probe after a 90° pulse is given by

$$\begin{aligned}\mathscr{E}_{peak} &= \frac{K\omega_0^2\left(\frac{B_{1,xy}}{i}\right)\left[N\gamma\hbar^2 I(I+1)\right]\Delta V}{3k_B T} \\ &\propto \omega_0^2\left(\frac{B_{1,xy}}{i}\right)\Delta V\end{aligned} \tag{1.20}$$

We see in Eq. (1.20) that the signal is proportional to the square of the nuclear precession frequency, the sensitivity of the probe coil, and the sample volume.

The sensitivity is dependent on the size and geometry of the specific RF coil. Consider, for example, the common RF coil shape of a solenoid. The on-axis sensitivity at the centre of an ideal single-layer solenoid of many turns $(n \gg 1)$ is given as (Ohanian 1988)

$$\left(\frac{B_{1,xy}}{i}\right) = \frac{\mu_0 n}{d\sqrt{1+[h/d]^2}} \tag{1.21}$$

where h is the coil length and d is the coil diameter. When the shape of the coil remains constant, i.e. $[h/d]$ unchanged, the sensitivity is seen to increase for smaller coil diameters. An equivalent form of Eq. (1.21) using the number of turns per unit length n' of the solenoid, gives

$$\frac{B_{1,xy}}{i} = \frac{\mu_0 n'[h/d]}{\sqrt{1+[h/d]^2}} \tag{1.22}$$

The noise in the time domain of the NMR signal arises from the RF coil, the NMR sample, and the receiver electronics. From the coil we have resistive Johnson noise, while from the sample, the noise is due to Brownian motion of the electrolytes and spin noise (Hoult and Ginsberg). In practice the NMR signal is also affected by phase noise in the receiver electronics, which is characterized by so-called $1/f$ noise. For small microcoils (i.e. d< 1mm) the Johnson noise is dominant, and thus is primarily thermal noise described by the Nyquist formula

$$\mathscr{E}_{noise} = \sqrt{4k_B T R_{coil} \Delta f} \tag{1.23}$$

where R_{coil} is used to represent all losses in the coil, e.g. RF element, matching/tuning capacitors, eddy currents, and Δf is the spectral bandwidth. The specific form of the parameter R_{coil} now becomes the most significant factor in probe performance. An exact form of R_{coil} for the solenoid is not found in the literature. The high-frequency, alternating-current case is complicated by skin effect as well as proximity to other current-carrying conductors. These effects will effectively alter the distribution of current throughout the conductor and change the current-carrying cross section (Hoult and Richards 1976; Peck,

Magin et al. 1995). The RF coil, essentially an inductance with a small resistance, is "noise-matched" to the pre-amplifier os that the latter gives its best performance. In other words, with the aid of a net, the impedance of the coil is transformed to the optimal source impedance of the first device in the preamplier (usually a field effect transistor) A standard model for this type of matching may be found in (Hoult 1978)

As an approximation of R_{coil} for the solenoid, consider the simpler case of a long straight wire. The resistance of the wire is given by $R = l/gA$ where l is the length of the conductor, g is the conductivity, and A the current-carrying cross section. The skin depth in a conductive medium is given by

$$\delta \equiv \sqrt{\frac{2}{\mu_0 \omega g}} \tag{1.24}$$

where μ_0 is the permeability of free space. Therefore, for a long, straight wire where the skin depth is much less than the wire diameter, the resistance is

$$R_{\text{straight wire}} = \frac{l}{gA} \equiv \frac{l}{gp\delta} \equiv \frac{l}{p}\sqrt{\frac{\mu_0 \omega}{2g}} \tag{1.25}$$

where p is the wire circumference. With the traditional solenoidal coil inter-turn spacing (centre-to-centre) of 1.5 times the wire diameter (Hoult and Richards 1976), the expression for the noise, Eq. (1.23), now becomes

$$\mathscr{E}_{noise} = \sqrt{4k_B T \frac{\zeta l}{p} \Delta f}\left[\frac{\mu_0 \omega}{2g}\right]^{1/4} \tag{1.26}$$

where a proximity factor ζ has been introduced in the square root to account for the approximation of the straight wire resistance to the case of the solenoid resistance (typically $1 \le \zeta \le 3$ (Peck, Magin et al. 1995)).

Equations (1.20) and (1.26) can be combined to give the equation for time-domain SNR for a many-turn coil where the skin depth is much less than the conductor diameter:

$$\begin{aligned} \mathbf{SNR} &= \frac{\mathscr{E}_{\text{peak}}}{\mathscr{E}_{\text{noise}}} \\ &= \frac{K\omega_0^{7/4}\left[N\gamma\hbar^2 I(I+1)\right]\Delta V}{(k_B T)^{3/2}} \frac{\mu_0 n}{d_{coil}\sqrt{1+\left[h/d_{coil}\right]^2}} \\ &\quad \times \left[\frac{p}{\zeta l \Delta f}\right]^{1/2}\left[\frac{g}{648\mu_0}\right]^{1/4} \\ &\propto \frac{\omega_0^{7/4}\Delta V}{d_{coil}} \end{aligned} \tag{1.27}$$

where the factor of 648 arises simply through combining the factors of 2, 3, and 4 (to various powers) in equation (1.18) and (1.24).

The SNR in the regime where the wire size in the RF coil is on the order of, or less than, the skin depth has been further studied by Peck, et. al. (Peck, Magin et al. 1995). Under these conditions the current distribution is nearly uniform. The SNR for a n-turn solenoidal winding with $n \gg 1$ in the uniform current regime is then given by

$$\mathbf{SNR} \propto \frac{\omega_0^2 \Delta V}{\sqrt{n d}} \tag{1.28}$$

From the time-domain SNR given in Eq. (1.27) we can estimate the intrinsic spectral SNR in the Fourier transformed data. This can be obtained by integrating the signal voltage, given earlier in Eq.(1.12), over the time of acquisition (Hoult 1996)

$$\begin{aligned}\mathscr{E}_{\text{signal}} &= \int_{t'=0}^{t} 2\pi\omega_0\left(\frac{B_{1,xy}}{i}\right)M_0'\Delta V\exp\left(\frac{-t'}{T_2}\right)dt' \\ &= 2\pi\omega_0\left(\frac{B_{1,xy}}{i}\right)M_0T_2\Delta V\left[1-\exp\left(\frac{-t}{T_2}\right)\right]\end{aligned} \tag{1.29}$$

In the limit where $t \to \infty$ we see that the signal $\mathscr{E}_{\text{signal}} \to 2\pi\omega_0\left(B_{1,xy}/i\right)M_0T_2\Delta V$.

This value represents the height of the spectral peak. A similar integration can be carried out for the RMS noise in the NMR experiment as well. This integration however, may be shown to be equivalent to applying a filter of width $\Delta\nu = 1/t$ (in Hz) and gain t (Chen 1989). Thus, the noise on the base line of the spectrum is

$$N = F'\sqrt{4k_BTRt} \tag{1.30}$$

where F' is the noise factor associated with the NMR receiver (typically 1.05) and thus N is seen to increase as the square root of the length of the acquisition. If we take the signal given by Eq. (1.29) and noise given by Eq. (1.30), and form the SNR

$$\text{SNR}_{\text{spectrum}} = \frac{2\pi\omega_0\left(\frac{B_{1,xy}}{i}\right)M_0T_2\Delta V\left[1-\exp\left(\frac{-t}{T_2}\right)\right]}{F'\sqrt{4k_BTRt}} \tag{1.31}$$

the spectral SNR goes through a maximum when the data have been collected for a time $t = 1.255\,T_2$. This optimal time for best spectral SNR is not, however, the optimal time for the best line shape and resolution of the spectral peak. The data must be collected for a longer period. Filter methods in the time domain that diminish the noise to zero (e.g. exponential attenuation as a function of time) as the NMR signal becomes comparable with the noise can be used to optimize the SNR in the frequency domain at the expense of resolution. However,

in the experiments described in this thesis no time-domain filtering was used. The data were acquired until the time domain S/N was $\ll 1$ in order to achieve the best spectral resolution.

We note that when designing microcoils for best resolution together with best time domain SNR, it is much easier to achieve the latter, often at the expense of the former. Good SNR is achieved by placing the RF coil near the NMR sample. However, the coil significantly perturbs the local static magnetic field, and resolution is compromised if the perturbation extends into the volume of the NMR sample. We therefore optimized resolution first (by minimizing coil-related field inhomogeneity), and were content with the resulting SNR achieved. The origin of the probe-related field perturbation (including the coil) and the measures taken to minimize its effect on the spectral linewidth are discussed extensively in Chapters 2-5.

1.4.2 Apparatus

The basic block diagram of the spectrometer is given in Fig. 1.1. The particular magnet used in this work was a 9.4T horizontal bore magnet with an open bore diameter of 210mm, manufactured by Magnex, Abingdon, UK. The bore is fitted with a shim/gradient insert (the role of this component to be discussed in the following paragraphs) that leaves a final open bore diameter of 110mm. The probe contains the NMR sample which can either be integrated into the probe's construction, for example a small sphere of water as would be the case for a field strength measurement probe, or the sample can be removable, as would be the case in clinical imaging where a person is moved into the magnet bore that also houses a large permanently mounted body RF coil on the bore periphery. Probes are usually custom-built for a specific experiment although general-purpose commercial probes are available. When the sample dimensions are about a millimetre or smaller, the probe is usually referred to as a

micro-probe. A transmit/receive switch (not shown in Fig. 1.1) is used to select whether the probe is in transmit or receive mode. The remainder of the spectrometer is an "off-the-shelf" research-type instrument, in this case the "Bio-Spec" model manufactured by Brüker Medizintechnik.

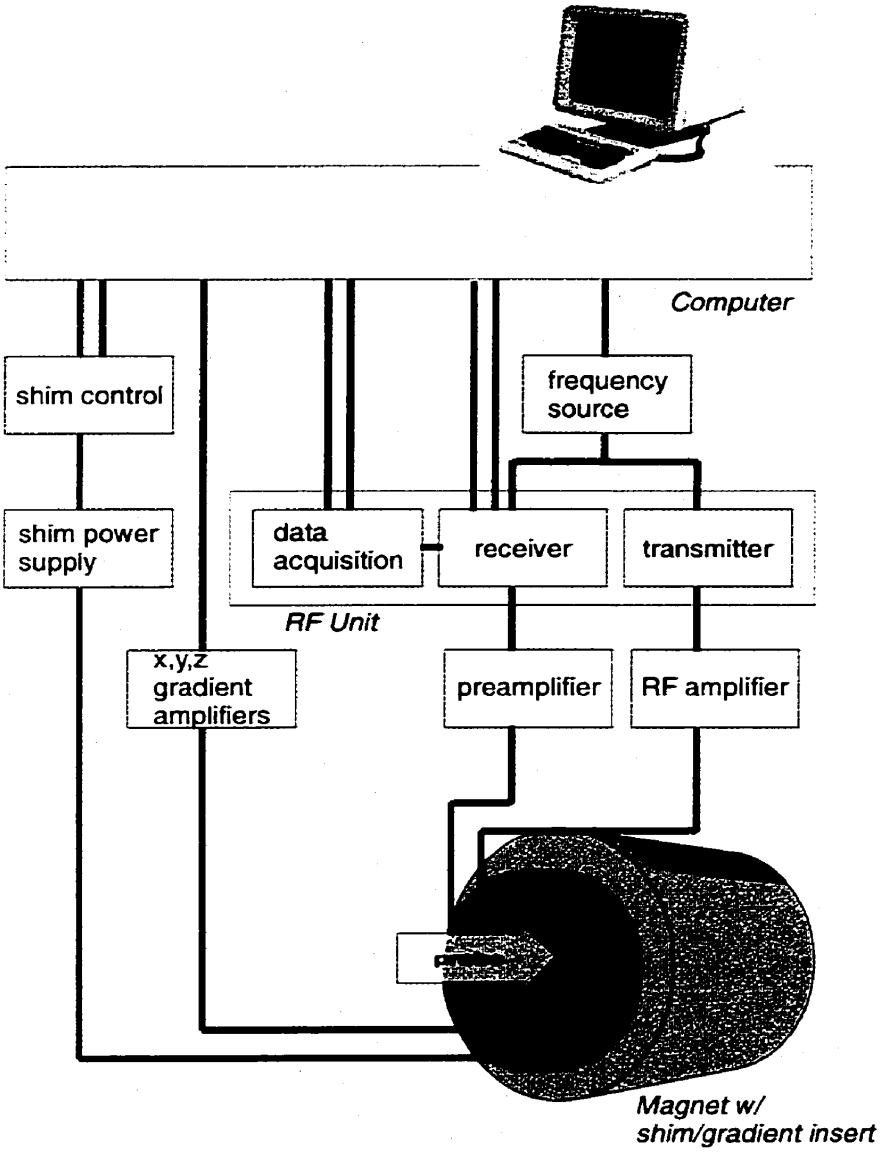

Fig. 1.1. NMR system diagram.

1.4.3 Procedure

The probe was placed at the iso-centre of the magnet and a FID acquired from a single pulse experiment with the following parameters. The frequency bandwidth was 50,000Hz in order to observe a broad range of frequencies that might be present throughout the sample due to various magnetic field strengths. The acquisition time varied according to the observed length of the free induction decay. In all cases, the data were acquired until the time domain SNR ratio was $\ll 1$. The flip angle used in all cases was 10°. This was verified in several ways. The most common for a given probe was to use a fixed transmitter power and slowly increase the pulse duration while observing the effect on the free induction decay. The Brüker on-line software can integrate the free induction decay and a maximum result implied a 90° flip angle. The pulse width was then divided by 9 to obtain the duration for a 10° flip angle.

Coarse power adjustments were made using fixed attenuators in 10dB increments at the output of the power amplifier. For the RF coils in this thesis the power settings were in the range of approximately 3~30W for a pulse of duration 2-10 μs.

After the transmitter pulse there were two short delays before the first data point from the free induction decay was acquired. The delays were necessary to prevent artefacts from the transmitter/receiver switching and audio frequency filters from appearing in the Fourier transform of the free induction decay data. These delays are fully described in the book by Chen & Hoult (Hoult, Chen et al. 1983). The first delay was in the interval between the end of the transmit pulse and the opening of the receiver. The second delay was from the start of the receiver ON until the first data point was collected. The system software often automatically sets the delays. However, this procedure is not always successful for free induction decays that contain a broad range of frequencies The correct delays were therefore determined

experimentally and for an acquisition/filter bandwidth set to 50kHz, were 6.3μs and 1μs for receiver-on delay and first-data-point delay respectively.

1.5 Description and correction of the base magnetic field

The probe designs presented in this thesis have been intended for use in the bore of a high field magnet. However, as mentioned earlier, if they are to be assessed adequately, the base magnetic field from the magnet must be sufficiently homogeneous. The field can be described using spherical harmonic analysis based on a spherical coordinate system. The advantage of this description is that the field is completely described by a sum of terms that are orthogonal to each other on the surface of a sphere. Corrective measures that affect any single harmonic are therefore independent and do not affect other harmonic terms. Further, the desired homogeneous field and simple fields such as linear gradients are members of the basis set.

We begin this analysis by considering the Maxwell equations appropriate for the magnetic **B** and **H** fields in magnetostatics:

$$\nabla \cdot \mathbf{B} = 0, \qquad \nabla \times \mathbf{H} = \mathbf{J}_f \ (SI \text{ expression}) \tag{1.32}$$

where $\mathbf{J}_f$ is the *free current density*. The free current density in this case is due to the current in the superconducting solenoid that generates the strong magnetic field B_0. The free current density in the bore of the magnet is of course zero and Eq. (1.32) becomes $\nabla \times \mathbf{H} = \mathbf{0}$. We can then define a magnetic scalar potential Φ such that $\mathbf{H} = -\nabla\Phi$. In free space $\mathbf{B} = \mu_0 \mathbf{H}$ and we may rewrite the first equation in Eq. (1.32) as

$$\nabla \cdot (\mu_0 \nabla \Phi) = 0, \tag{1.33}$$

or simply Laplace's equation

$$\nabla^2\Phi = 0. \tag{1.34}$$

The general solution of Laplace's equation in spherical coordinates (r,θ,ϕ) can be written in terms of spherical harmonics $Y_{nm}(\theta,\phi)$ and powers of r as (Jackson 1975)

$$\Phi(r,\theta,\phi) = \sum_{n=0}^{\infty}\sum_{m=-n}^{n}\left[A_{nm}r^{n} + B_{nm}r^{-(n+1)}\right]Y_{nm}(\theta,\phi) \tag{1.35}$$

where the A_{nm} and B_{nm} terms contain the field sources. The normalized $Y_{nm}(\theta,\phi)$ are defined as

$$Y_{nm}(\theta,\phi) = \sqrt{\frac{2n+1}{4\pi}\frac{(n-m)!}{(n+m)!}}P_{nm}(\cos\theta)e^{im\phi} \tag{1.36}$$

where the $P_{nm}(\cos\theta)$ are the associated Legendre functions (see Table 1.1). We need consider only the case when $m \geq 0$, as the associated Legendre functions for negative m are defined in terms of the associated Legendre functions with positive m. We also consider $n \geq 1$ since we can choose the zero point of potential arbitrarily and we are interested in points close to the origin. The magnetic field $B(r,\theta,\phi)$ may be found by

$$\begin{aligned} B_z(r,\theta,\phi) &= -\mu_0\partial\Phi(r,\theta,\phi)/\partial z, \\ B_x(r,\theta,\phi) &= -\mu_0\partial\Phi(r,\theta,\phi)/\partial x, \\ B_y(r,\theta,\phi) &= -\mu_0\partial\Phi(r,\theta,\phi)/\partial y. \end{aligned} \tag{1.37}$$

However, the fields in the x and y directions are several orders of magnitude less than the field in the z-direction and are ignored. If we return to Eq. (1.32) for a moment, we find

that we can also write the magnetic field $B_z(r,\theta,\phi)$ directly in terms of spherical harmonics $Y_{nm}(\theta,\phi)$ and powers of r. To do this we substitute $\mathbf{H}=\mathbf{B}/\mu_0$ into $\nabla\times\mathbf{H}=\mathbf{0}$ to get

$$\nabla\times\mathbf{B}(r,\theta,\phi)=\mathbf{0}. \tag{1.38}$$

Further

$$\nabla\times\left(\nabla\times\mathbf{B}(r,\theta,\phi)\right)=\mathbf{0}, \tag{1.39}$$

from which it may be shown that

$$\nabla^2 B_x(r,\theta,\phi)=\nabla^2 B_y(r,\theta,\phi)=\nabla^2 B_z(r,\theta,\phi)=0. \tag{1.40}$$

Thus B_z can be described directly in terms of

$$B_z(r,\theta,\phi)=\sum_{n=0}^{\infty}\sum_{m=-n}^{n}\left[A_{nm}r^n+B_{nm}r^{-(n+1)}\right]Y_{nm}(\theta,\phi). \tag{1.41}$$

In the NMR field it is common practice to use an unnormalised form of Eq. (1.41) (Romeo and Hoult 1984). The new form appears as

$$B_z(r,\theta,\phi)=\sum_{n=0}^{\infty}\sum_{m=0}^{n}C_{nm}r^n P_{nm}(\cos\theta)\cos m(\phi-\psi) \tag{1.42}$$

where C_{nm} and ψ are now the arbitrary constants representing the amplitude and phase respectively of the field components present in the magnetic field.

1.5.1 Field plotting and analysis

We determine the relative contributions of various spherical harmonics in the magnet field by measuring the field strength at various points in the central region of the bore as shown in Fig. 1.1.

Table 1.1. Legendre and Associated Legendre functions for a few lower order n and degree m terms.

n=0	$P_0(\cos\theta) = 1$	
n=1	$P_1(\cos\theta) = \cos\theta$	$P_{11}(\cos\theta) = \sin\theta$
n=2	$P_2(\cos\theta) = \frac{1}{2}\left(3\cos^2\theta - 1\right)$	
	$P_{21}(\cos\theta) = 3\sin\theta\cos\theta$	$P_{22}(\cos\theta) = 3\sin^2\theta$
n=3	$P_3(\cos\theta) = \frac{1}{2}\left(5\cos^3\theta - 3\cos\theta\right)$	$P_{32}(\cos\theta) = 15\sin^2\theta\cos\theta$
	$P_{31}(\cos\theta) = \frac{3}{2}\sin\theta\left(5\cos^2\theta - 1\right)$	$P_{33}(\cos\theta) = 15\sin^3\theta$
n=4	$P_4(\cos\theta) = \frac{1}{8}\left(35\cos^4\theta - 30\cos^2\theta + 3\right)$	
	$P_{41}(\cos\theta) = \frac{5}{2}\sin\theta\left(7\cos^3\theta - 3\cos\theta\right)$	$P_{43}(\cos\theta) = 105\sin^3\theta\cos\theta$
	$P_{42}(\cos\theta) = \frac{15}{2}\sin^2\theta\left(7\cos^2\theta - 1\right)$	$P_{44}(\cos\theta) = 105\sin^4\theta$
n=5	$P_5(\cos\theta) = \frac{1}{8}\left(63\cos^5\theta - 70\cos^3\theta + 15\cos\theta\right)$	$P_{53}(\cos\theta) = \frac{105}{2}\sin^3\theta\left(9\cos^2\theta - 1\right)$
	$P_{51}(\cos\theta) = \frac{15}{8}\sin\theta\left(21\cos^4\theta - 14\cos^2\theta + 1\right)$	$P_{54}(\cos\theta) = 945\sin^4\theta\cos\theta$
	$P_{52}(\cos\theta) = \frac{105}{2}\sin^2\theta\left(3\cos^3\theta - \cos\theta\right)$	$P_{55}(\cos\theta) = 945\sin^5\theta$
n=6	$P_6(\cos\theta) = \frac{1}{16}\left(231\cos^6\theta - 315\cos^4\theta + 105\cos^2\theta - 5\right)$	
	$P_{61}(\cos\theta) = \frac{21}{8}\sin\theta\left(33\cos^5\theta - 30\cos^3\theta + 5\cos\theta\right)$	$P_{64}(\cos\theta) = \frac{315}{2}\sin^4\theta\left(11\cos^2\theta - 1\right)$
	$P_{62}(\cos\theta) = \frac{105}{8}\sin^2\theta\left(33\cos^4\theta - 18\cos^2\theta + 1\right)$	$P_{65}(\cos\theta) = 10395\sin^5\theta\cos\theta$
	$P_{63}(\cos\theta) = \frac{315}{2}\sin^3\theta\left(11\cos^3\theta - 3\cos\theta\right)$	$P_{66}(\cos\theta) = 10395\sin^6\theta$

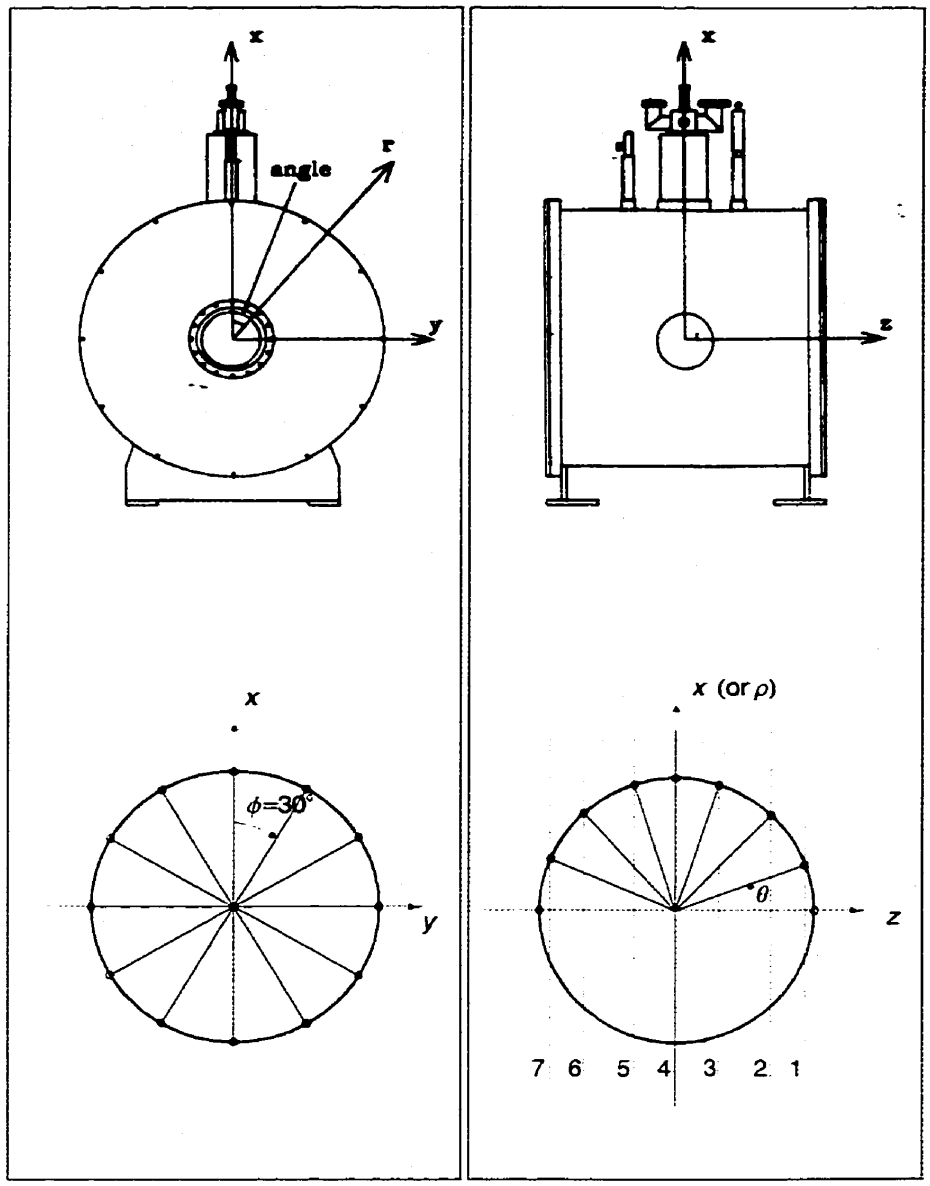

Fig. 1. 2 Magnetic field plotting coordinate system. Plotting consists of measuring the strength of the magnetic field at various points in central region of the magnet (shown in red) which are on the surface of an imaginary sphere. Note: The manufacturer's convention for the plotting coordinate system has been used here. The left panel shows the plotting points chosen in the azimuthal plane at 30° intervals. The right panel shows the increments in longitudinal angle θ in order to define the position of seven planes along the z-axis. The θ angles are chosen to make $P_{70} = 0$. The field is also measured along the z-axis (i.e. axial values).

Table 1.2. Magnetic field plotting coordinates. The declinational angle θ determines the position of the planes in the field plot. The angles in the table below make the Legendre function $P_{70} = 0$. In most practical cases, orders higher than P_{70} may be ignored. The θ angle is converted into cylindrical coordinates z, ρ for a field map in on a 10cm diameter spherical boundary.

θ		z	ρ
Radians	degrees	(cm)	(cm)
0	0	5	0
0.320 05	18.4°	4.745	1.575
0.735 19	42.1°	3.709	3.355
0.152 78	66.0°	2.030	4.570
$\pi/2$	90.0°	0	5

The magnetic field plot can be analyzed in terms of spherical harmonics. Two computer programs were available for this analysis. The first was called MULTISHIM (Manufacturer: Magnex Scientific, Abington, U.K.) and the second was called FIELDANALYSIS (written by Dr. D. I. Hoult, NRC).

1.5.2 Field correction

The apparatus available for field corrections is in the form of a shim set included as part of the gradient insert (refer Fig. 1.1). The shim set comprises independent windings where each winding generates the field of a spherical harmonic component. Each shim winding can be energized with steady current from individual shim power supplies. Ideally, each field produced by individual shim windings is orthogonal to other shim winding fields. However, this orthogonality is rarely achieved in the manufacture of shim windings. Unwanted components are usually of lower order than the spherical harmonic primarily produced. In the case of the shim set for the 9.4T magnet, the unwanted components could be 20% of the total

shim winding field generated. In the higher orders, e.g. 4th order, the primary component may represent only half of all the harmonics fields produced. The correct current to be used in each shim winding may be determined in three ways.

In Method 1, a human operator makes systematic adjustments of the current via a shim control module, with a water sample (not necessarily small) and probe placed at the centre of the magnet. The NMR signal is Fourier transformed to reveal a frequency spectrum corresponding to the magnetic environment at the position of the sample. When the field is homogeneous, the line shape becomes narrow and tall. This method can be time consuming since the shims can interact with each other and several shim trials are needed to confirm that the best (or global) shim settings have been obtained. By this method, the magnetic field is optimized only for the volume occupied by the sample and not necessarily the entire usable volume of the magnet (unless, of course, the sample fills this entire volume). This method is therefore only qualitative in nature if a final field plot is omitted.

In Method 2, shim currents are based on manufacturer-specified field sensitivities for each shim winding (where each winding is ideally equivalent to a single harmonic component). The correction currents are calculated to cancel the existing spherical harmonic components in the plotted field to render the final field uniform. This quantitative method works satisfactorily as long as the manufacturer's specifications are accurate and precise. However, some level of interaction between shim windings always exists, and it is therefore of limited practicality. This method was not utilized in this work.

In Method 3, the orthogonality of each shim winding is experimentally determined and then a calculated field correction is applied. A plot of the magnetic field with all shim currents set to zero is used as a starting "background" plot. Unit current is applied to one shim winding

only and a plot of the resulting magnetic field distribution is taken. The post shim-current field plot is subtracted from the starting field plot to reveal the effect of the shim under test. The "background subtracted" plot is then analyzed by spherical harmonic analysis. Each shim winding is then correlated with corresponding spherical harmonic components and a data base of the shim set effectiveness built.

Let the effect of the shim set in terms of generated spherical harmonics be represented by the matrix $\mathbf{S}$. Currents in the windings may be represented by the column vector $\mathbf{I}$. The effect of the shim currents is to generate the field harmonics $\mathbf{F}$ according to $\mathbf{SI}=\mathbf{F}$. It therefore follows that

$$\mathbf{I}=\mathbf{S}^{-1}\mathbf{F}, \tag{1.43}$$

where $\mathbf{S}^{-1}$ is the inverse of the shim matrix. If the matrix $\mathbf{S}$ is not square then the we would need to find the pseudo-inverse. Thus we see in Eq. (1.43), a useful relationship between the field harmonics **F**, and the shim current setting **I** related through the inverse shim matrix $\mathbf{S}^{-1}$. If we represent the initial field harmonic distribution by the vector $\mathbf{F}_0$, then the condition for final field homogeneity is $\mathbf{F}_0+\mathbf{F}_{\text{correction}}=\mathbf{0}$. Thus $\mathbf{F}_{\text{correction}}=-\mathbf{F}_0$ and the correction shim current setting is given by

$$\mathbf{I}_{\text{correction}}=\mathbf{S}^{-1}(-\mathbf{F}_0). \tag{1.44}$$

1.6 Chapter Summary.

While in principle any NMR probe can be used to measure the resonance frequency of protons in a water sample, a probe for magnetic field measurements should ideally provide a monochromatic signal in the presence of strong field gradients. To do so, the NMR sample must therefore be small - ideally a point sample. In practice, the sample necessarily has a

minimum volume since the signal strength is proportional to sample volume. However, the presence of a static field gradient in the sample, and thus a range of B_0 values will contribute to a range of received frequencies. Therefore we took measures as described in Section 1.5.2 to improve the homogeneity of the magnet field in order that a larger and more practical sample volume on the order of 1mm could be used. After magnetic field corrections were made, the probe itself should not introduce local inhomogeneity in the main magnetic field, which would have the effect of adding additional frequencies to the received NMR signal.

The goal of this thesis was therefore to build a NMR-based microprobe for magnetic field measurements with the following performance criteria: (1) the probe should yield a NMR signal with a spectral resolution (i.e. full width at half maximum) of 1Hz, and (2) a SNR in the frequency domain of greater than 1000 so that time-domain analysis of rapid ($\sim 10^{-2}$) field fluctuations could be performed reliably.

Chapter 2

MICROPROBE BASICS

2.1 Introduction

In this chapter, the basic layout of the NMR-based microprobe is introduced and construction details related to performance are discussed. Performance criteria were mainly concerned with building a probe that gave a signal with good SNR and narrow spectral linewidths. Section 2.2 describes the details of the probe's construction and operation as a RF circuit. The core of the probe is the RF coil and the NMR sample. Other components are required to transform the impedance of the RF coil to that of a coaxial transmission line for the best energy transfer from the spectrometer electronics. Section 2.3 describes the *static* probe-related field inhomogeneity arising from the diamagnetic or paramagnetic nature of the building materials used in the probe's construction. To maximize the available SNR we must place the NMR sample in close proximity to the RF coil. However, narrow linewidths are then possible only when the probe itself does not introduce any field inhomogeneity within the NMR sample volume. Thus, in general, a magnetostatic analysis must be undertaken to understand the static field distribution when any probe component is introduced into an initially uniform field.

2.2 Theory of operation.

The basic layout of a NMR-based microprobe is given in Fig. 2.1. The probe includes a RF coil L (inductor) wound about a sample vessel and sample material and made resonant

with tuning capacitor C_1. A second capacitor C_2 and a matching network are used to match the impedance of the probe to the transmission line. Probes described in Chapters 3-5 use the same electronic configuration with the main difference between them being the design of the RF coil. In the next few sections we look at each component in Fig. 2.1 separately.

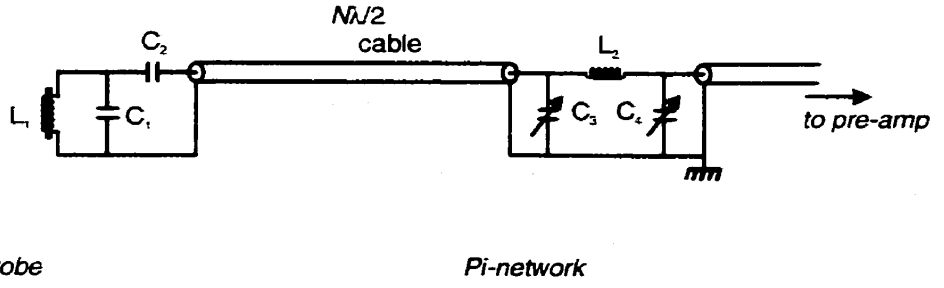

Fig. 2.1. Schematic drawing of the NMR probe used in all experiments. The first section on the left contains the RF coil (inductor), sample, and capacitors used to achieve an approximate 50Ω impedance match at the cable connection. The second section (right) is a π-section fine-tuning and matching network that can be adjusted outside the magnet bore

2.2.1 The RF Coil

The purpose of the RF coil is to provide the B_1 field used to flip spins in the sample out of alignment with B_0, and then receive the induced NMR signal. The design of the RF coil is primarily influenced by the requirements of spectral resolution and the SNR for the received signal. Good SNR is achieved by placing the RF coil as near as possible to the NMR sample to obtain a large filling factor. ('Filling factor' is the term used to indicate the proportion of volume occupied by the sample as compared to the total spatial volume (or extent) of the B_1 field.) However, the SNR is also dependent upon coil sensitivity, or the effective B_1 field produced as a function of unit current through the coil, as discussed in chapter 1. The sensitivity depends on the specific geometry of the RF coil used and is therefore discussed on a coil-by-coil basis in chapters 3-5. Good spectral resolution is achieved when the RF coil is

"magnetically transparent", in the sense that it does not perturb the magnetic field wherein the NMR sample is placed. The field perturbation is also discussed in chapters 3-5 for each coil design.

2.2.2 *Tuning and matching components*

The inductor L_1 and capacitor C_1 in Fig. 2.1 form a parallel tank circuit that has a natural resonance at the frequency $\omega_T = 1/\sqrt{L_1 C_1}$, or in hertz $f_T = 1/2\pi\sqrt{L_1 C_1}$ (Simpson 1987). The circuit has a quality factor Q of

$$Q = \frac{\omega L_1}{r} \tag{2.1}$$

where r is a small resistance not shown in Fig. 2.1 but associated primarily with the inductor L_1. Losses associated with capacitor C_1 are usually negligible as very high Q factor ($\gtrsim 5000$) capacitors are chosen for NMR applications. The impedance of the parallel tank circuit isolated from the rest of the circuit is given by (ignoring the small resistance associated with the capacitor)

$$\mathrm{Re}\, Z_{\mathrm{tank}} = \frac{\dfrac{r}{\omega^2 C_1^2}}{r^2 + \left(\omega L_1 - 1/\omega C_1\right)^2} \tag{2.2}$$

$$\mathrm{Im}\, Z_{\mathrm{tank}} = \frac{\dfrac{1}{\omega C_1}\left(r^2 - \dfrac{L_1}{C_1} - L_1^2\omega^2\right)}{r^2 + \left(\omega L_1 - 1/\omega C_1\right)^2} \tag{2.3}$$

For a frequency operating point chosen at resonance (i.e. $\omega = \omega_T$), the above equations simplify to $\mathrm{Re}\, Z_{\mathrm{tank}} = Q\omega_T L_1$ and $\mathrm{Im}\, Z_{\mathrm{tank}} = 0$. However, it is possible to chose an

operating frequency ω_a at $\omega_a < \omega_T$ such that the above equations (2.2) and (2.3) simplify to $\mathrm{Re}\, Z_{\mathrm{tank}} = 50\Omega$ and $\mathrm{Im}\, Z_{\mathrm{tank}} > 0$. The positive imaginary component of the impedance implies that the tank is inductive in nature at this frequency. The series capacitor C_2 is then chosen so that the capacitor's reactance is equal and opposite to the imaginary component of impedance from the tank circuit at frequency ω_a, i.e.

$$\mathrm{Im}\, Z_{\mathrm{probe}} = -\frac{1}{\omega C_2} + \mathrm{Im}\, Z_{\mathrm{tank}} = 0 \tag{2.4}$$

The value of C_2 is then given by

$$C_2 = C_1 \frac{r^2 + \left(\omega_a L_1 - 1/\omega_a C_1\right)^2}{r^2 - L_1/C_1 - L_1^2 \omega_a^2}. \tag{2.5}$$

Thus the probe circuit (the parallel tank and C_2) has an impedance of $Z = 50\Omega + j0\Omega$ and is then matched to the cable impedance of $Z_{\mathrm{cable}} = 50\Omega$ for an efficient transfer of energy to and from the probe. The operating point ω_a is chosen to be the same as the Larmor frequency of the NMR experiment.

It is not easy to achieve a perfect $Z_{\mathrm{probe}} = 50\Omega + j0$ result with only fixed values for C_1 and C_2. Using variable capacitors for C_1 and C_2 is undesirable since there is the possibility that the (usually) large adjustable capacitors will adversely affect the static magnetic field near the inductor when the probe is placed in the bore of the magnet. Slight mis-match in the probe impedance is therefore compensated with negligible loss by connection to a $\pi-$network by a $\lambda/2$ cable as indicated in Fig. 2.1. By the adjustment of capacitors C_3 and

C_4 we can ensure that the impedance of the probe circuit plus the $\pi-$network circuit is $Z_{\text{probe}+\pi\text{-network}} = 50\Omega + j0$ at the cable connection to the pre-amplifier or transmitter. Connection is via a passive transmit/receive switch (not shown).

2.2.3 Sample vessel

For the probe designs discussed in this paper, the sample vessel used was a long, thin capillary. The sizes and specifications of the capillaries are given in Table 2.3. The 3mm tubes came in two quality types both made of borosilicate glass. The first of these (Willmad Glass, part number 327-PP-7) was specified for use in magnetic fields of up to 9.4T. This upper field limit is based on tolerances in the tube's manufacture for inner diameter tolerance, concentricity, and camber. Deviations from a perfect circular cross section and perfectly parallel walls induce susceptibility-related magnetic field perturbations near the defect (i.e. in the volume to be occupied by the sample under study). As a precaution, tubes of a higher quality (Willmad Glass, part number 335-PP-7) suitable for use in magnetic fields of 11.7T and higher were used in order to check for any changes in the NMR data that would point out tube-related susceptibility problems. The actual volumetric magnetic susceptibility was not precisely known due to batch to batch variations in the raw materials that eventually make Pyrex 7740 glass (manufactured by Corning, USA) (Cope 1994).

Table 2.3. Capillary tubes used in this work.

NMR sample tubes from Wilmad Glass (Buena, NJ)								
	Wall (mm)	Concentricity/ Camber μ	OD (mm)	Tolerance (mm)	ID (mm)	Tolerance	Material	Product number
3mm	0.29	25/25	3.000	+0.000-0.013	2.413	+0.013-0.000	7740 Pyrex	327-PP-7
3mm	0.29	13/6	3.000	+0.000-0.013	2.413	+0.013-0.000	7740 Pyrex	335-PP-7
NMR capillary tube from Wilmad Glass (Buena, NJ)								
1mm	0.2	-	1.0	-	0.8	-	Pyrex	WG-1365-1
Fused silica capillary tubing from PolyMicro Technologies Inc. (Phoenix, AZ)								
	Wall (μm)	Coating Thickness (μm)	OD (μm)	Tolerance (μm)	ID (μm)	Tolerance	Material	Product number
150μm	75	12	150	6	75	3	Fused Silica	TSP075 150
850μm	150	24	850	25	700	12	Fused Silica	TSP700 850

The majority of experiments were with the 1mm tubes from Wilmad Glass. These Pyrex (borosilicate glass) tubes were inexpensive and easy to cut to the desired length. Their susceptibility however, was unknown. These tubes are not manufactured at Wilmad glass, but purchased in bulk from two main suppliers, Corning (USA) and Kimble (Vineland, NJ) and then repackaged. A published susceptibility specification does not exist for these tubes, but an unpublished specification (and unknown original source) gives a volumetric susceptibility for KG33 (Kimble) glass of -10.76×10^{-6} (*SI* units)(Cope, 1994).

The fused silica capillary tubing came with a polyimide coating as delivered by the manufacturer. It is possible to remove this coating using thermal or chemical methods, but this was not done for any of the experiments described here. If the coating thickness is uniform

then there should be no detrimental susceptibility-induced problems (see the discussion section 2.3.2). Several sizes of polyimide-coated tubing, ranging from 75μm ID to 700μm ID, were obtained from the manufacturer. Due to time constraints, only these two sizes were used in the construction of probes (experiments are described in chapter 3).

2.3 Magnetostatic description

2.3.1 The RF Coil

As stated earlier, good SNR is achieved by placing the RF coil as near as possible to the NMR sample to obtain a large filling factor. However, poor spectral linewidths are often obtained because the RF coil and/or the NMR sample introduce local inhomogeneity in the main B_0 field. Sometimes the local inhomogeneity can be reduced by the adjustment of magnetic field shims, but not always (Conover 1984). Almost always the local inhomogeneity can be reduced by increasing the distance between the coil and sample, but at the expense of diminished SNR. The probe designer then is faced with the difficult task of controlling or limiting the coil-induced inhomogeneity while optimizing the SNR and linewidth of the NMR signal. In practice, it is sometimes easier to trade resolution for higher SNR. In this thesis however, we are optimizing resolution first, and then SNR.

The dominant probe-related local inhomogeneity is normally due to the RF coil. Thus looking at the problem from a "reverse-engineering" perspective, we can briefly examine three methods that are used to control coil-induced inhomogeneity and then examine their effects on SNR and linewidth. One of the earliest methods relies on the fact that certain geometric shapes placed in an initially uniform magnetic field do not perturb the field uniformity in their interior. For example, an infinitely long cylindrical shell of material with magnetic susceptibility χ with its axis oriented perpendicular to an initially uniform magnetic field will have a uniform

field in its interior whose strength depends only on χ (Jackson 1975). This fact was first used by Arnold (Arnold 1956) who embedded current-carrying copper foil into a cylindrical plastic former with the same susceptibility as the copper foil, a so-called "susceptibility-matched" process. Recently, progress has been made with this symmetry technique by the use of a susceptibility-matched fluid surrounding a solenoidal RF microcoil (Olson, Peck et al. 1995; Webb and Grant 1996; Lacey, Subramanian et al. 1999). The wire windings are immersed in a matching fluid, which is contained inside a cylindrical shell. The general applicability of this method may be limited due simply to construction complexity and/or undesirable RF interactions of the matching fluid with probe components (Lacey, Subramanian et al. 1999). The availability of an appropriately matched fluid that does not give an interfering NMR signal may also be problematic. A similar symmetry technique can be used with a spherical shell, but without the requirement of a unique orientation in the field. However, the presence of a dielectric material near the coil may reduce the latter's quality factor Q and therefore SNR.

If symmetrical shapes can not be exploited, then the only conventional solutions remaining are to minimize the use of probe materials, e.g. by using foil instead of wire, or simply to keep a safe distance between the RF coil and the NMR sample, accepting the loss in filling factor and therefore SNR. A solenoidal coil in a high field application is especially difficult in this regard. The coil-induced inhomogeneity worsens with increasing field strength since fewer turns on the coil, and hence thicker wire, are needed for optimal SNR (Chen, 1989).

A direct solution without any comprise to SNR or NMR linewidths is to use zero-magnetic susceptibility wire (Anderson and Shoolery 1963; Hoult 1978; Unger and Hoult 1997). The wire is effectively "magnetically invisible" and therefore does not introduce any

local field inhomogeneity. Optimal linewidths are thereby achieved and full SNR is available as the wire can be close to the NMR sample. The winding of such a coil is also straightforward as compared to the construction techniques described above. Thus, in Chapter 4 we describe the production of wire of zero volumetric magnetic susceptibility for use in the construction of high-resolution NMR probes described in Chapter 5.

An indirect solution to the problem of coil-induced inhomogeneity is based on the magnetostatic behaviour of a long permeable (i.e. $\chi \neq 0$) cylindrical wire oriented *parallel* to a uniform magnetic field (Landau 1984, (Unger and Hoult 1999). The static magnetic field near the cylinder is not disturbed and the NMR sample can be placed immediately adjacent to it. The wire and its current return path –essentially a shorted transmission line- generate the required B_1 field. Coil-induced inhomogeneity is therefore eliminated and very narrow linewidths are possible. As well, ordinary materials such as copper wire can be used in the construction of the line. A disadvantage with this design is that SNR is compromised due to the low filling factor. The theory and construction of high-resolution NMR probes using this design are described in Chapter 3.

2.3.2 Sample and sample vessel

In this section, we determine the magnetostatic effect of the water-filled capillary tube on an initially uniform magnetic field. For the sake of clarity, we start with the artificial case of a cylinder of water in a uniform magnetic field, and then progress to the case of a water-filled capillary.

Neither the sample vessel nor the sample materials were made of "magnetic" materials (materials containing Fe, Co, or Ni). However, they did posses small magnetic character, either diamagnetic or paramagnetic, which resulted in their becoming weakly magnetized when

placed in a strong magnetic field. The macroscopic magnetic moment induced may be written as $\mathbf{M}(x', y', z')$ where the primes indicate that the magnetisation is limited to the volume of the sample and vessel.

The infinitely long cylinder falls into the general class of ellipsoids, and therefore when placed in a uniform field in any orientation, the field within the cylinder is also uniform, but in general not parallel to $\mathbf{B}_0$ (Landau and Lifshitz 1984). The field inside is parallel to $\mathbf{B}_0$ when the capillary is parallel or transverse to the external field. When the capillary is transverse, the value of the field inside is given by

$$\textit{Cylinder:} \qquad \mathbf{B}_{inside} = \mathbf{B}_0\left(1+\frac{\chi}{2}\right), \quad \chi \ll 1 \tag{2.6}$$

where the susceptibility χ is say that of the water sample. The field outside the cylinder is given by (Hauser 1971)

$$\mathbf{B}(r,\theta)_{outside} = \mathbf{B}_0 + \frac{\chi B_0}{2}\frac{a^2}{r^2}\left(\cos\theta\,\hat{e}_r + \sin\theta\,\hat{e}_\theta\right), \; \chi \ll 1 \tag{2.7}$$

with the geometry as defined in Fig. 2.1. Of course the field outside the cylinder is only of secondary interest, the primary concern being the field in the volume occupied by the water.

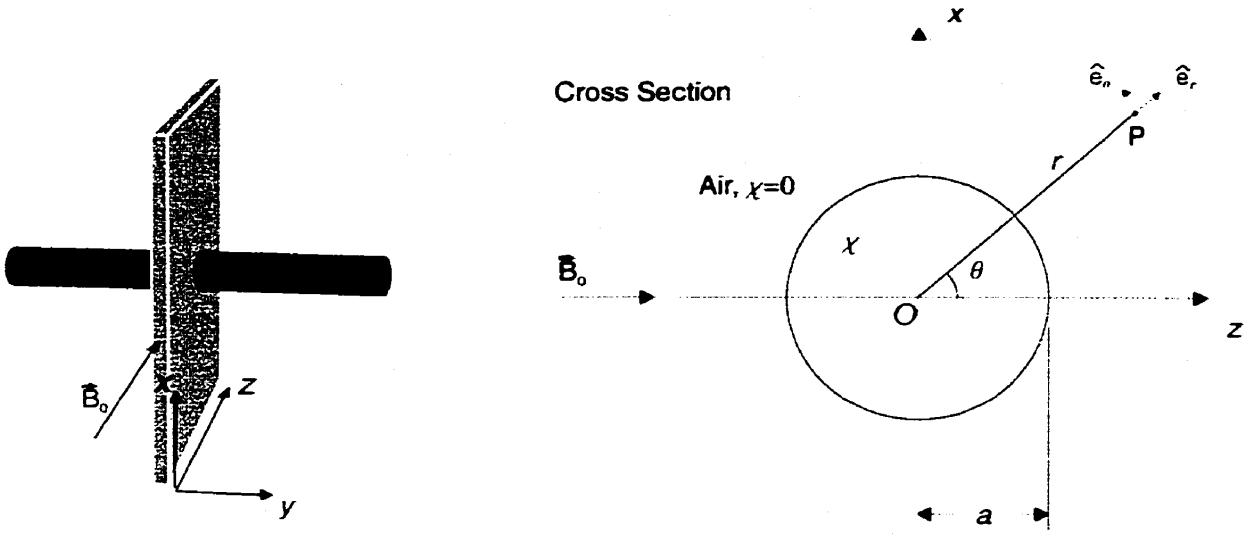

Fig. 2.2. Cross-section of a cylinder with a radius a and associated volume magnetic susceptibility χ, oriented perpendicular to a uniform magnetic field $\mathbf{B}_0$ in the circular-cylindrical co-ordinate system (r, θ).

If the susceptibility of the glass walls of the capillary and water were the same, then the discussion would be complete. In general, however, these susceptibilities do not match and the effect on the final magnetic field must be re-evaluated.

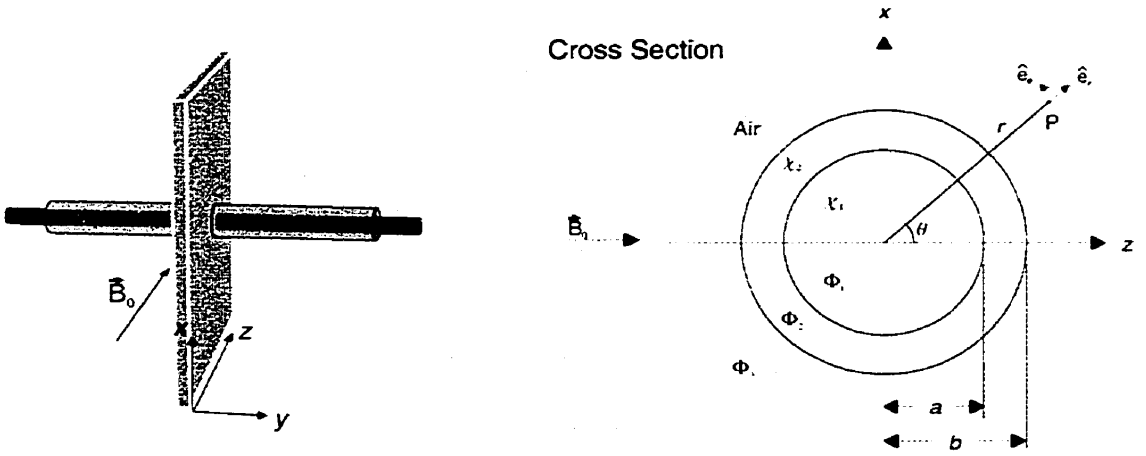

Fig. 2.3. Cross section of a co-axial cylinder with an inner core (e.g. water) of radius a and associated volume magnetic susceptibility χ_1, and an outer layer (e.g. glass) with inner and outer radii a and b respectively and associated susceptibility χ_2, oriented perpendicular to a uniform magnetic field $\mathbf{B}_0$ in the circular-cylindrical co-ordinate system (r, θ). Φ is the magnetic scalar potential.

We start with Laplace's equation $\nabla^2\Phi = 0$ as well as assuming a linear relationship $\mathbf{B} = \mu\mathbf{H}$ for the materials we will encounter in this application. For water, glass, and fused quartz χ_m is small and negative, -9.035×10^{-6} (Figgis and Lewis 1965), $\sim -110\times10^{-6}$, and $\sim -62\times10^{-6}$ - respectively (Grant and Phillips 1975). (An exact number for the susceptibility of glass is not usually possible since the formulation changes from batch to batch.) A solution of Laplace's equation for the geometry of a cylinder can be found in polar coordinates (r,θ), - see Fig. 2.3 (Binns, Lawrenson et al. 1992). The general solution may be written as

$$\Phi(r,\theta) = \sum_{m=1}^{\infty}\left(c_m r^m + d_m r^{-m}\right)\left(g_m \cos m\theta + h_m \sin m\theta\right), \tag{2.8}$$

where m takes all integral values between 1 and ∞ and c_m, d_m, g_m and h_m are constants. In our geometry we have symmetry about the z-axis so that $\Phi(r,\theta') = \Phi(r,-\theta')$ which implies there are no sine terms in the solution. The general form of the potential function then reduces to

$$\Phi(r,\theta) = \sum_{m=1}^{\infty}\left(c_m r^m + d_m r^{-m}\right)\cos m\theta. \tag{2.9}$$

Separate potentials Φ_1, Φ_2, Φ_3 are written for each of the three regions of space shown in Fig. 2.3. The values of the constants c_m and d_m are determined by the boundary conditions at the surfaces $r = a$, $r = b$ and these are that the potential Φ and the radial components of $\mathbf{B}$ be continuous there. Further the boundary condition at infinity is one of potential gradient. That is, at an infinite distance from the water-filled capillary, the field strength is uniform and its radial component is

$$H_0 \cos\theta = -\frac{\partial\Phi_3(r,\theta)}{\partial r} \tag{2.10}$$

Now

$$\frac{\partial \Phi_3(r,\theta)}{\partial r} = \frac{\partial}{\partial r}\sum_{m=1}^{\infty}\left(c_m r^m + d_m r^{-m}\right)\cos m\theta$$
$$= \sum_{m=1}^{\infty}\left(mc_m r^{m-1} - md_m r^{-(m+1)}\right)\cos m\theta \qquad (2.11)$$

from which it is seen that m can have the value unity only and hence, substituting $m = 1$ and $r = \infty$, that $c_3 = -H_0$. Thus for the outer air space, Eq. (2.9) reduces to

$$\Phi_3(r,\theta) = \left(-H_0 r + \frac{d_1^{\text{region 3}}}{r}\right)\cos\theta .$$

Further, as the field at the origin cannot be infinite, d_m=0 and $m \geq 1$ for region 1. Similarly, as the field at infinity cannot be infinite for region 3, c_m=0 for m>1. The potentials in the three regions are thus given by

$$\Phi_1(r,\theta) = c_1 r\cos\theta$$
$$\Phi_2(r,\theta) = \left(c_2 r + \frac{d_2}{r}\right)\cos\theta \qquad (2.12)$$
$$\Phi_3(r,\theta) = \left(-H_0 r + \frac{d_3}{r}\right)\cos\theta$$

where the subscripts now represent the region associated with the constant (and no longer the order m).

Expressing the equality of the radial components of the magnetic B field and of the tangential components of the magnetic H field (or its equivalent, the scalar potential) on opposite sides of the air-glass-water interface gives

$$\begin{aligned}
\mu_3\left(\frac{\partial\Phi_3(r,\theta)}{\partial r}\right)_{r=b} &= \mu_2\left(\frac{\partial\Phi_2(r,\theta)}{\partial r}\right)_{r=b} \\
\Phi_3(r,\theta)\big|_{r=b} &= \Phi_2(r,\theta)\big|_{r=b} \\
\mu_2\left(\frac{\partial\Phi_2(r,\theta)}{\partial r}\right)_{r=a} &= \mu_1\left(\frac{\partial\Phi_1(r,\theta)}{\partial r}\right)_{r=a} \\
\Phi_2(r,\theta)\big|_{r=a} &= \Phi_1(r,\theta)\big|_{r=a}
\end{aligned} \tag{2.13}$$

Differentiating Φ_1, Φ_2, Φ_3 and substituting in the interface boundary conditions, Eq. (2.13) yields

$$\begin{aligned}
\mu_3\left(-H_0 - \frac{d_3}{b^2}\right) &= \mu_2\left(c_2 + \frac{d_2}{b^2}\right) \\
-H_0 b + \frac{d_3}{b} &= c_2 b + \frac{d_2}{b} \\
\mu_2\left(c_2 - \frac{d_2}{b^2}\right) &= \mu_1 c_1 \\
c_2 a + \frac{d_2}{a} &= c_1 a
\end{aligned} \tag{2.14}$$

We now have four equations and four unknowns, i.e. (c_1, c_2, d_2, d_3). Solving for these unknowns we have

$$\begin{aligned}
c_1 &= -\frac{2H_0}{2+\chi_1+2\chi_2} \\
c_2 &= -\frac{(2+\chi_1+\chi_2)H_0}{2+\chi_1+2\chi_2} \\
d_2 &= \frac{a^2(\chi_1-\chi_2)H_0}{2+\chi_1+2\chi_2} \\
d_3 &= -\frac{a^2\left(\chi_1-\chi_2\left(1-b^2/a^2\right)\right)H_0}{2+\chi_1+2\chi_2}
\end{aligned} \tag{2.15}$$

Finally using $\mathbf{H} = -\nabla\Phi$ and $\mathbf{B} = \mu\mathbf{H}$ we find that the solutions for regions 1, 2, and 3, neglecting the susceptibility of air and end effects, are given by

$$\begin{aligned}\mathbf{B}_1 &= \mu_1 \frac{2(1+\chi_2)\mathbf{H}_0}{2+\chi_1+2\chi_2} \\ &\cong \mathbf{B}_0\left(1+\frac{\chi_1}{2}\right), \qquad \mu_1 = \mu_0(1+\chi_1),\ \chi \ll 1\end{aligned} \tag{2.16}$$

$$\begin{aligned}\mathbf{B}_2(\theta) &= \mu_2 \frac{(2+\chi_1+\chi_2)\mathbf{H}_0}{2+\chi_1+2\chi_2} + \mu_2 \frac{a^2(\chi_1-\chi_2)H_0}{2+\chi_1+2\chi_2}[\cos\theta\,\hat{\mathbf{e}}_r + \sin\theta\,\hat{\mathbf{e}}_\theta] \\ &\cong \mathbf{B}_0\left(1+\frac{\chi_2}{2}\right), \qquad \mu_2 = \mu_0(1+\chi_2),\ \chi \ll 1\end{aligned} \tag{2.17}$$

$$\begin{aligned}\mathbf{B}_3(r,\theta) &= \mu_3\mathbf{H}_0 + \mu_3 \frac{H_0 a^2\left(\chi_1 + \chi_2\left(b^2/a^2 - 1\right)\right)}{r^2(2+\chi_1+2\chi_2)}[\cos\theta\,\hat{\mathbf{e}}_r + \sin\theta\,\hat{\mathbf{e}}_\theta] \\ &\cong \mathbf{B}_0 + \frac{B_0 a^2}{2r^2}\left[\chi_1 + \chi_2\left(\frac{b^2}{a^2}-1\right)\right][\cos\theta\,\hat{\mathbf{e}}_r + \sin\theta\,\hat{\mathbf{e}}_\theta], \qquad \mu_3 = \mu_0,\ \chi \ll 1\end{aligned} \tag{2.18}$$

In the volume occupied by the water, (region 1) we see that the magnetic field differs only by a constant factor from that of the initial uniform field. In other words, the field inside the capillary is also uniform. To ignore the end effects of the capillary, the length of the capillary compared to its outer diameter should be on the order of, or greater than, 10:1. This estimate is based on considering the ends of the capillary as small dipole moments whose field generated diminishes as r_0/r^3 where r_0 is the radius of the capillary end and r is simply the distance from the end itself.

In reality, the capillary tubes are never perfectly circular in cross-section, and the above model for the magnetic field is only the starting point for an accurate calculation. The volume of the capillary is divided into two parts: (i) a capillary with a perfect circular cross-section, and (ii) the volume outside the capillary. Imperfections in the capillary can be considered as part of

(ii) in the above model where the perturbation at the field point $\mathbf{r}(r,\theta,\phi)$ due to a volume element dV located at $\mathbf{r}'(r',\theta',\phi')$ is given by (Chen and Hoult 1989)

$$dB_z(\mathbf{r},\mathbf{r}') = \chi B_0 dV \sum_{n=0}^{\infty}\sum_{m=0}^{n}\left\{\begin{array}{l}\varepsilon_m \dfrac{(n-m+2)!}{(n+m)!} \\ \times\left(\dfrac{1}{r'^{n+3}} P_{n+2,m}(\cos\theta')\cos m(\phi-\phi')\right) r^n P_{nm}(\cos\theta)\end{array}\right\} \tag{2.19}$$

where χ is the susceptibility and ε_m is the Neumann factor $\varepsilon_0 = 1, \varepsilon_{m\neq 0} = 2$. Eq. (2.19) is also useful to the micro-probe designer in calculating the perturbing effect of other objects, e.g. chip capacitors, that may be near the NMR sample, and may therefore affect the linewidth of the received signal. Other researchers have also looked at the magnetostatic perturbing effect of the sample shape on the NMR linewidth, e.g. (Belorizky, Gorecki et al. 1990).

2.3.3 Capacitors

Small high Q capacitors often have a ferromagnetic component due to metals (most often nickel) used in their construction. Even the so-called non-magnetic versions used in NMR have strongly paramagnetic materials which result in their becoming weakly magnetized when placed into the magnet bore. The position of the tuning and matching capacitors with respect to the NMR sample is thus a critical magnetostatic consideration if optimal line width and resolution are to be achieved. Put bluntly, capacitor-induced static field gradients in the sample are to be avoided. A theoretical understanding of the effects of capacitor magnetization on the local field is very difficult due to the complex structure and unknown susceptibilities of the materials used in its construction. We therefore determined the effect of capacitor magnetization on the static local field by an experimental approach.

The high-Q non-magnetic capacitors used (see Fig. 2.4) were manufactured by Dielectric Laboratories Inc. with values in the range 0.1-10pF as required. (Q≈2000 for the 2pF value at 400MHz and Q≈10000 for the 0.5pF value at 400MHz ; quoted breakdown voltage of $500V_{DC}$.) Typical precision was in the range of 5-10%. The construction of these capacitors involves layering several thin foils in flat layers separated by ceramic dielectric. The termination material is a silver-palladium alloy. (A nickel alloy material is used in the termination of the magnetic version.) Palladium has a relatively high magnetic susceptibility, $\chi_{Pd} = 804.2 \times 10^{-6}$.

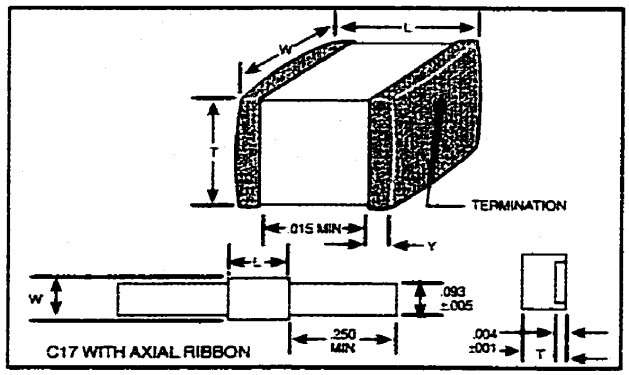

Fig. 2.4. Multi-layer chip capacitor used in all probes in this work. Dimensions: L=W=2.8mm, T=2.5mm, and Y=0.4mm.

A testing device was developed using a small NMR microprobe (shown in Fig. 2.5) to detect changes in the local magnetic field as an object under test was moved by. NMR experiments were performed on a 9.4T (400MHz) wide-bore (21cm) imaging magnet described in Chapter 1. The advantage of a high field system is that the susceptibility artefacts scale as B_0 field strength, which for our non-traditional purposes makes them easier to detect. Linear field inhomogeneity introduced into the magnet field due to the presence of the test device was shimmed out using the x, y, and z shims. The shim values were then held constant for further experiments. Drift of the field of the magnet was not a problem in the time scale of

the experiments. Transmitter power and pulse duration were the same for all samples and the flip angle was kept well below 90 degrees to ensure a linear response. Further experimental details involved in acquiring the NMR signal are described in detail in Chapter 4.

The NMR microprobe shown in Fig. 2.5 was a slightly modified version of a microprobe described in Chapter 4 (see Fig. 4.10). The probe design presented in Chapter 4 was used here because it had minimum field perturbations associated with its presence in the B_0 field. The modification primarily involved adding a long hollow tube next to the water sample so that a test object could be brought near the active volume of the probe in a controlled way. The length of the hollow tube was chosen so that the magnetostatic end effects of the tube would not perturb the magnetic field at the middle. As described in Chapter 4, the NMR signal was received from only a small region near the wire loop. A test capacitor was placed in the hollow tube and attached to a thin silk thread. (The silk thread was assumed to have negligible magnetic susceptibility compared to the capacitor under test. This assumption is based on the volume of the silk used in the thread as compared to the relatively large capacitor.) The capacitor was then pulled through the hollow tube in short increments while the effect on the NMR signal (i.e. the free induction decay) was observed and recorded. The raw data then were in the form of {position, FID} pairs.

Each free induction decay was Fourier transformed to show the real part of the frequency spectrum. Sample spectra are shown in Fig. 2.6. The spectral shape and frequency changed substantially as the capacitor was brought close to the active NMR volume. Since the exact relationship between spectral shape and peak position is difficult to relate directly to a theoretically expected lineshape, a more practical approach, the integral width of the spectrum shape, was used to characterize the changes. The frequency range from 10% to 90% of the

integral curve was defined as the "integral width" and then plotted against the position of the test capacitor.

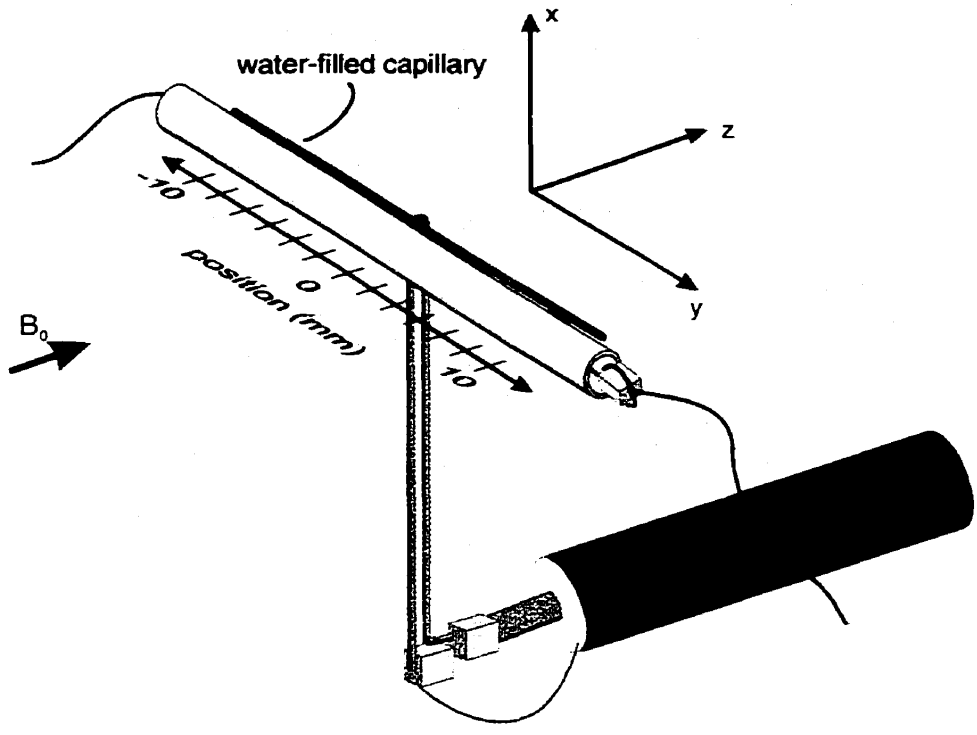

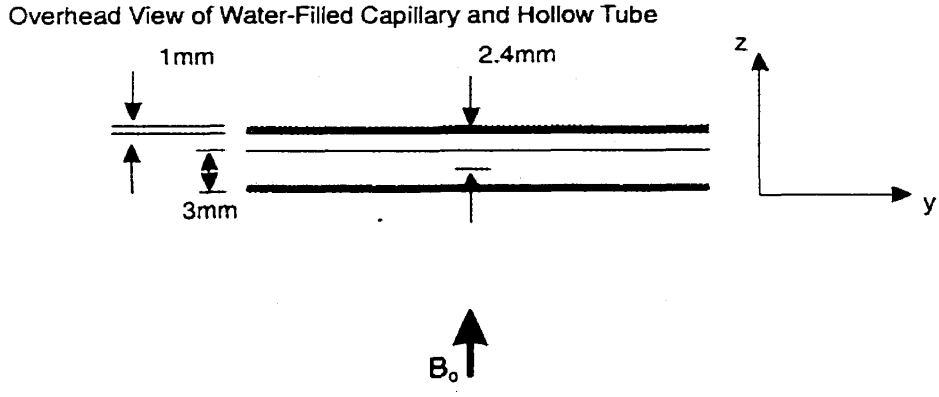

Fig. 2.5. Geometry of the NMR probe used to test susceptibility of the chip capacitors. The basic design of the probe is taken from the design presented in Fig. 4.10. A test capacitor would be inserted into one end of the larger capillary tube and moved through it in 1mm increments while observing the effect on the NMR signal. The green line represents the silk thread which is attached to the test capacitor.

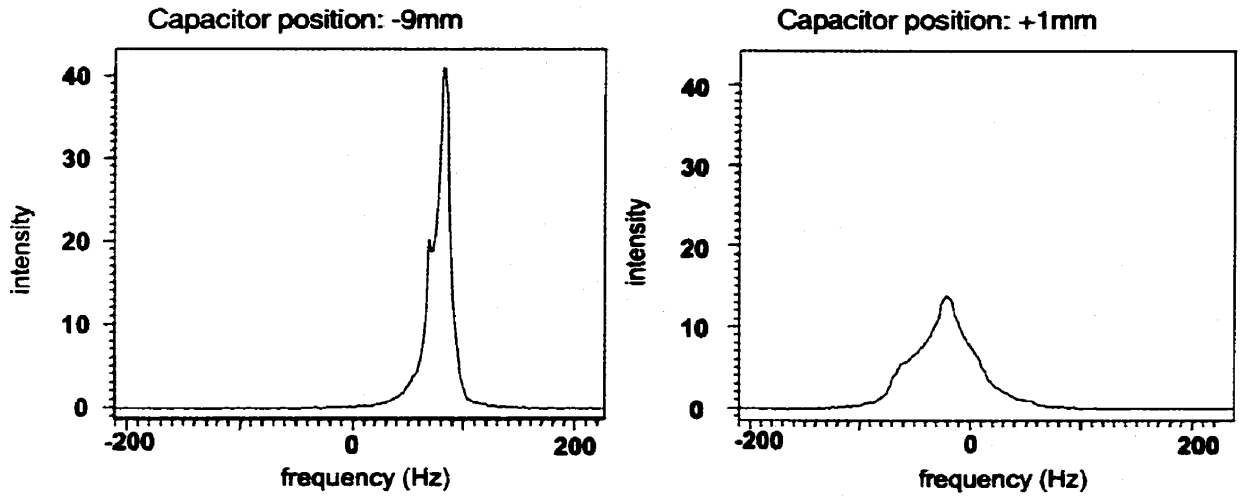

Fig. 2.6. Fourier transforms for two different test capacitor positions during the capacitor susceptibility tests. As seen in the Fourier transforms the shape of the NMR signal varies considerably.

We see from Fig. 2.7 that the maximum in the plot occurred at an arbitrary capacitor position of 1mm. The "background" level for the integral width was approximately 30Hz. The capacitor positions that rise above the 30Hz "background" are approximately ±4mm on either side of the integral width maximum. Thus, we can only make the rather weak recommendation that these capacitors should then be positioned at least 4mm from the active NMR volume in any probe design in order to obviate the effect of local field inhomogeneity due to the capacitors when the integral width is required to be below 30Hz. The baseline must be reduced further (ideally $\leq$ 1Hz) to make a recommendation for a safe capacitor distance at integral widths less than 30Hz.

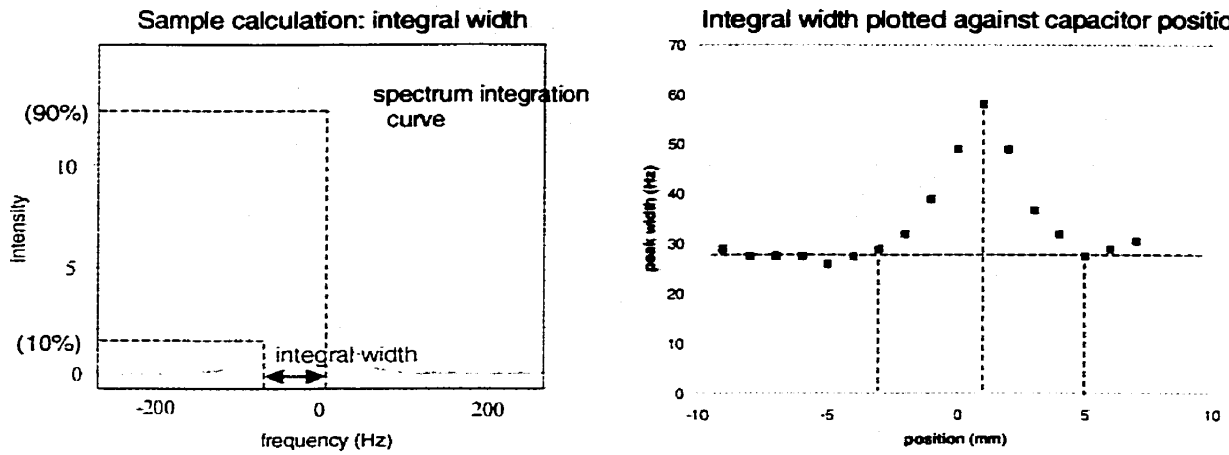

Fig. 2.7. Spectral data analyzed to obtain the integral width plotted against the position of the capacitor. A sample of the integral width calculation is given in the left figure. In the right figure, the maximum integral width occurs at the 1mm position. A difference from the 0mm position could be due to the orientation of the capacitor as it was moved past the active NMR region. The integral width falls to the background level at positions –3mm, and 5mm. Therefore, only an extrapolation can be made to find the capacitor position that generates a field inhomogeneity of <1 part per billion.

2.4 Chapter Summary

The basic layout of the NMR-based microprobe was introduced and construction details related to performance were discussed. Performance criteria were mainly concerned with building a probe with good SNR and narrow spectral linewidths. To maximize the available SNR we must place the sample in close proximity to the RF coil. However, narrow linewidths are possible only when the probe does not introduce any field inhomogeneity within the NMR sample volume.

The distribution of the static magnetic field inside the sample due to the sample vessel and sample itself was studied. Since the sample and sample vessel are in the shape of long cylinders they do not create a non-uniform field in their interior. Therefore the sample and sample vessel have been effectively been removed from the magnetostatic "problem list".

The tuning capacitor C_1 in Fig. 2.1 should be placed near the RF coil to enhance circuit stability and also to maximize the circuit Q and therefore the SNR. On the other hand

the magnetostatic perturbing effect of the capacitor C_t can compromise spectral linewidths. Keeping it a reasonable distance from the NMR sample can reduce perturbations. In short, a compromise is needed.

Chapter 3

PROBE DESIGN 1. THE ALIGNED STRAIGHT WIRE

3.1 Introduction

In the following three chapters, three strategies (i.e. RF coil designs) are presented to understand and minimize the perturbing effect of the RF coil on the field to be measured (and therefore on the perturbed field in the NMR sample volume). In all three cases, the emphasis is on the achievable linewidth with a particular design. The SNR was noted in these studies, but not optimized.

Microprobe design 1 (Chapter 3)

A RF coil made from ordinary copper wire using a novel geometry such that the coil does not cause any magnetic field inhomogeneity at the sample. The RF coil necessarily must be very much bigger than the sample size in this case, and this leads to a poor filling factor, but very narrow linewidths.

Microprobe design 2 (Chapter 4)

Zero magnetic susceptibility wire is used to construct the RF coil. The theory is developed for a straight length of wire that is perpendicular to the main magnetic B_0 field. The wire is made from aluminium wire coated with a thick layer of copper. The opposite susceptibilities effectively cancel each other for a specific thickness of copper on aluminium, and thus the ensemble possesses zero magnetic susceptibility. For linewidth comparison purposes, pure copper and pure aluminium wire are used to form geometrically identical RF coils.

Microprobe design 3 (Chapter 5)

Zero magnetic susceptibility wire is used to construct a solenoidal RF coil. The solenoid axis of symmetry is oriented perpendicular to the main magnetic B_0 field. For linewidth comparison purposes, other solenoids are made from aluminium and pure copper wire.

3.1.1 Probe Design 1. The Aligned Straight Wire

This chapter describes the design and construction of a simple NMR field-mapping micro-probe based on an interesting consequence of the boundary conditions in magnetostatics. That is, a long straight wire aligned parallel with the B_0 field does not create any local B_0-induced inhomogeneity next to the wire (see Fig. 3.1). If such a wire is incorporated as the RF coil of the microprobe, then a small sample can be placed next to the aligned parallel wire in order to measure the strength of the B_0 field without the risk of field distortion related to the presence of the RF coil.

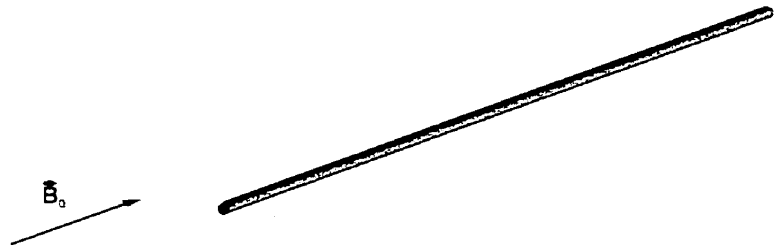

Fig. 3.1. Basic principle of the aligned parallel probe. A long straight wire that is parallel to a uniform magnetic field will not perturb the field outside the volume of the wire. This result is valid for linear or non-linear permeable materials.

There are several advantages to this design. The first is that the magnetic field next to the wire is independent of the magnetic susceptibility of the wire material. Thus, ordinary materials like copper can be used in the construction of the RF coil. The second advantage is

that the size of the NMR sample can easily be reduced in order to improve the resolution of the measurement if the original field is non-uniform. However, a reduction of sample dimensions also reduces the number of protons in the sample, and consequently the NMR signal strength. In this way, measurement resolution must be traded against signal strength. The third advantage is that this probe is easy to build. Using common materials like copper wire, the only important criteria are that the wire leads be straight, and long enough to keep magnetostatic perturbing materials far enough away from the NMR sample.

Three versions of this basic design were built and tested. The RF coil shapes are shown in Fig. 3.2. The RF coil of Fig. 3.2(a) was chronologically the first to be studied, and gave the initial positive results that verified the physical assumptions of a probe designed around an aligned straight wire as an RF coil. The RF shape of Fig. 3.2(b) was built to minimize field perturbations due to such components as the tuning and matching capacitors, or the transmission line. The "oversize" RF coil (using a total of 12 inches of copper wire) was not optimized from an electrical sense for operation at 400MHz, but rather optimized in a magnetostatic sense. The third design shown in Fig. 3.2(c) was an attempt to miniaturize the basic design while maintaining the optimal linewidth performance.

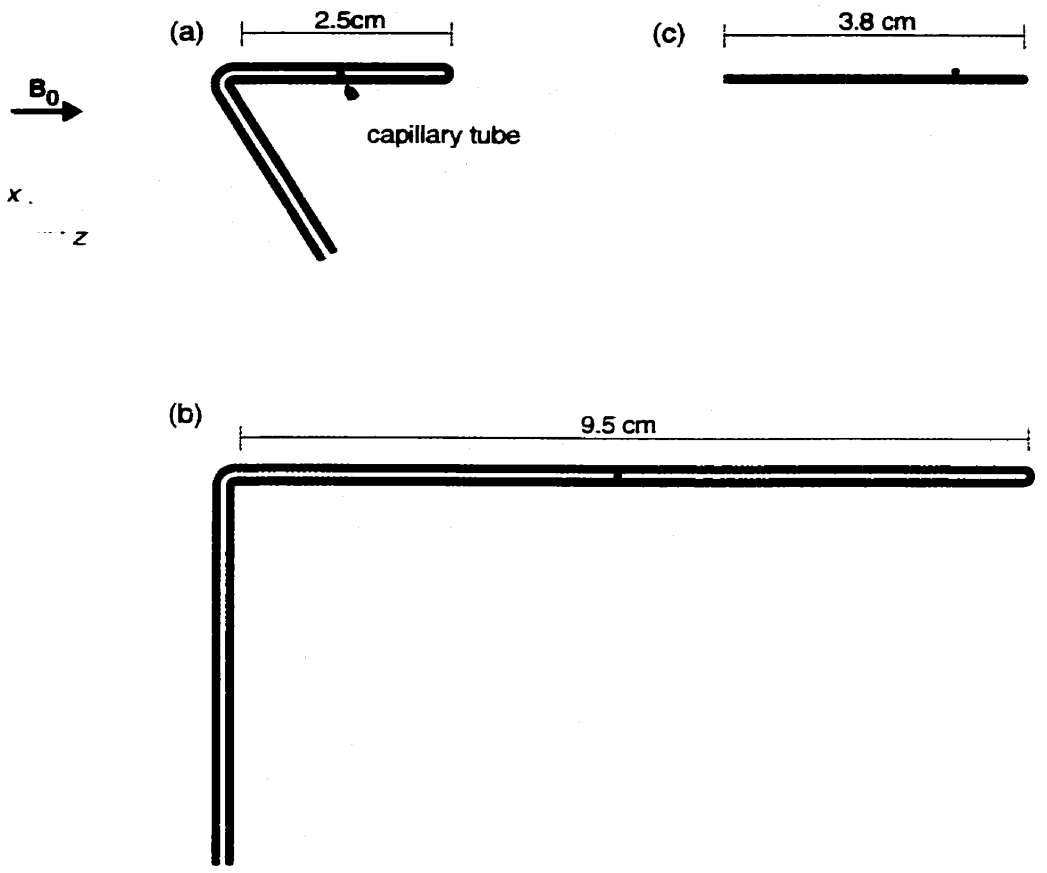

Fig. 3.2. RF coil shapes used in the aligned parallel probe design. (a) The first shape tested. It was designed for a pre-existing probe where the tuning/matching capacitors were 25mm directly below the 1mm O.D. water-filled capillary tube. (b) Long wire version used to increase the distance between the tuning/matching capacitors and the NMR sample. (c) Fine wire version used to test performance in the smaller overall size. In all cases, the closed wire ends are at least 10 wire diameters from the NMR sample. All figures shown to scale.

3.2 Theory

3.2.1 Magnetostatic Analysis

Two magnetostatic problems are relevant here: (1) a long straight wire in a uniform longitudinal field, and (2) a capillary in a uniform transverse field. In the case of the second problem, the capillary shape falls into the general class of ellipsoids, and therefore when placed in a uniform field in any orientation, the field within the (water-filled) capillary is also uniform, but in general not parallel to $\mathbf{H}_0$ (Landau and Lifshitz 1984) as described in Chapter 2.

For the first problem, that of the long straight wire in a longitudinal uniform field, there are several ways to proceed. We may use Laplace's equation with boundary conditions and then solve directly from the boundary conditions. Alternatively, this problem can be solved by considering the magnetic dipole distribution throughout the wire volume together with the appropriate boundary conditions. The boundary conditions for the magnetic **B** and **H** fields at the interface between two permeable media are obtained from the equations $\nabla \cdot \mathbf{B} = 0$ and $\nabla \times \mathbf{H} = 0$ (i.e. no free currents). At the boundary, the normal components of the magnetic **B** field, B_n, and the tangential components of the magnetic **H** field, $\mathbf{H}_t$, must be equal (Landau and Lifshitz 1984). For a long wire parallel to B_0 we then have,

$$B_{n,\text{inside}} = B_{n,\text{outside}} = 0 \text{ and } \mathbf{H}_{t,\text{inside}} = \mathbf{H}_{t,\text{outside}} = \mathbf{H}_0 . \tag{3.1}$$

This last relationship is particularly important because its validity is independent of the permeability of the wire. The magnetic **H** field is uniform within and outside the wire. Additionally, the uniformity of the external field is preserved up to the surface of the wire.

The tangential component of the magnetic **B** field, unlike its normal components, is discontinuous at the surface separating the two media. The magnitude of the discontinuity can be related to the current density on the surface. To see this consider the cylinder of permeable material oriented parallel in a uniform field in Fig. 3.3. We can see magnetic dipole moments are induced throughout the volume, as shown by the small arrows where **m** is the average dipole moment per atom. If N is the number of atoms per unit volume then

$$\mathbf{M} = N\mathbf{m} \tag{3.2}$$

where **M** is the nett magnetic moment per unit volume at a given point, the magnetization.

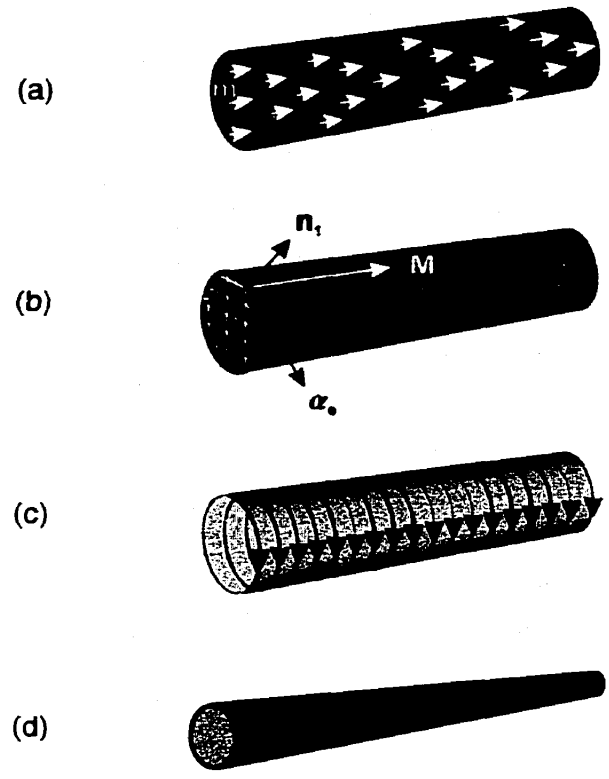

Fig. 3.3. The equivalent surface current density α_s.(a) shows a cylinder of material with individual dipole moments induced throughout the volume by an uniform magnetic field (b) the individual moments can be thought to arise from small current loops in square cells of cross-sectional area a^2, where $a \to 0$. The current in adjoining cells cancels except at the periphery of the cylinder thus giving rise to the equivalent surface current density, α_s. (c) The magnetostatic properties of a cylinder in a static field are then equivalent to the current distribution of a solenoid. (d) If the cylinder is long, then the field outside the cylinder is zero by analogy with the long solenoid result.

These individual dipole moments per atom can also be thought of as arising from Ampèrian loops (small current coils) as shown by the grid on the end face. We imagine that each cell carries a clockwise surface current of M ampères per unit length, as in the figure. Then each unit length of a cell has a magnetic moment per unit volume of a^2M ampères per unit length squared and a magnetic moment per unit volume is **M** ampères per unit length in the direction shown in the figure. As the cell dimensions are reduced, the current in one cell is cancelled by the current in adjoining cells, except at the periphery of the cylinder. Since the

cylinder has magnetization M due to the uniform $\mathbf{B}_0$ field, then the equivalent current density α_e at the surface is M. The vector equation of the equivalent, or Ampèrian, surface current density is

$$\boldsymbol{\alpha}_e = \mathbf{M} \times \mathbf{n}_1 \tag{3.3}$$

where $\mathbf{n}_1$ is a unit vector normal to the surface and pointing outward. Over the end faces, $\mathbf{M}$ is parallel to $\mathbf{n}_1$ and α_e is zero. The induced static magnetic field of a cylinder in a uniform field is therefore identical to that of a solenoid of the same dimensions with N' turns per unit length and carrying a current I such that $IN' = M$.

In particular, consider the special case of a long solenoid where the magnetic field outside the windings is zero. Therefore, if we align a real wire in the direction of a uniform magnetic field, there is no local perturbation outside the wire. An NMR sample placed next to such a wire would therefore not experience any inhomogeneity. The basic design of an NMR microprobe based on this principle is given in Fig. 3.4.

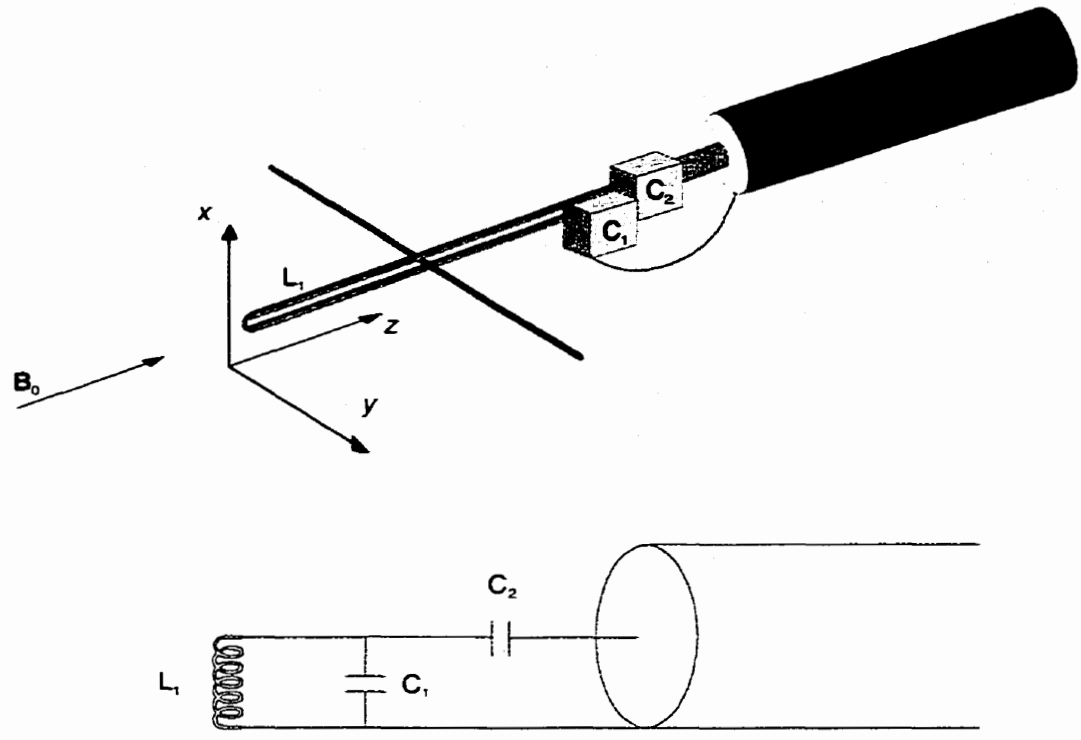

Fig. 3.4. NMR probe based on the magnetostatic properties of the aligned straight wire. The parallel wire leads are kept long enough that perturbations due to the capacitors at one end and the closed loop of the RF coil at the other end do not perturb the field at the position of the capillary. The water-filled capillary itself does not contribute any inhomogeneity in the interior water volume, as described in Chapter 2. As a rule of thumb the capillary length-to-diameter ratio must be greater than 10:1 in order to minimize its magnetostatic perturbing end effects.

3.2.2 B_1

The magnetic B_1 field produced by a long straight wire is of the form of concentric azimuthal circles as shown in Fig. 3.5. When the wire axis is aligned with the z-axis, the B_1 field is perpendicular to $\mathbf{B}_0$. The B_1 field from a single wire carrying current i is given by

$$\mathbf{B}_1(\rho) = \frac{\mu_0 i}{2\pi\rho}\hat{\mathbf{e}}_\phi \tag{3.4}$$

where ρ is the radial distance from the wire axis to the point outside the wire, and $\hat{\mathbf{e}}_\phi$ is the azimuthal unit vector. The B_1 field equation for a wire pair as shown in Fig. 3.5 would be the

vector sum of two magnetic B_1 field equations as given in Eq. (3.4). If we restrict our attention to the field along the x-axis, then for the wire pair,

$$B_1(x)_{y=0} = \frac{\mu_0 i}{2\pi} \frac{1}{\left(d/4 - x^2/d\right)} \tag{3.5}$$

Since current is flowing in opposing directions in each wire, the B_1 fields from each wire add constructively in the region between wires segments and cancel above and below the wires, but not completely to zero.

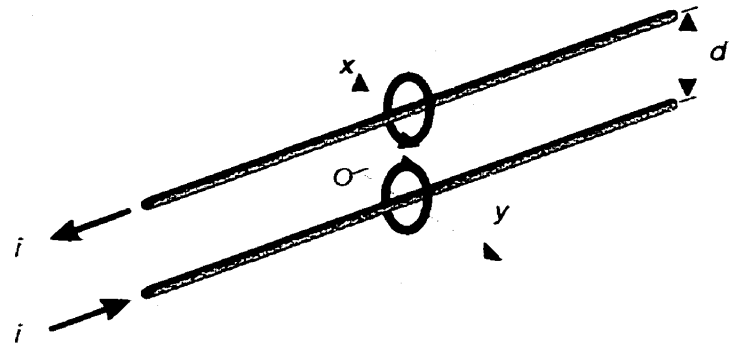

Fig. 3.5. $\mathbf{B}_1$ field from a pair of current carrying long straight wire with the current in flowing in the opposite direction. The lines of **B** form concentric closed loops around the wire that are reinforced in the space between the wires and partially cancel above and below the wires.

The region of highest sensitivity, i.e. (B_1/i), is at the position $x = y = 0$ as seen from Eq. (3.5). Therefore, the optimum location for the capillary tube in terms of SNR is between the two wire segments. However, the capillary could be placed above the top wire or below the bottom wire for some special construction requirement at the expense of a reduction in SNR.

The strength of the B_1 field in the long water-filled capillary in Fig. 3.4 defines the size of the "active region" of the water sample. By the principle of reciprocity, the volume of water that is affected by the transmitted B_1 pulse, i.e. whose spins are flipped, is also the volume of water that generates the NMR signal to be received. From Eq. (3.4) we see that the field B_1

drops off as $|1/y|$ along the axis of the water-filled capillary. Therefore, the active region of the water sample extends from $y = 0$ roughly up to a distance of about one wire radius on either side of $y = 0$. Low flip angles must be used, e.g. less than 10°, to ensure that only spins near the wire are excited, otherwise spins at a considerable distance from the wire can be flipped and the active sample region will be undesirably large.

3.2.3 Signal-to-noise Ratio

The SNR can be estimated by continuing from Eq. (1.19) in Chapter 1,

$$\mathrm{SNR} = \frac{\text{peak signal}}{\text{RMS noise}} = \frac{\left[\int_{\text{sample}} \frac{\partial}{\partial t}\left\{\left(\frac{\mathbf{B}_1(\mathbf{r})}{i}\right)\cdot\mathbf{M}_0(\mathbf{r},t)\right\}d^3r\right]_{\text{peak}}}{\mathscr{E}_{\text{noise}}}. \tag{3.6}$$

Consider as in Eq.(1.20) that the $\mathbf{B}_1$ and $\mathbf{M}_0$ fields are uniform over the NMR sample volume. This approximation is roughly valid for a small sample where the size of the sample is smaller than, or on the order of, the size of the conductor. Then the signal amplitude in the form of the peak voltage induced in the probe after a 90° pulse is given by

$$\begin{aligned}\mathscr{E}_{\text{peak}} &= \frac{K\omega_0^2\left(\frac{B_{1,xy}}{i}\right)\left[N\gamma\hbar^2 I(I+1)\right]\Delta V}{3k_B T} \\ &\propto \omega_0^2\left(\frac{B_{1,xy}}{i}\right)\Delta V\end{aligned} \tag{3.7}$$

The sensitivity in this case is relatively straightforward to compute for a sample located at the centre of the RF coil; that is mid-way between the straight wire segments (see Fig. 3.5). Using Eq. (3.5) derived in the previous section for the sensitivity, we have

$$\left(\frac{B_{1,xy}(x)_{y=0}}{i}\right)=\frac{\mu_0}{2\pi}\frac{1}{\left(d/4-x^2/d\right)} \qquad (3.8)$$
$$=\frac{2\mu_0}{\pi d}\ ,x=0\ .$$

The signal amplitude then becomes

$$\mathscr{E}_{\text{peak}}=\frac{K\omega_0^2\left[N\gamma\hbar^2 I(I+1)\right]\Delta V}{\frac{2}{3}\pi k_B T}\frac{\mu_0}{d} \qquad (3.9)$$
$$\propto\frac{\omega_0^2\Delta V}{d}\ .$$

We see in Eq. (3.9) that the signal is proportional to the square of the nuclear precession frequency, the sample volume, and inversely proportional to the distance between the straight wire segments.

The Nyquist formula as described in Chapter 1 still holds as the form of the noise in this microcoil design.

$$\mathscr{E}_{\text{noise}}=\sqrt{4k_B T R_{\text{coil}}\Delta f} \qquad (3.10)$$

where R_{coil} is used to represent all losses in the coil, e.g. RF coil, matching/tuning capacitors, eddy currents, and Δf is the spectral bandwidth. The specific form of the parameter R_{coil} used here is for a long straight wire. This has previously been determined in Chapter 1. The result found there in Eq. (1.26) is

$$\mathscr{E}_{noise}=\sqrt{4k_B T\frac{\zeta l}{p}\Delta f}\left[\frac{\mu_0\omega}{2g}\right]^{1/4}. \qquad (3.11)$$

Equations (3.9) and (3.11) can be combined to give the equation for SNR for a straight wire RF coil where the skin depth is much less than the conductor size:

$$\begin{aligned} \text{SNR} &= \frac{\text{peak signal}}{\text{RMS noise}} \\ &= \frac{K\omega_0^{7/4}\left[N\gamma\hbar^2 I(I+1)\right]\Delta V}{(128/81)^{1/4}\pi(k_B T)^{3/2}}\frac{\mu_0^{3/4}}{d}\left[\frac{pg^2}{Fl\Delta f}\right]^{1/2} \\ &\propto \frac{\omega_0^{7/4}}{d}\left(\frac{p}{l}\right)^{1/2}\Delta V \end{aligned} \tag{3.12}$$

As shown in Eq. (3.12) the SNR varies inversely with distance between the RF coil wire segments when the ratio of wire circumference to overall length (p/l) is held constant.

3.3 Microprobe construction

Probes were designed around the basic straight wire loop shown in Fig. 3.4. Three versions of this probe using three different RF coils were constructed as shown in Fig. 3.2.

In all cases, the distance from the sample to the closed end of the loop and the distance from the sample to the tuning and matching capacitors had to be great enough that static field perturbations near these objects would not extend into the sample volume of the water-filled capillary. From the closed end of the loop, the general rule for a 'safe distance' was that the loop should be greater than 10 wire diameters away from the capillary tube. Therefore, if the wire used is 0.88mm diameter, then the capillary tube should be at least 9mm from the end. The basis for this rule may be found in Eq. (2.7) from Chapter 2,

$$\mathbf{B}(r,\theta)_{\text{outside}} = \mathbf{B}_0 + \frac{\chi B_0}{2}\frac{a^2}{r^2}(\cos\theta\,\hat{e}_r + \sin\theta\,\hat{e}_\theta), \qquad \chi \ll 1 \tag{3.13}$$

where a is the radius of the wire used, and r is the distance to the field point. Our interest in this equation lies in the second term, which is the perturbation in the uniform field. For $\theta = 0°$, and a field point approximately 10 diameters away from the wire, the perturbation term in Eq. (3.13) becomes

$$\frac{\chi B_0}{2}\frac{a^2}{r^2}=\frac{\chi B_0}{2}\left(\frac{1}{20}\right)^2 \quad ,r=20a\,. \tag{3.14}$$

If we are using copper wire then $\chi \equiv -10\times10^{-6}$ and for a measurement in a 10T field the perturbation due to the closed end of the loop is approximately

$$\frac{\chi B_0}{2}\frac{a^2}{r^2}\approx\frac{10\times10^{-6}\cdot 10\mathrm{T}}{2}\left(\frac{1}{20}\right)^2=125\mathrm{nT}\,(\text{or } 5\mathrm{Hz})\,. \tag{3.15}$$

If the NMR sample is approximately 1mm in diameter then the field difference across the volume of the sample is approximately

$$\frac{\chi B_0}{2}a^2\left(\frac{1}{r_{\text{near}}^2}-\frac{1}{r_{\text{far}}^2}\right)\approx\frac{10\times10^{-6}\cdot 10\mathrm{T}}{2}\left(\frac{1}{20^2}-\frac{1}{22^2}\right)=20\mathrm{nT}\,(\text{or } 1\mathrm{Hz}) \tag{3.16}$$

Note that Eq. (3.13) can be used only as an estimate of the field perturbation since this equation was derived assuming the wire is infinitely long.

A general rule for a 'safe distance' between the water-filled capillary and the tuning and matching capacitors was more difficult. The capacitors used were all manufactured by Dielectric Laboratories Inc. and range from 0.1-10pF as required. Details of capacitors, including a test of their susceptibility, have been previously described in Chapter 2. The data presented there (refer Fig. 2.5) do not conclusively indicate a safe distance between the capacitors and the NMR sample. At a sensitivity (or peak *FWHM*) of 30Hz, the capacitors should be kept at least 4mm from the sample. However, we are designing a probe for a resolution of less than 1Hz, and the data from Fig. 2.5 do not conclusively indicate a safe distance in this case. If we assume that the capacitor-induced field perturbations behave as a dipole field (i.e. $(a/r)^3$) at distances relatively far from the capacitor (i.e. $r \gg a$) then we find

that the field drops to $1/60^{th}$ of its initial value at approximately $r = 4a$. If $a \approx 1.5$mm then we estimate 6 mm to be a safe distance from capacitor to sample. As a precaution, the capacitors used for tuning and matching were kept 25mm from the NMR sample.

The RF coil Fig. 3.2(a) was made out of copper magnet wire, 20 AWG (0.88mm diameter) and formed into the shape of a hairpin of length 50mm (i.e. using 100mm of wire) with a 1mm space between the leads. The segment length of wire aligned with $\mathbf{B}_0$ is 25mm. A thin capillary tube (outside diameter 1mm, inside diameter 0.8mm) was mounted transverse to the field (i.e. along the y-axis direction) mid-way along the aligned wire segment (i.e. 13mm from the closed end of the loop). There was the flexibility to mount the capillary tube either between the legs of the loop or above or below the wire pair. The NMR active region was then roughly a pillbox shape approximately 0.8mm in length and 0.8mm in diameter, i.e. the amount of sample within one wire radius of the capillary-wire crossing. The tuning and matching capacitors were then positioned approximately 25mm from the active NMR volume.

The components were soldered together with common commercial solder. The susceptibility of random samples of commercial solder was tested (using the basic susceptibility test as described in Chapter 4) and found to be free of ferrous contaminants and actually quite close to the predicted susceptibility of the tin/lead mixture in common solder. Both of these materials have a low volumetric magnetic susceptibility, $\chi_{Sn} = +2.40 \times 10^{-6}$ and $\chi_{Pb} = -15.9 \times 10^{-6}$.

The RF coil Fig. 3.2(b) was made out of tinned copper wire, 18 AWG (1.00mm diameter) and formed into the shape of a hairpin of length 150mm (i.e. using 300mm of wire) with a 1mm space between the leads as shown in Fig. 3.6. A thin capillary tube (outside

diameter 1mm, inside diameter 0.8mm) was mounted transverse to the field (i.e. along the x-axis direction) mid-way along the aligned wire segment (i.e. 50mm from the closed end of the loop) either between the legs of the loop or, in other experiments, above or below the wire pair as in the figure. The active region was approximately 1mm in length and 1mm in diameter located at the crossing of the copper wire and capillary. The tuning and matching capacitors were then approximately 113mm from the active NMR volume. Unfortunately, the capacitance to match to 50Ω at 400MHz was impracticably small (<1pF) due to the large inductance associated with such a long wire length and a match was not possible. (Note: typical wire lengths that would be suitable in this frequency range are more on the order of <50mm). This probe was then essentially unmatched at the frequency of operation and subsequently the power transfer, both into and out of the probe, was much reduced. From an NMR perspective on the transmit side, the poor impedance match implied a lower flip angle throughout the sample (thus a higher power setting was needed to get the required flip angle). On the NMR signal reception side, the impedance mismatch prevented an efficient energy transfer from the sample to the receiver electronics, and consequently the overall SNR was degraded.

Fig. 3.6. Photo of the long wire version of the aligned parallel (RF coil) probe.

The RF coil Fig. 3.2(c) was made out of tinned copper wire, 26 AWG (0.23mm diameter) and formed into the shape of a hairpin of length 34mm (i.e. using 68mm of wire) with approximately 0.3mm space between the leads. Various capillary tube diameters ranging from 150μm-1mm OD were separately mounted transverse to the field (i.e. along the y-axis direction) mid-way along the aligned wire segment (i.e. 17mm from the closed end of the loop). Several capillary sizes were tried with this design. If the capillary was narrow enough then it was positioned between the legs of the loop or, for larger water-filled capillaries, above or below the wire pair. The active region was approximately 0.2mm in length and 0.2mm in diameter (i.e. the amount of sample "reachable" within one wire radius approximately) located at the crossing of the copper wire and capillary. The tuning and matching capacitors were then approximately 17mm from the active NMR volume. The microprobes constructed for Chapter 3 have been summarized in Table 3.1 below.

Table 3.1. Coil design summary for RF coils based on the aligned parallel wire.

Coil Design Summary			
Ref.	**Wire diameter**	**Capillary ID/OD**	**Capillary position**
Fig. 3.2(a)	0.88mm	0.8/1.0mm	outside loop
Fig. 3.2 (a)	0.88mm	0.8/1.0mm	inside loop
Fig. 3.2 (b)	1mm	700/850μm	outside loop
Fig. 3.2 (b)	1mm	0.8/1.0mm	outside loop
Fig. 3.2 (b)	1mm	2.9/3.0mm (335-PP)	outside loop
Fig. 3.2 (c)	0.4mm	75/150μm	inside loop
Fig. 3.2 (c)	0.4mm	0.8/1mm	outside loop

3.4 NMR experiments

The experiments were performed on a 9.4T 21cm horizontal bore magnet (Magnex, U.K.) as described earlier in Chapter 1. In this section, we describe how the NMR experiments were performed using the aligned straight wire probe design. In the following subsection we briefly describe the state, or non-uniformity, of the B_0 magnetic field into which the probe was placed prior to acquiring the NMR data. We begin with an initial survey of the field followed by field corrections and relevant NMR experimental parameters.

3.4.1 Field plot

We determined the relative contributions of various spherical harmonics in the 9.4T magnet field by measuring the field strength at various points in the central region of the bore as shown in Fig. 1.2. The measurements were made in this case using an NMR-based probe with a 4mm diameter water-filled sphere. This design was not optimized for high-resolution results (i.e. narrow spectral linewidths) or SNR, but the linewidth and SNR were acceptable for this application. The field plot is normally quoted to ppm resolution over the volume of interest. Therefore, this was also the minimum linewidth resolution required for the field-plotting probe. The NMR resonant frequencies corresponding to field positions were converted to magnetic field strength using the Larmor equation in order to produce a list of magnetic field value versus position. The data were analyzed in terms of spherical harmonics using computer programs MULTISHIM and FIELDANALYSIS. The programs were in agreement and the results, the field vector $\mathbf{F}_0$, are given in Table 3. 2 under the column heading, "Initial Field Values".

3.4.2 Field correction

"Method 3" as described in Section 1.4.2, was used to make field corrections. The shim set on the 9.4T magnet comprised thirteen independent windings. Unit current was applied to a shim winding and a plot of the resulting magnetic field distribution was taken. After the "background subtraction" process (refer §1.4.2), the plot was then analysed in spherical harmonics. This was repeated for each shim and a data base was made, i.e. the shim set effectiveness matrix $\mathbf{S}$ shown in Table 3. 23.

Recall that the correction shim current settings $\mathbf{I}_{\text{correction}}$ are given by

$$\mathbf{I}_{\text{correction}} = \mathbf{S}^{-1}(-\mathbf{F}_0). \tag{3.17}$$

where $\mathbf{F}_0$ is the initial, or uncorrected field as given in Table 3. 32 under the column heading, "Initial Field Values".

Correction shim currents $\mathbf{I}_{\text{correction}}$ were applied and the field remapped. Due to experimental uncertainties in the field mapping process, the field was not perfectly homogeneous after this procedure. The remapped field was then used as input for another "cycle" of determining the correction shim winding currents. The final field after two cycles of corrections is given in the column "Corrected Field Values" with the inhomogeneity reduced to 2.3 ppm over a 10cm diameter sphere.

A further attempt was made to reduce the inhomogeneity along the z-axis using a simple polynomial fit to the field data collected along the z-axis. After corrections, the overall field had a final inhomogeneity of 3.2 ppm over a 10cm diameter sphere, but the field along the z-axis (± 5 cm from iso-centre) varied only by 75 Hz (or <0.2 ppm).

Table 3. 2. Calculated spherical harmonic values for the 9.4T imaging magnet used in this study. The Re, Im notation is used here to denote **Re** $\Rightarrow \psi = 0$ and **Im** $\Rightarrow \psi = 90°$ in Eq.(1.42).

Spherical harmonic indices (n,m)	Cartesian Descriptor	Initial Field Values (ppm), $\mathbf{F}_0$ {9.9ppm p-p}	Corrected Field Values (ppm) {2.3ppm p-p}	Axial-Corrected Field Values (ppm) {3.2ppm p-p}
$(1,0)$	z^1	1.69	-0.05	-0.17
$(2,0)$	z^2	-0.80	0.00	1.23
$(3,0)$	z^3	2.54	0.02	-0.22
$(4,0)$	z^4	-0.98	-0.01	0.10
$(5,0)$	z^5	-0.10	0.04	0.04
$(6,0)$	z^6	1.17	0.45	0.37
$\mathrm{Re}(1,1)$	x	0.30	0.06	0.10
$\mathrm{Im}(1,1)$	y	1.05	0.14	0.05
$\mathrm{Re}(2,1)$	zx	-0.28	0.00	0.02
$\mathrm{Im}(2,1)$	zy	0.10	0.01	0.01
$\mathrm{Re}(2,2)$	$x^2 - y^2$	-0.27	0.01	0.01
$\mathrm{Im}(2,2)$	xy	0.04	0.00	0.00
$\mathrm{Re}(3,1)$	z^2x	0.35	0.01	0.00
$\mathrm{Im}(3,1)$	z^2y	-0.07	-0.14	0.04
$\mathrm{Re}(3,2)$	$z\left(x^2 - y^2\right)$	0.26	0.00	-0.01
$\mathrm{Im}(3,2)$	zxy	-0.05	-0.05	-0.06
$\mathrm{Re}(3,3)$	x^3	0.01	0.01	0.00
$\mathrm{Im}(3,3)$	y^3	-0.01	-0.01	-0.01
$\mathrm{Re}(4,1)$	z^3x	-0.04	-0.06	-0.07
$\mathrm{Im}(4,1)$	z^3y	0.03	0.03	0.05
$\mathrm{Re}(4,2)$	$z^2\left(x^2 - y^2\right)$	0.00	0.02	0.01
$\mathrm{Im}(4,2)$	z^2xy	0.02	0.01	0.01
$\mathrm{Re}(5,1)$	z^4x	-0.02	0.06	0.05
$\mathrm{Im}(5,1)$	z^4y	0.03	0.04	0.02

Table 3. 3. Matrix representation of the effect of individual shim windings on the overall field. The rows represent the spherical harmonic analysis components (provided by MULTI). The columns represent the individual shim windings. Numbers are given in parts per million of the magnetic field strength.

Spherical Harmonic Component	Shim Winding Label													
	X	Y	XZ	YZ	Z	Z2	X2-Y2	2XY	Z2X	Z2Y	Z3	Z4	Z(X2-Y2)	Z(2XY)
z^1	0.02	0.02	0.02	-0.2	-1.6	0.24	-0.02	0.01	0.08	-0.55	-0.03	-0.05	-0.06	-0.02
z^2	0.22	-0.01	-0.31	-0.32	0.02	-7.08	-0.12	-0.05	-0.01	-0.02	-1.78	0.04	0.11	0.06
z^3	-0.01	-0.01	0.04	0.09	-0.03	0.14	-0.13	0.12	-0.03	0.46	9.12	-0.97	-0.09	-0.1
z^4	-0.28	0.02	-0.06	-0.01	0.04	0.06	-0.08	0.06	0.06	0.03	0.79	12.09	0.01	-0.01
z^5	0.02	0.01	-0.01	-0.09	0.05	-0.09	0.25	-0.01	0.01	-0.06	-0.21	0.26	0.08	0.1
z^6	0.33	0	0.13	0.19	0.03	0.23	0.36	0.03	-0.01	-0.08	-0.57	2.3	-0.06	-0.06
x	0.01	1.45	0.97	-0.02	-0.01	-0.28	-0.12	0.14	1.32	0.02	0.13	0.08	-0.13	-0.15
zx	-0.02	0	-5.05	0.16	0.01	-0.06	0.07	-0.06	0.11	0.04	0.19	0.07	0.02	0.06
$x^2 - y^2$	0.08	0.01	0.07	-0.08	0.01	0.03	-0.38	-0.06	0	-0.01	-0.04	0.04	-0.61	0.07
z^2x	-0.04	-0.03	-0.04	-0.03	0	0.01	0.1	-0.02	-1.61	-0.12	0	0.01	-0.01	0.01
$z\left(x^2 - y^2\right)$	0	0	-0.01	0	0	0.02	0.97	0.01	0.01	0.03	0.02	0.02	0.03	-0.01
x^3	-0.01	0	0	0	0	0.01	-0.03	0	-0.01	0	0	0	0	0
z^3x	0.01	0	0.16	0.09	0	0.04	-0.05	0.05	-0.03	-0.01	-0.01	-0.04	-0.02	-0.05
z^4x	0.02	-0.01	-0.1	-0.01	0	0.02	-0.06	-0.01	0.24	0.05	-0.03	-0.03	0.01	0.01
$z^2\left(x^2 - y^2\right)$	-0.02	0	0.01	-0.01	0	0	0.06	-0.01	0	0	0	0	-0.1	0.01
y	1.35	0.05	0.03	1	0.01	-0.02	0.41	0.07	0.07	-1.18	0.15	0.03	0.13	-0.06
zy	-0.01	-0.01	-0.27	-4.85	-0.01	-0.09	0.02	-0.1	0.04	-0.07	-0.08	0.02	-0.01	0.08
xy	0.05	0	0.03	0.02	-0.01	-0.05	0.06	0.68	-0.02	0	-0.01	0.04	-0.04	-0.7
z^2y	0.11	0	0.01	-0.02	0	0	-0.1	-0.03	-0.09	1.6	-0.02	-0.07	0.01	0.02
zxy	0	0	0.03	-0.01	0	-0.02	0.07	-0.06	0	0	0	0.02	0	0.07
y^3	0.01	0	0	0	0	0	-0.01	0	0	-0.01	0	0.01	0	0
z^3y	0	0	-0.01	0.13	0.01	0.07	-0.09	0.06	0	0.03	0	-0.03	0	-0.06
z^4y	-0.12	0.01	-0.01	-0.07	0	0.03	-0.06	-0.01	0.04	-0.23	0.07	-0.02	-0.02	0
z^2xy	-0.02	0	0	-0.01	0	0	0.01	0.1	0	-0.01	0	0	-0.01	-0.1

3.4.3 Magnetic Field Protocols

Experiments were performed in three separate magnetic field conditions: (1) the unshimmed field; (2) the shimmed field using room temperature shims to remove only magnet related inhomogneity, and (3) the shimmed field using room temperature shims to remove both magnet and probe-related inhomogeneity.

In field condition (1) we are looking for the associated spectral linewidth due to all sources of field inhomogeneity, both probe related and magnet related. This condition would be a realistic magnetic environment of a practical field measurement probe. In field condition (2) we are looking for the linewidth resolution due to field inhomogeneity related to the probe alone. This assumes the room temperature shims have been adjusted to obtain a perfectly uniform magnetic field *before* the probe is placed in the magnet. Field condition (2) is relevant for "debugging" the design of new probes since any observed inhomogeneity will be due only to the probe under test. In field condition (3) we are looking for the best performance the probe can give if used for, say, spectroscopy with the narrowest of linewidths. That is, the range of frequencies in the free induction decay signal is on the order of parts per billion of the resonance frequency.

In practice, it is almost impossible to establish field conditions (2) and (3) well. We have seen that we were unable to obtain a perfectly homogeneous gross field in the magnet, while for condition 3 with our small samples, the linear field gradient shims are of greatest import. Thus any higher order inhomogeneity produced by the probe cannot be annulled.

Condition (3) was explored as follows. With the probe in position at the magnet iso-centre, current passing through the shim windings was adjusted until the narrowest linewidth in the Fourier transform of the free induction decay was obtained. Depending on the

configuration of the RF coil and other probe components, the narrowest linewidth varied between 0.6 Hz and 10Hz. Most certainly, the limiting factor to getting better than 0.6Hz was the sensitivity (i.e. $mT/m^n/A$) of certain shim spherical harmonics. The manufacturer designed the shim winding set assuming the sample was roughly the same order of magnitude as the free bore, e.g. a suitable sample for an open bore of 12cm would be a rat with a 7cm diameter. The probes under study here are two orders of magnitude smaller than the open bore size, and the shim winding set is simply not suited to the field probe's dimensions. A simple rule must be followed; a physically small shim set for a physically small sample. Otherwise, the corrective action of almost any large dimension shim ends up looking like a linear shim on the micro-scale of the probe.

In summary, the shimming process is actually quite difficult since it is impossible to verify a uniform field with any probe used in this work, or otherwise available to the author. The following data must be interpreted in this light.

3.4.4 Data acquisition

The probe was placed at the iso-center of the magnet and a FID acquired from a single pulse experiment with the following parameters. The frequency bandwidth was 50,000Hz in order to observe a broad range of frequencies that might be present throughout the sample due to various magnetic field strengths. The acquisition time varied according to the observed length of the free induction decay. In all cases, the data were acquired until the time domain SNR ratio was $\ll 1$. The flip angle used in all cases was 10°. This was verified in several ways. The most common for a given probe was to use a fixed transmitter power and slowly increase the pulse duration while observing the effect on the free induction decay. The Bruker on-line

software can integrate the free induction decay and a maximum result implied a 90° flip angle. The pulse width was then divided by 9 to obtain the duration for a 10° flip angle.

The transmit pulse power for a given flip angle and pulse duration (typically 2-10 μs) with the RF coil design of Fig. 3.2. Coarse power adjustments were made using fixed attenuators in 10dB increments at the output of the power amplifier. For the RF coils in Fig. 3.2(a) and (b) the power setting was approximately 30W. This is a relatively high value, but it is doubtful whether the majority of this power was delivered to the probe due to an impedance mismatch at the junction of the transmission line end and the probe/π-network. For the RF coil in Fig. 3.2(c), the power setting was a more reasonable 3W.

3.4.5 Results and Discussion

3.4.5.1 Overview of Results

Linewidth results are tabulated in Table 3.4 and Fourier transforms of the free decay induction decays are given in Fig. 3.7-Fig. 3.9 for the three RF coil designs of Fig. 3.2.

Table 3.4. Aligned straight wire probe linewidth results. Coil profiles are found in Fig. 3.2. Capillary tube descriptions can be found in Table 2.1 in Chapter 2. "Capillary position" refers to the position of the capillary with respect to the closed loop of the RF coil. The magnetic field condition is described in the text. The SNR has been noted in the frequency spectrum, but this is not an optimized parameter. "NR" indicates that the spectrum was Not Recorded for off-line analysis. The value was estimated using the on-online diagnostic mode of the acquisition software.

Coil Design [capillary OD, position]	**Linewidth Performance**								
	Inhomogeneous field			**Homogeneous field**			**Shimmed field**		
	FWHM	**S/N**	**Ref.**	**FWHM**	**S/N**	**Ref.**	**FWHM**	**S/N**	**Ref.**
Fig. 3.2(a) [1mm, outside loop]	10 Hz	90	Fig. 3.7(a) /Expt. 1				7.2 Hz	1040	Fig. 3.7(b) /Expt. 2
Fig. 3.2 (a) [1mm, inside loop]	15 Hz	270	Fig. 3.7(c) /Expt. 3				5.5 Hz	1930	Fig. 3.7(d) /Expt. 4
Fig. 3.2 (b) [850μm, outside loop]	22 Hz	11	Fig. 3.8(a) /Expt. 5				0.60 Hz	20	Fig. 3.8(b) /Expt. 6
Fig. 3.2 (b) [1mm, outside loop]							0.69 Hz	15	Fig. 3.8(c) /Expt. 7
Fig. 3.2 (b) [3mm, outside loop]				1.05 Hz	600	Fig. 3.8(d) /Expt. 8	0.66 Hz	360	Fig. 3.8(e) /Expt. 9
Fig. 3.2 (c) [150μm, inside loop]				7000 Hz	60	Fig. 3.9(a) /Expt. 10			
Fig. 3.2 (c) [1mm, outside loop]				~8 Hz		NR	2.3 Hz	60	Fig. 3.9(b) /Expt. 11

These experimental results represent typical performance under the conditions stated, and are not the results of repeating the experiments in several trials. Uncertainties in the FWHM

resolution are typically less than 10% of the associated value. A sophisticated lineshape fitting to spectra was not performed, but rather a reasonable fit by drawing a smooth curve through the data was used. Care was taken to visually align the RF coil with the magnet bore axis before acquiring the data. The angle of the RF coil relative to the bore axis was not an adjustable parameter in this series of experiments. As observed from Table 3.4, not all RF coils were tested in all magnetic field conditions. More effort was spent testing the performance of the probe in a shimmed field, condition (3). This was due to the initial objective stated in Chapter 1 of reaching a linewidth (FWHM) of less than 1Hz. Once this target had been reached for a micro-size sample in a shimmed field, then further work would be directed toward reaching the 1Hz linewidth result in a homogenous field. This second goal was not fully realized at the time of writing this thesis.

By inspection of Table 3.4 we see that the most successful design with respect to spectral linewidth was that of the long wire RF coil, Fig. 3.2(b). In all combinations with different capillary tube sizes, we were able to achieve sub-1Hz FWHM results. Chronologically this was not the first design based on the aligned-wire principle. The first probe built and tested was that of Fig. 3.2(a). The encouraging results from this initial design led to the construction of the long wire RF coil, Fig. 3.2(b) and then finally the scaled-down design of Fig. 3.2(c). The linewidth results of the scaled-down design did not go below 1Hz as hoped, which indicated that the static magnet field perturbation from various probe components was not completely understood. Regardless, several observations can be made from this data in Table 3.4. and Fig. 3.7 to 3.9.

SNR was not optimized in any of the tests, so the possibility of achieving a probe design with a SNR of 1000 (or better) was not fully investigated. Certainly, this goal seems

achievable since order-of-magnitude results have been obtained, e.g. (1) 3mm capillary tube outside the RF coil windings operated in a homogeneous field (FWHM= 1.05Hz, at a S/N=600) (2) 1mm capillary tube outside the RF coil windings operated in a shimmed field (FWHM= 7.2 Hz, at a S/N=1040) and (3) 1mm capillary tube between the RF coil windings operated in a shimmed field (FWHM= 5.5 Hz, at a S/N=1930).

3.4.5.2 Specific Results

We first examine the results for the probe design of Fig. 3.2(a). All spectra related to this probe design are contained in Fig. 3.7. The water-filled capillary tube was positioned both inside the loop formed by the RF coil and outside the loop in both inhomogeneous and shimmed fields. This change in position affected the linewidth slightly, and at least doubled the SNR in the frequency spectrum. Roughly speaking, a factor of two improvement was expected in the SNR. In the case of the inhomogeneous field, the FWHM increased on placing the capillary inside the RF coil loop. This result is deceptive, however, for examining the line shapes of Fig. 3.7(a) and (c) we see that the shape of the curve has changed considerably and a full width at half maximum analysis is misleading.

In a shimmed magnetic field the linewidth improved, but not to sub-1Hz values. This indicated a local magnetic field inhomogeneity that could not be "shimmed out" using the room temperature shim set. The line shapes were more symmetric in the shimmed field condition as seen in Fig. 3.7(b) and (d). However, upon close inspection, a slight shoulder in the high field side of the peak indicated a $1/r^2$ dependence within a large proportion of the NMR sample. The $1/r^2$ dependence likely originated from the interaction of the main B_0 field with a diamagnetic object, for example the capacitors used in tuning and matching. These suspicions were addressed in the next generation of the aligned straight wire probe resulting in

the RF coil shown in Fig. 3.2(b). Here the capacitor-NMR sample distance was increased from 25mm to 75mm and the probe was built on a uniform cylindrical former (refer Fig. 3.6).

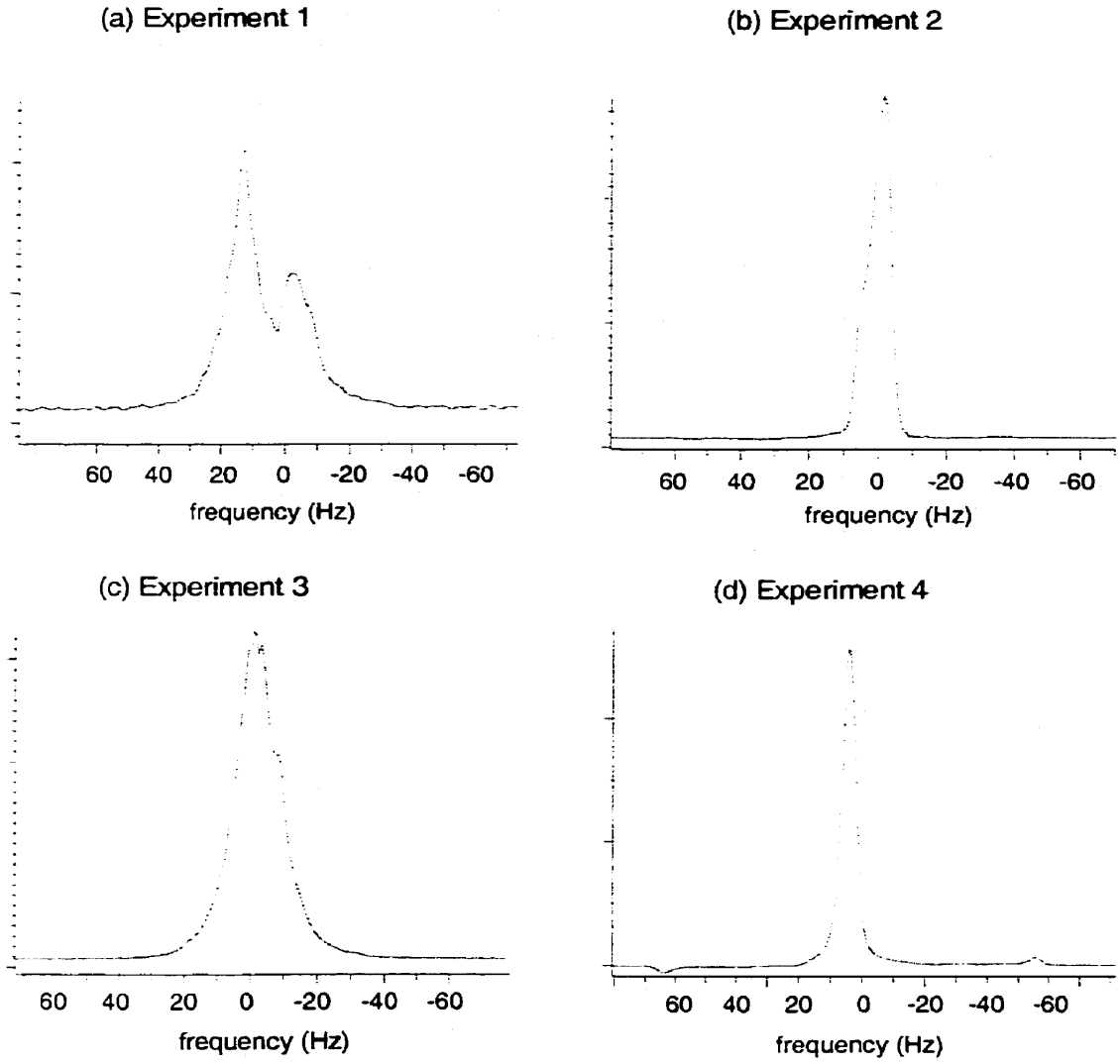

Fig. 3.7. NMR spectra resulting from RF coil design Fig. 3.2(a) with a 1mm water-filled capillary tube. Spectra are correlated to data in Table 3.4. Experiment 1 was obtained with the capillary outside the wire loop and in an inhomogeneous field. Experiment 2 was obtained with the capillary outside the wire loop and in a shimmed field. Experiment 3 was obtained with the capillary inside the wire loop and in an inhomogeneous field. Experiment 4 was obtained with the capillary inside the wire loop and in a shimmed field. Following NMR convention, the direction of increasing frequency point toward the left. The origin of frequency axis has been chosen arbitrarily. Fourier transformed spectra intensities are relative.

The long straight wire version of the align wire probe Fig. 3.2(b) gave the best linewidth results (see Fig. 3.8). The design was tested with three different water-filled capillary sizes in inhomogeneous, homogeneous, and shimmed fields. In an inhomogeneous field, the linewidth of the frequency spectrum was 22Hz using the 700/850μm ID/OD tube. This was the same order of magnitude as found in the previous probe design for the inhomogeneous field condition.

In a homogeneous field, the linewidth reduced to 1.05Hz using the 3mm water-filled capillary tube. The large SNR in this case was likely due to a larger volume of flipped spins in the water sample. The 3mm capillary tube is not appropriate for use in a micro-magnetic field sensor application, but was useful here to investigate the benefit of using high precision glassware for the sample volume.

In a shimmed field, the linewidth reduced to 0.6~0.7Hz, in all capillary sizes. When using the 850μm capillary the peak appeared symmetric although slightly broadened at the peak base. This was likely due to a high order (3+) odd spherical harmonic inhomogeneity in the interior volume of the NMR sample. The peak shape was also symmetric in the case when the 1mm capillary was used, but apparently without the higher odd order spherical harmonic inhomogeneity present. The width of the peak at its base was 3Hz. When using the 3mm capillary tube, the line shape changed from high even-order inhomogeneity, in the case of a homogeneous field, to that of a low-order even spherical harmonic inhomogeneity. This was likely the result of a shimming error in the effort to get the overall narrowest linewidth. Note that the observed linewidth was still significantly larger than the minimum predicted (~0.1 Hz for T_2~3s), and thus the required corrections required exceeded the capabilities of the shim set.

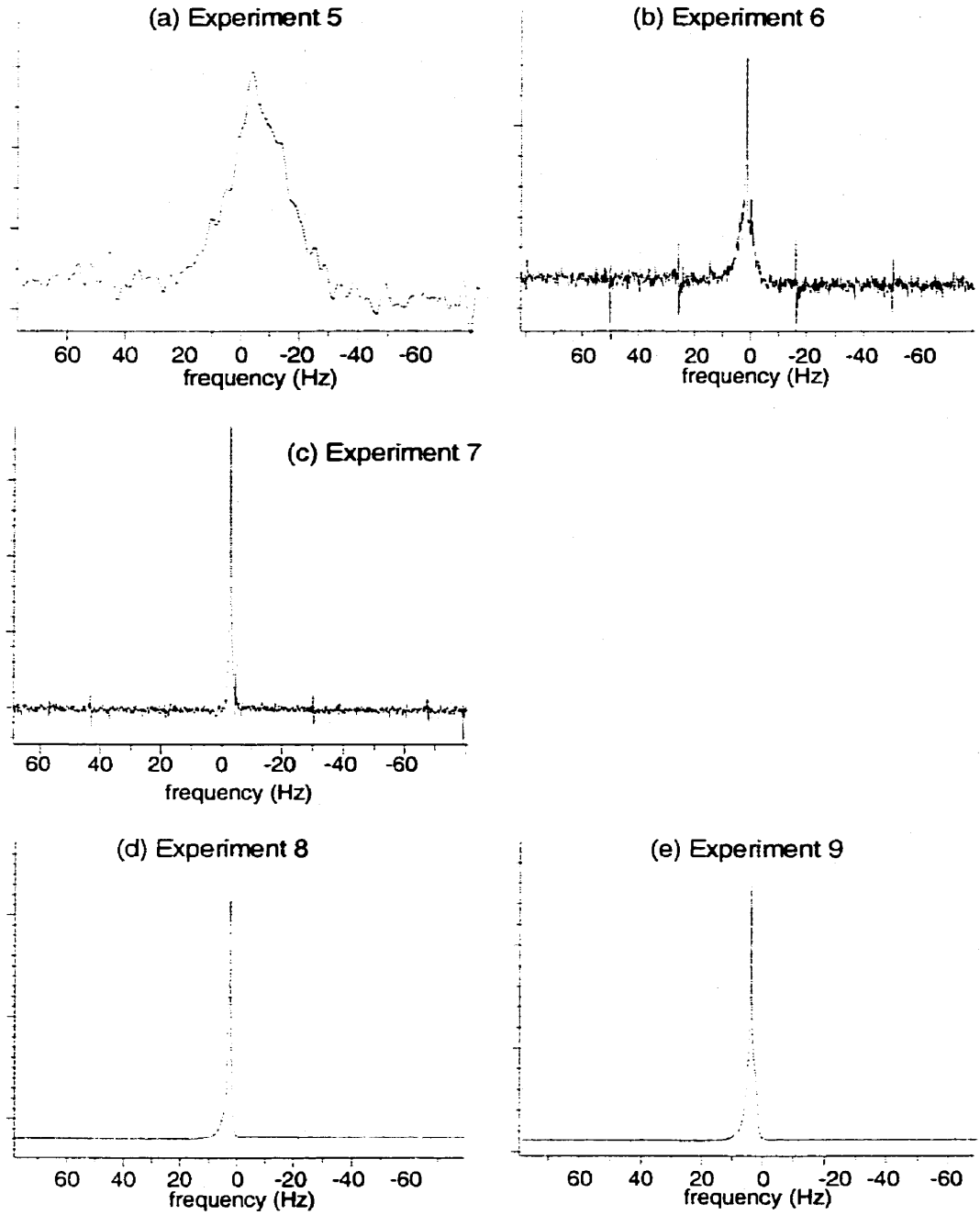

Fig. 3.8. NMR spectra resulting from RF coil design Fig. 3.2(b) with various sized water-filled capillary tubes. Spectra are correlated to data in Table 3.4. Experiment 5 was obtained with a 850μm OD capillary outside the wire loop and in an inhomogeneous field. Experiment 6 was obtained with a 850μm OD capillary outside the wire loop and in a shimmed field. Experiment 7 was obtained with a 1mm capillary inside the wire loop and in a shimmed field. Experiment 8 was obtained with a 3mm capillary outside the wire loop and in a homogeneous field. Experiment 9 was obtained with a 3mm capillary outside the wire loop and in a shimmed field.

Other than paramagnetic perturbations from the capacitors, etc. additional possible factors affecting linewidth are local impurity in the wire, alignment of the RF coil with the $\mathbf{B}_0$ field, and irregularities in the circular cross-section of the capillary walls. The prediction of homogeneity in the interior field of the capillary when it is placed in a uniform field (refer Chapter 2) assumed a perfect circular cross section without deviation along the length of the capillary tube. The 3mm capillary tubes were manufactured to high precision and tested as described in Chapter 2. As observed in Table 3.4, the 3mm tubes resulted in similar linewidth performance to the others used. A justification for using high precision 3mm tubes (approximate cost $25 each, as opposed to the 1mm capillary ~$1) cannot be found based on these results.

The probe shown in Fig. 3.2(c) was an attempt to reduce the overall size of this aligned wire probe design while retaining the narrow spectral linewidths found with the design of Fig. 3.2(b). The design was tested with 150μm and 1mm (OD) capillary tube sizes in homogeneous and shimmed fields. The resulting spectra are shown in Fig. 3.9.

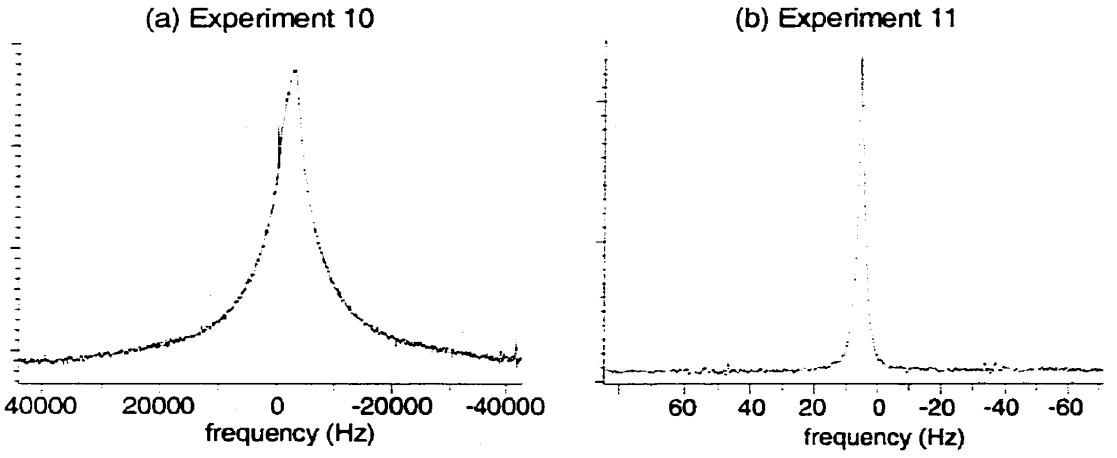

Fig. 3.9. NMR spectra resulting from RF coil design Fig. 3.2(c). Spectra are correlated to data in Table 3.4. Experiment 10 was obtained with a 150μm OD capillary inside the wire loop and in a homogeneous field. Experiment 11 was obtained with a 1mm OD capillary outside the wire loop and in a shimmed field.

The spectrum obtained when using the 150μm capillary gave a larger than expected linewidth, i.e. FWHM=7000Hz. The peak shape was roughly symmetric as can be seen in Fig. 3.9(a). The reason for the broad linewidth is not known, but certainly warrants further investigation to determine if fault lies with materials or methods, e.g. air bubbles remaining in the capillary after filling with water. The magnetic field inhomogeneity associated with an air bubble in the capillary tube could account for this observed result. The presence of bubbles in the narrow capillary was difficult to visually confirm due to an opaque coating on the outer capillary wall. When the probe was fitted with a 1mm capillary, the linewidth reduced to a more believable 8Hz at FWHM.

In a shimmed field, again using the 1mm capillary, the linewidth was reduced to 2.3Hz. This was a reasonable result but indicated the presence of local field inhomogeneity that could not be shimmed out with the room temperature shim set. Possible sources for this local inhomogeneity are the proximity to the tuning/matching capacitors, the cable connection to the probe, the solder used at component/cable joints, or a misalignment of the RF coil.

3.5 Chapter Summary

The primary conclusion from this chapter is that a probe design based on the magnetostatic properties of a long cylinder in a uniform magnetic field can achieve near ideal linewidths, in agreement with the theory. This conclusion is based on results obtained with capillary tube sample diameters of 1mm and 3mm. This long-cylinder magnetostatic property has been mentioned in passing in the physics literature, but has previously not been discussed in the context of NMR probe construction. The target linewidth of 1Hz has been achieved and surpassed with this design, although the large sample size does not allow 1Hz performance (FWHM) in an inhomogeneous field.

The principle was tested with three different probe implementations, and found to give reasonable results in all cases. In the initial proof-of-concept-implementation, Fig. 3.2(a), the probe achieved a minimum linewidth of 5.5 Hz FWHM (14ppb) with an associated SNR of 2000. The long wire implementation, Fig. 3.2(b), came the closest to a "perturbation free" volume near the NMR sample. The minimum linewidth achieved with this design was 0.60 Hz FWHM (1.5ppb) although the SNR was only 20. This design would be ideally suited to a test platform designed to quantify the magnetostatic-related inhomogeneity of the field. The final design Fig. 3.2(c) was an attempt at miniaturization of the long wire design. However, the attempt was too aggressive and the minimum linewidth achieved was only 2.3Hz FWHM (5.75ppb) with an associated SNR of 60.

These results also validate the use of ordinary materials, such as copper, for construction of the RF coil. This material is relatively easy to work with in respect to shaping and soldering. The capillary tube can be positioned easily inside or outside the RF loop allowing considerable freedom in the probe's construction.

Further effort is needed to determine the minimum dimensions of the probe while preserving the integrity of the B_0 field near the sample. Small size is critical to the successful operation of this probe in inhomogeneous fields, as smaller sample volumes, e.g. capillary tubes, can thus be used and narrow lines obtained. The field measurement is then correspondingly more precise.

Chapter 4

PROBE DESIGN 2. SUSCEPTIBILITY-COMPENSATED WIRE AND THE "HAIRPIN" LOOP

4.1 Introduction

Conventional NMR-based microprobes are usually built by winding a small solenoidal RF element around a small spherical or cylindrical sample. The wire used to build the solenoid induces significant adjacent magnetic field gradients when it is placed in a strong magnetic field. These degrade both the NMR linewidth and spectral signal-to-noise performance of the probe.

A direct solution to this problem, without any compromise of signal-to-noise ratio or NMR linewidth, is to use zero-susceptibility wire in the construction of the RF element (Anderson and Shoolery 1963; Hoult 1978). The wire is effectively "magnetically invisible" and therefore does not introduce any local field inhomogeneity. Optimal linewidths are thereby achieved and full signal-to-noise is available as the wire can be close to the NMR sample. Thus, we describe in this chapter the production of wire with zero volumetric magnetic susceptibility for use in the construction of high-resolution NMR probes.

There are two main types of zero-susceptibility wire. The first is made by forming an alloy from suitable diamagnetic/paramagnetic metals, e.g. copper with palladium (Vogt 1933). The alloy may then be drawn to the required wire gauge. This method has the advantage that the wire has zero susceptibility for all orientations in a magnetic field. Its disadvantage is that

its conductivity is reduced from that of the better electrical conductor of the alloy pair, thus reducing the Q-factor of any coil and hence, the signal-to-noise ratio. Possibly, there exists a commercial supply of alloyed wire possessing zero susceptibility, but unrecognized as such by the supplier. However, even if one could chance on finding such a product, there are still the issues of conductivity and batch-to-batch variation of susceptibility due to trace ferrous contaminants.

Turning to the second type, it is well known that radio-frequency current flows in a thin skin on the surface of a conductor. Thus, forming a simple co-axial combination of diamagnetic and paramagnetic metals, as shown in Fig. 4. 1 need not degrade conductivity; for example, we might use copper outside an aluminium wire core. Because of the potential signal-to-noise ratio advantage, we have chosen to pursue the simple co-axial combination method here. We also describe in this chapter a specially built probe used to evaluate/verify the susceptibility of the wire produced. In this probe design, the wire used to make the RF element is oriented perpendicular to the strong $\mathbf{B}_0$ field of the magnet as shown in Fig. 4.2, and has the form of a "hairpin loop" microprobe. This probe is not intended for use as a practical magnetic field microprobe. A working microprobe based on a solenoidal RF element wound with zero-susceptibility wire is described in Chapter 5.

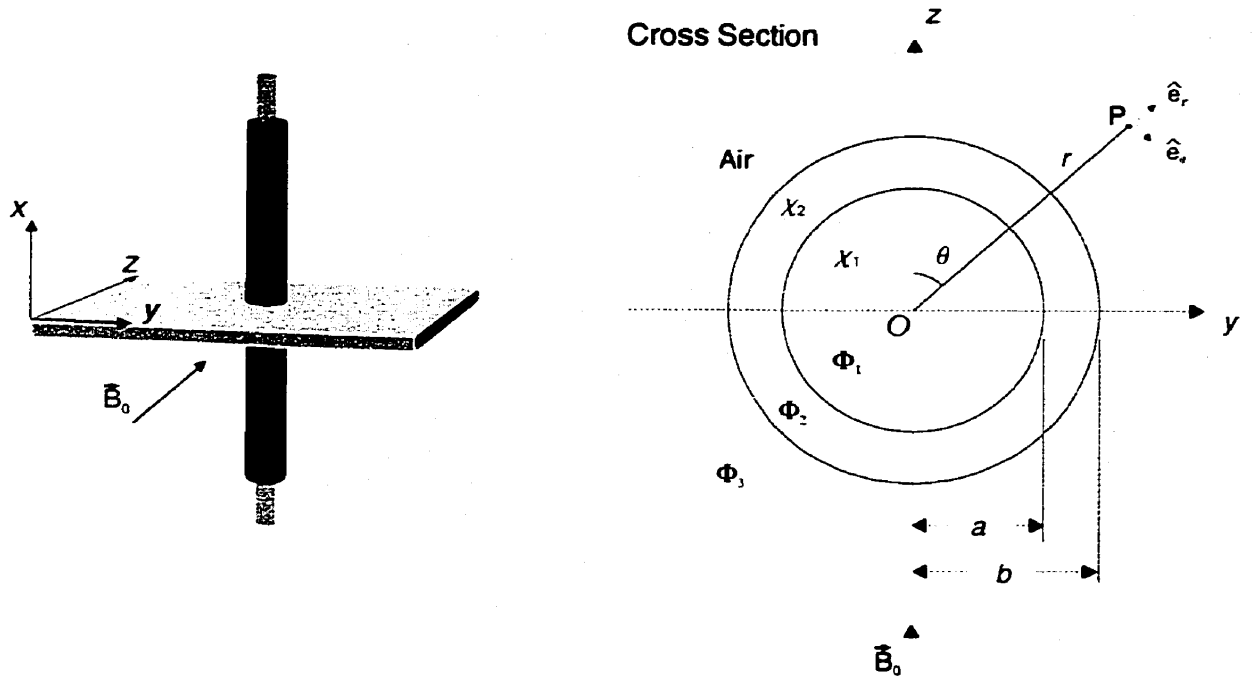

Fig. 4. 1. Cross-section of a co-axial long wire with an inner core of radius a and associated volume magnetic susceptibility χ_1, and an outer layer with inner and outer radii a and b respectively and associated susceptibility χ_2, oriented perpendicular to a uniform magnetic field $\mathbf{B}_0$ in the circular-cylindrical co-ordinate system (r, θ). Φ is the magnetic scalar potential.

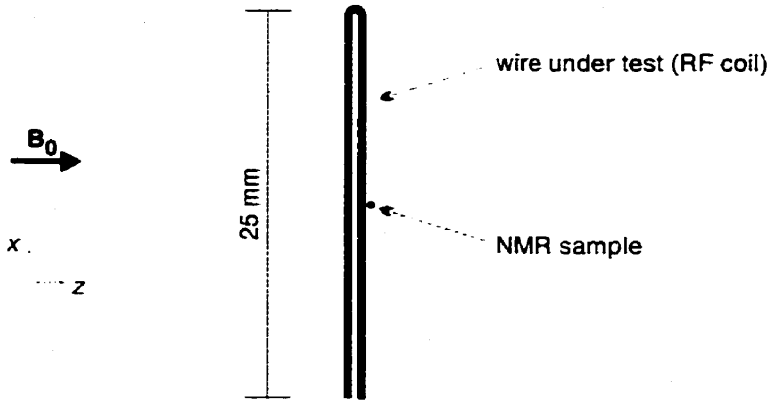

Fig. 4.2. Hairpin loop RF coil. The susceptibility of the wire can be studied by forming the wire into a hair-pin loop shape and then placing the NMR sample near the legs of the loop as shown in the figure.

4.2 Theory

4.2.1 Magnetostatic Analysis

The static magnetic character of wire constructed in a simple co-axial combination depends on the susceptibility of the materials involved, the dimensions of construction, and the geometric relationship of the wire to the magnetic field. For a long straight wire in a uniform magnetic field where the wire is oriented perpendicular to the field, the results are analogous to the case of the water-filled capillary presented in Chapter 2. From Eq. (2.22) then, the equation describing the static magnetic field outside the wire is given by:

$$\mathbf{B}_{r\geq b}(r,\theta) \equiv \mathbf{B}_0 + \frac{B_0 a^2}{2r^2}\left[\chi_1 + \chi_2\left(\frac{b^2}{a^2}-1\right)\right]\left[\cos\theta\,\hat{\mathrm{e}}_r + \sin\theta\,\hat{\mathrm{e}}_\theta\right],\ \chi \ll 1 \qquad (4.1)$$

It is convenient to define an effective susceptibility $\chi_{1\text{-}2}$ for the combination of susceptibilities χ_1 and χ_2 that appear in Eq. (4.1):

$$\mathbf{B}_{r\geq b}(r,\theta) \equiv \mathbf{B}_0 + \frac{B_0 b^2}{2r^2}\chi_{effec}\left[\cos\theta\,\hat{\mathrm{e}}_r + \sin\theta\,\hat{\mathrm{e}}_\theta\right],\ \text{where } \chi_{effec} = \frac{a^2}{b^2}\left[\chi_1 - \chi_2\left(1-\frac{b^2}{a^2}\right)\right] \qquad (4.2)$$

A plot of effective susceptibility versus the wire diameter is given in Fig. 4.3 for the combination of aluminium core and copper outer layer. The curve in this plot crosses the axis at the point where the effective susceptibility of the wire is zero. The zero crossing dimensions are found by setting the effective susceptibility to zero in the above equation. Thus

$$\chi_{effec} = \frac{a^2}{b^2}\left[\chi_1 - \chi_2\left(1-\frac{b^2}{a^2}\right)\right] = 0, \qquad \Rightarrow\ b = a\sqrt{\frac{\chi_2 - \chi_1}{\chi_2}}. \qquad (4.3)$$

This result was also found by F. O. Zelaya, et. al. (Zelaya, Crozier et al. 1995).

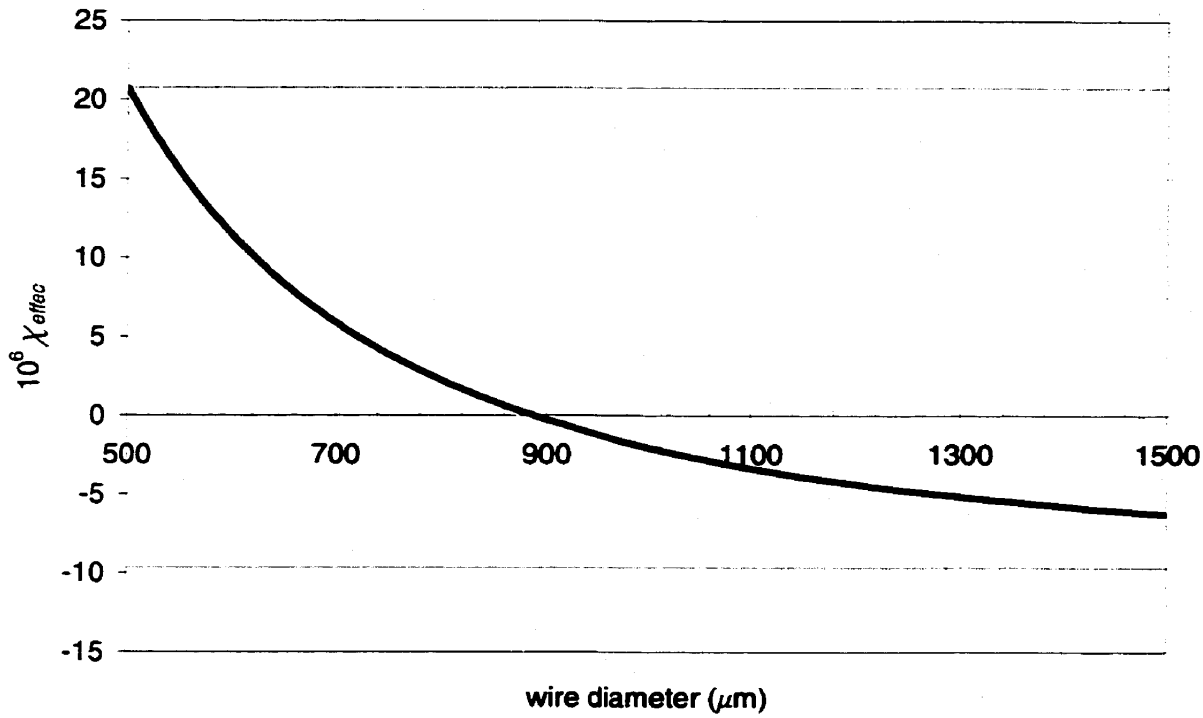

Fig. 4.3. Effective susceptibility of a coaxial wire for the geometry of Fig. 4.2 with a core of aluminium and a copper outer layer. The effective volumetric magnetic susceptibility is seen to decrease as the copper outer layer becomes thicker for a field point outside the wire. In the example given here the aluminium core has a diameter of 500μm. The thickness corresponding to zero susceptibility wire is 888μm. The solid red lines indicate the susceptibility of aluminium ($\chi_{Al} = 20.76 \pm 0.01 \times 10^{-6}$) and copper ($\chi_{Cu} = -9.63 \pm 0.01 \times 10^{-6}$).

In practice, there are two methods for forming co-axial wire: extrusion or electroplating. The major advantage of extrusion is the avoidance of the formation of a binary alloy at the interface between the metals. Binary alloy phases are sometimes brittle and do not allow the wire to endure the bending and shaping needing to form the RF coil. A disadvantage associated with extrusion is that the core may drift off the central axis. Then the susceptibility cancellation would vary along the length of the finished wire. Non-ferrous dies (and possibly cutting tools) may also be required. A variant on extrusion is to obtain precision tubing, e.g.

copper tubing, and insert a core of the opposite susceptibility (Doty 1999), e.g. aluminium rod or wire, doped plastic, etc. However, the suitability of this method is dependent on the availability of precision tubing and the elemental purity of both components. Electroplating, the method presented in this paper, is an acceptable solution for the production of wire in small quantities where the electrochemistry involved does not present a significant obstacle.

4.2.2 Dimensional Tolerance

The susceptibility cancellation predicted by Eq. (4.3) is valid only for accurate dimensions a and b. The expected value of dimension b depends on the precision of the input values for a, χ_1 and χ_2. The overall uncertainty in the predicted value of b is found using the propagation of errors in Eq. (4.5) (Bevington 1969).

$$\delta b^2 = \delta a^2 \left(\frac{\partial b}{\partial a}\right)^2 + \delta \chi_1^2 \left(\frac{\partial b}{\partial \chi_1}\right)^2 + \delta \chi_2^2 \left(\frac{\partial b}{\partial \chi_2}\right)^2 . \tag{4.5}$$

Using Eq.'s (4.3c) and (4.5), we then have

$$\delta b^2 = \delta a^2 \left(\frac{b}{a}\right)^2 + \delta \chi_1^2 \left(\frac{b}{2(\chi_2 - \chi_1)}\right)^2 + \delta \chi_2^2 \left(\frac{b\chi_1}{2(\chi_2 - \chi_1)}\right)^2 \tag{4.6}$$

For example, aluminium wire with a starting diameter of 0.5mm plated with copper reaches zero susceptibility at a diameter $b \pm \delta b = 888 \pm 2\,\mu\text{m}$ with $\chi_{Cu} = -9.63(1) \times 10^{-6}$, $\chi_{Al} = +20.76(1) \times 10^{-6}$ (SI units (Weast 1987)), and $\delta a = 1\,\mu\text{m}$, a precision achievable with a high quality micrometer. To compound the problem when electroplating, a measure of b may have inaccuracy of much more than 1μm if the plated surface is rough.

Given then that there will inevitably be errors in b, we need some measure of how accurate b should be for *acceptable* susceptibility cancellation. From a practical point of view, a

comparison, say, of our plated wire and another wire made of pure copper of the same diameter, is helpful. To do this we form a ratio of field inhomogeneity using the inhomogeneity term in Eq. (4.1), putting the composite wire (with parameters a, b, χ_1, χ_2) in the numerator and the copper wire (with parameters b and χ_3) in the denominator. The ratio R so formed reduces to

$$R = \frac{a^2}{b^2}\left(\frac{\chi_1 - \chi_2}{\chi_3}\right) + \frac{\chi_2}{\chi_3}. \tag{4.7}$$

with associated uncertainty

$$\begin{aligned}\delta R^2 = &\left[\frac{2a}{b^2}\left(\frac{\chi_1 - \chi_2}{\chi_3}\right)\right]^2 \delta a^2 + \left[\frac{2a}{b^3}\left(\frac{\chi_1 - \chi_2}{\chi_3}\right)\right]^2 \delta b^2 + \left[\frac{a^2}{b^2 \chi_3}\right]^2 \delta \chi_1^2 \\ &+ \left[\frac{1}{\chi_3}\left(1 - \frac{a^2}{b^2}\right)\right]^2 \delta \chi_2^2 + \left[\frac{R}{\chi_3}\right]^2 \delta \chi_3^2\end{aligned} \tag{4.8}$$

The uncertainty δR is important here as a check of the usable precision we may set for the ratio R. Using our previous aluminium/copper example, we find that $\delta R = 0.1\%$ for an idealized $\delta b = \delta a = 0$, and a=500μm, b=888μm, $\delta\chi_{Al} = \delta\chi_{Cu} = 1\times10^{-8}$, while the limits of b that will give $R \leq 1\%$ are $b = 888 \pm 4$μm.

The wire thickness for a practical microcoil design is often much smaller than our example just presented here. Additionally, the limits on the final plated diameter for a precision zero susceptibility result become harder to achieve as the finished diameter of the wire becomes smaller. Consider a final diameter of the plated wire in the 80 μm range. Copper plated on an aluminium wire of starting diameter 50 μm will have a finished diameter b of 88.8 ± 0.4 μm, $R \leq 1\%$. For other metal combinations, say rhodium ($\chi_{Rh} = 168 \pm 1 \times 10^{-6}$ (Weast

1987)) plated onto a copper wire of starting diameter 80 μm, we will have a finished diameter 82.26 ± 0.02 μm, $R \leq 1\%$, ($\delta R = 0.6\%$ for an idealized $\delta b = \delta a = 0$, and $a = 80\mu m$, $b = 82.26\mu m$, $\delta\chi_{Cu} = 1\times10^{-8}$, $\delta\chi_{Rh} = 1\times10^{-6}$). If we reverse the order of plating and plate copper onto a thin rhodium wire of starting diameter 20μm, we reach a zero susceptibility result at 85.9±0.4μm, $R \leq 1\%$.

These examples illustrate an important compromise in choosing metals for a zero susceptibility combination. Thin layers are easier to plate and will likely have excellent mechanical properties, but as the error in the Rh/Cu example indicates, thin layers must be applied with a mirror finish on a surface that is equally smooth with wire diameter well known. Furthermore, as rhodium has only one third the electrical conductivity of copper, and since current at radio frequency travels on the outer skin of the wire, the overall Q-factor of a coil made with this wire would be reduced unless the thickness of Rh were much less than the skin depth. Plating copper onto rhodium, or copper onto aluminium, gives the best Q and a more realistic chance of obtaining a final diameter of the required precision. The difficulty here, however, is that thick coatings often lead to poor mechanical properties (especially ductility) of the finished wire.

4.2.3 Diffusion

The expected susceptibility cancellation that occurs with plated wires may degrade due to diffusion of metal atoms across the interface that separates them. The functional dependence of susceptibility with the proportions of two metals can be highly non-linear, as seen from examples in Ref. (Vogt 1933). While diffusion at room temperature is not expected to be a problem, diffusion rates are strongly dependent on temperature, and the complete

"temperature history" of the plated wire must be considered. In this regard, whether or not annealing is required is important. The mechanism of diffusion is either migration through interstitial sites or thermally activated jumps into vacant lattice sites (LeClaire 1983). The exact mechanism depends on the crystal structure of the two metals involved. The net flux of atoms $\mathbf{J}_N$ of one metal species diffusing into another is related to the concentration gradient N and the diffusion coefficient D through Fick's Law, $\mathbf{J}_N = -D\,\nabla N$. An equivalent diffusion equation exists expressing an equal and opposite flux $-\mathbf{J}_N$ for the second species diffusing into the first. For simplicity this second process is ignored here.

Since the diffusion process is evolving in time, we can write a continuity equation that expresses the point wise conservation of matter, $\frac{\partial N}{\partial t} = -\nabla \cdot \mathbf{J}_N$. This expression is known as Fick's Second Law. For diffusion across a cylindrical surface, as in the case of our co-axial wire, we can consider a depth of penetration that is small compared with the radius of curvature of these surfaces. Then, the diffusion system can be considered one-dimensional and Fick's first and second laws become $J_N = -D\frac{\partial N}{\partial x}$ and $\frac{\partial N}{\partial t} = \frac{\partial}{\partial x}\left(D\frac{\partial N}{\partial x}\right)$. Generally, D depends on concentration, on position coordinate, or both. If D does not depend on position then we can write

$$\frac{\partial N}{\partial t} = D\frac{\partial^2 N}{\partial x^2} \quad . \tag{4.9}$$

If we further assume that D does not depend on concentration we can proceed with an approximate solution, known as the Error Function Solution (Shewmon 1963). Let $x = 0$ be

located at the boundary of the two undiffused metals at time $t = 0$ (see Fig. 4.4). Then the concentration of one metal species diffusing into another at some later time t is given by

$$N(x,t) = \frac{N'}{2}\left[1 + \mathrm{erf}\left(\frac{x}{2\sqrt{Dt}}\right)\right], \tag{4.10}$$

where N', a normalization constant, is simply equal to 1 in our case, and "erf( )" is the error function defined by the equation

$$\mathrm{erf}(\chi) = \frac{2}{\sqrt{\pi}}\int_0^{\chi} \exp\left(-\eta^2\right) d\eta. \tag{4.11}$$

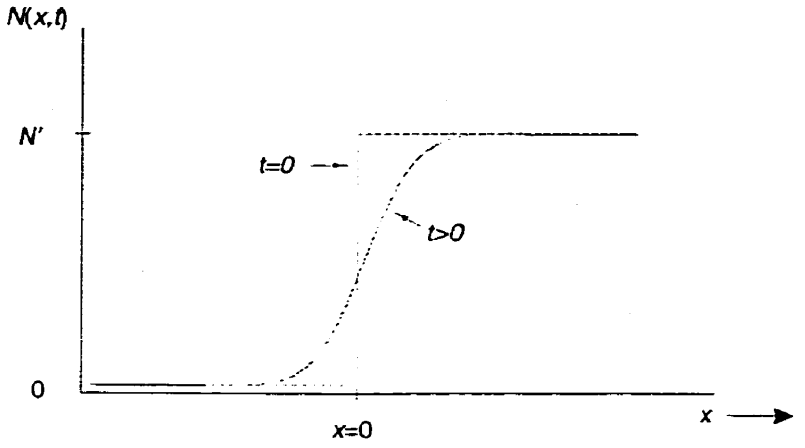

Fig. 4.4. The curve $N(x,t)$ represents the diffusion of one of the metals pairs before diffusion begins, i.e. $t = 0$, and then a later time $t > 0$.

The diffusion constant D in Eq. (4.10) cannot be obtained directly from the literature, but may be determined from the Arrhenius equation, Eq. (4.12) (LeClaire 1983), which also includes the observed temperature dependence of the diffusion process.

$$D = D_0 \exp\left(-E/k_B T\right). \tag{4.12}$$

In this expression, D_0 is the frequency factor for solute impurity diffusion in the solvent, E is activation energy for the process, k_B is Boltzmann's constant, and T is temperature at the

boundary. Examples are given in Table 4.1 for diffusion between candidate metal-pairs that might be used for making zero susceptibility wire.

Table 4.1. Diffusion-time calculations for diffusion in copper, aluminium, and zinc using the error function solution $N(x,t)$ given in Eq.(4.10). Two scenarios are considered here. The first is diffusion at room temperature to the depth of a few atomic layers, i.e. 1nm, to a concentration $N = 0.9N'$. The second is diffusion at 500C (e.g. during annealing) to a depth of 1μm, $N = 0.9N'$. Data for the Frequency Factor and Activation Energy have been taken from reference (Burachynsky and Cahoon 1997).

Solute	Solvent	Frequency Factor D_0 (10^{-4}m^2/s)	Activation Energy E (kJ/mole)	Time to diffuse to a depth of 1nm* at $T = 20$C *($N = 0.9N'$)	Time to diffuse to a depth of 1μm* at $T = 500$C *($N = 0.9N'$)
Rh	Cu	3.3	242.8	10^{28} years	250 days
Pt	Cu	0.56	233	10^{27} years	350 days
Cu	Al	0.65	136.1	285 years	8 seconds
Zn	Al	0.756	127.4	6.3 years	2 seconds
Cu	Zn	1.11	124.25	460 days	0.7 seconds

Since diffusion is dependent on temperature, the sample calculations in Table 4.1 have been given at room temperature as well at 500C, such as might be encountered during an annealing process. The wire may need to be annealed after plating to improve its mechanical or electrical properties, e.g. to control acoustic ringing of the RF coil (Fukushima and Roeder 1979; Gerothanassis 1987). The origins of acoustic ringing are mechanical/electromagnetic oscillation at the B_1 field frequency in the presence of the strong B_0 field. If an annealing step is necessary, the examples from Table 4.1 suggest that one should avoid constructing zero susceptibility wire from metals that easily diffuse into each other where one is used as a

relatively thin coating and there is a non-linear dependence of susceptibility with respect to metal alloy composition.

4.2.4 Temperature Dependence

Change of temperature may lead to changes in the final magnetic field $\mathbf{B}_{final}$ through one, or both, of χ_1, χ_2 in Eq. (4.3). Using the rules for propagation of error (Bevington 1969), we may obtain

$$\delta B^2 = (\delta\chi_1[T])^2\left(\frac{\partial B}{\partial \chi_1}\right)^2 + (\delta\chi_2[T])^2\left(\frac{\partial B}{\partial \chi_2}\right)^2 = \delta T^2\left[\left(\frac{d\chi_1}{dT}\right)^2\left(\frac{\partial B}{\partial \chi_1}\right)^2 + \left(\frac{d\chi_1}{dT}\right)^2\left(\frac{\partial B}{\partial \chi_2}\right)^2\right].$$

Differentiating using Eq. (4.1) we then have,

$$\delta B^2 = \delta T^2\left[\left(\frac{d\chi_1}{dT}\right)^2\left(\frac{B_0 a^2}{2r^2}\right)^2 + \left(\frac{d\chi_2}{dT}\right)^2\left(\frac{B_0}{2r^2}\left(b^2 - a^2\right)\right)^2\right]. \tag{4.13}$$

The anticipated range of temperature depends on the type of experiment performed, but we can evaluate Eq. (4.13) for a simple instance where the temperature of the wire may change by only a few degrees. If we use the somewhat arbitrary condition that the fractional change of magnetic field should be limited to no more than 1 part in 10^8 at a field point chosen to be at the surface of the wire, and the assumption that $|\chi_1| \approx |\chi_2|$, then the temperature coefficient $\frac{d\chi}{dT}$ must be on the order of 10^{-8}-K^{-1}. Table 4.2 provides a list of temperature coefficients for possible probe metals. From Table 4.2 we can see that use of metals from the platinum family should be avoided if strong temperature changes are expected during the NMR experiment. In this regard, copper and aluminium are suitable materials.

Table 4.2. Approximate Temperature Coefficients of Volumetric Magnetic Susceptibility (in SI units) (Henry and Rogers 1956; Hurd 1966; Flynn, Rigney et al. 1967; Kittel 1971)

Element	χ	$\frac{\partial \chi}{\partial T}$
Paramagnetic Metals		
Pt	278.3×10^{-6}	$20\times10^{-8}\ K^{-1}$
Rh	168×10^{-6}	$8\times10^{-8}\ K^{-1}$
Al	20.76×10^{-6}	$0.03\times10^{-8}\ K^{-1}$
Diamagnetic Metals		
Cu	-9.63×10^{-6}	$-0.2\times10^{-8}\ K^{-1}$
Ag	-23.9×10^{-6}	$-0.2\times10^{-8}\ K^{-1}$
Au	-34×10^{-6}	$-0.03\times10^{-8}\ K^{-1}$

4.2.5 Design summary

Susceptibility. A high susceptibility metal plated on a low susceptibility metal implies that a precision-dimension/smooth-surface finish must be attained. If two metals of roughly equivalent but opposite susceptibilities are used, then the final dimension and finish are not as critical.

Conductivity. To obtain the highest Q factor, the better conductor of the pair should be plated to a thickness of at least five skin depths.

Electroplated Thickness. If electroplating is used, then thin layers are more successfully plated than thick layers. Thin/thick is relative. Generally, anything more than 10μm is considered thick.

Diffusion. Thin coatings may lead to susceptibility degradation if the base and coated metals diffuse easily at elevated temperatures, e.g. during annealing. The susceptibility of the binary alloy in the diffusion region may be highly non-linear with the degree of diffusion.

Acoustic Ringing. The choice of metals should minimize the possibility of acoustic ringing of the RF coil. Unfortunately, aluminium, an attractive metal in other respects, is one of the poorest materials because of this parasitic effect. If the wire is annealed to control this effect then consideration must be given to ensuring that the susceptibility cancellation is not adversely affected due to diffusion.

Temperature coefficient of susceptibility. If temperature changes are expected during the NMR experiment, then consideration of this coefficient is warranted. Metals from the platinum group show strong temperature dependence.

Availability. Finally, the metal used as the wire core should be relatively easy to obtain with exact dimensions and in either high purity, or otherwise known not to contain any ferrous contaminants. This is important for the reproducibility of zero susceptibility results

4.3 Manufacture of the wire

From the design considerations mentioned in the previous section, we pursued a zero susceptibility combination with aluminium as the core metal and copper on the exterior. Using an electroplating technique, there is more than one way to achieve this combination. Copper clad aluminium wire (12% Cu by volume) is available commercially and is easily built up to the desired copper thickness in a simple copper sulphate-acid electroplating bath. However, the desired starting diameter of wire may be limited, based on the commercial source. In addition, the chemical purity of the wire is usually unknown, and unfortunately, iron is a common contaminant. Thus, we have investigated the plating of copper on pure aluminium (99.999%).

The objective of the electroplating procedure is to produce a smooth and ductile copper coating, free from ferrous contaminants. Ductility is especially important since we have chosen to plate copper onto a straight length of wire, and then bend the wire into a coil. (The other method of pre-forming a coil and then electroplating is not preferred because of the difficulties of ensuring even plating and of accurate measurement.) Ductility may be compromised in two regions. One is at the boundary layer between the core metal and the plated metal. In this region, an intermetalic alloy will be formed which may, or may not be ductile. As an aid to predicting which combinations of metals are suitable, phase diagrams of intermetalic binary alloys are available (Lyman 1973). The second region is the (usually thick) layer of plated copper. The nature of the bath (e.g. copper cyanide, copper sulphate, or copper pyrophosphate), and any additives used as well as the operation of the bath (e.g. temperature, current density, cathode potential), all affect the properties of this layer.

The final apparatus used consisted of an electro*less* plating setup, and an electroplating setup as shown in Fig. 4.5. Electroless plating, sometimes called immersion plating, is

successful to varying degrees for various metal pairs. The immersion plating apparatus consisted simply of four beakers large enough to accommodate the wire to be plated without bending. The immersion plating solutions will be described in the following section. The apparatus for electroplating is shown in Fig. 4.6. The electroplating process described here used two different solutions, one based on copper cyanide, and the other on copper sulphate. Copper cyanide and copper sulphate solutions are kept in separate beakers and then can be substituted in place, as shown in Fig. 4.6, at the appropriate time. In this way, only one stirrer and anode are needed. If equipment permits, two stirrers and two anodes for each of the copper cyanide and the copper sulphate solutions can be used as shown in

Fig. 4.7. Only a single cathode stirring motor is required in any case, and any small, geared motor will suffice to rotate the wire (cathode) during plating The angular speed used was on the order of 1 ± ½ revolutions per second. The anode used was a high purity copper rod (7mm x 150mm, 99.999%, Supplier: Alfa Aesar, Ward Hill, MA). The use of a phosphorized copper anode (Supplier: Kocour, Chicago, IL) is also described later (in the context of a more advanced plating technique). The constant electroplating current circuit is shown in Fig. 4.8. The circuit can be used to supply low current, 1μA to 10mA, and currents greater than 10mA in either the forward only, or forward/reverse directions. The main current supply is a standard constant current/voltage supply (Hewlett-Packard 6002). The low current portion of the circuit uses a National Semiconductor LM 334 3-Terminal Adjustable Current Source. A single external potentiometer is used to regulate the current from 1μA to 10mA. Current reversing (to be described later) is achieved using an Analog Devices DG212 analogue switch that is suitable for currents up to 30mA. An external square wave generator with an adjustable duty cycle was used to set the timing for forward and reverse current modes.

An important note with respect to hardware needs to be made at this point. If clips or other mounting hardware are used near the beaker, ensure that they are not plated with nickel. This is a common finish, and will certainly corrode or dissolve either in the fumes given off by the acid-based solution, or in the event of direct contact with the solution. Indeed, any hardware that has the chance of coming in contact with the plating bath should be non-magnetic.

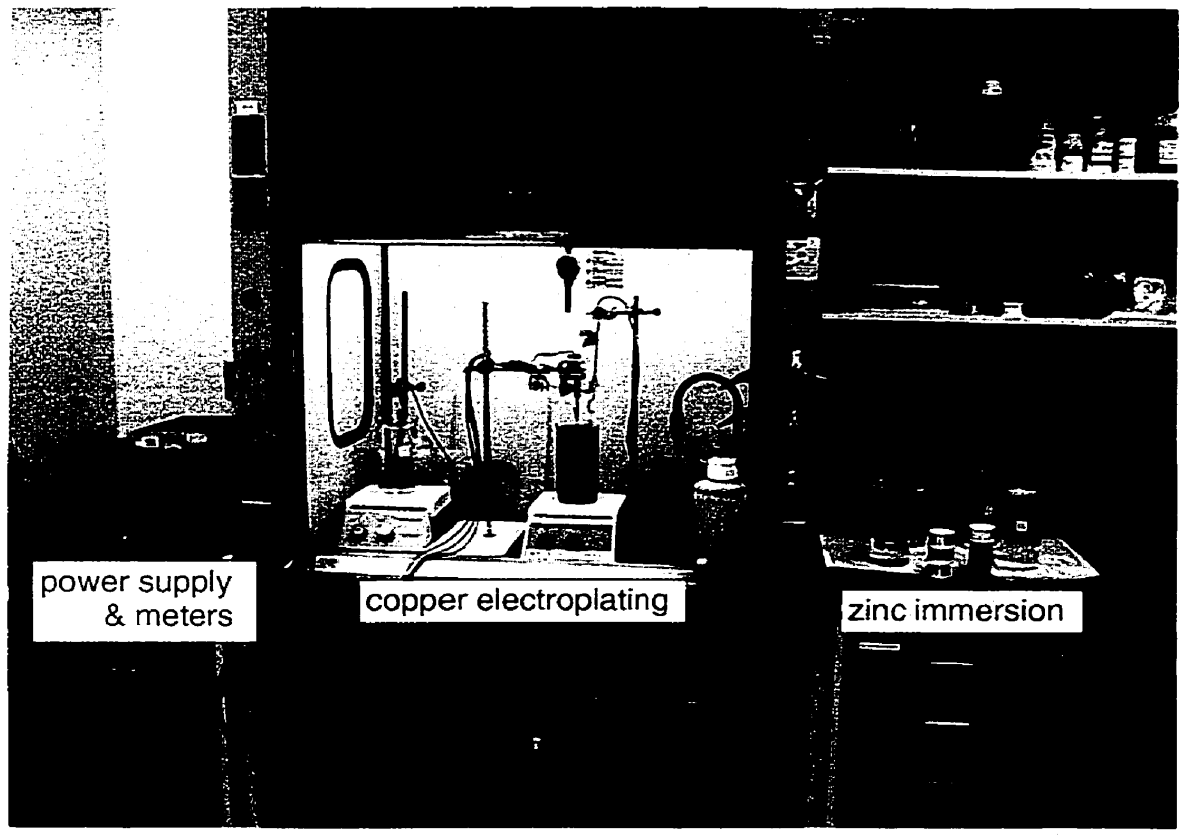

Fig. 4.5. Photograph of the apparatus for the electroplating experiments. The fume hood is a necessary precaution in case hydrogen cyanide gas is generated by accidental mixing of the acid-based plating solution and the cyanide-based plating solution.

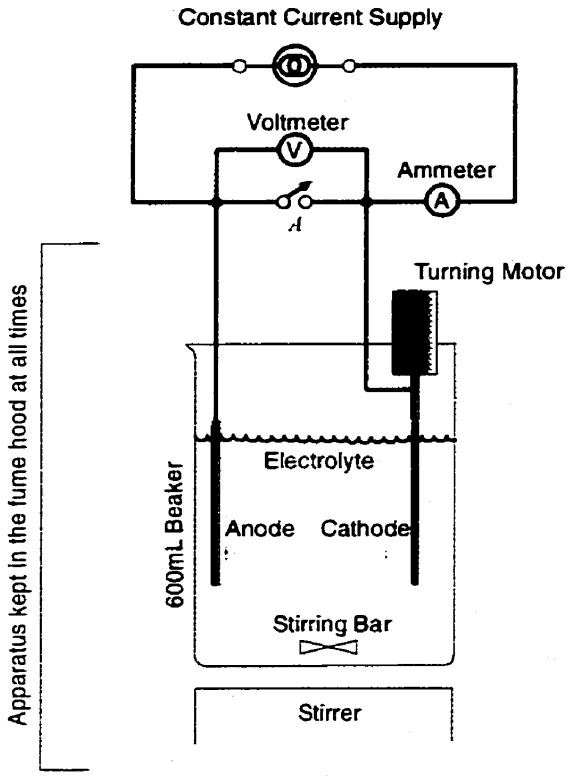

Fig. 4.6. Electroplating apparatus used in this work showing the arrangement of the plating bath and accessories for stirring the solution and rotating the wire. The turning motor and anode are mounted on a retort stand (see next figure) so that separate electrolyte-filled beakers can be used for acid and cyanide-based steps.

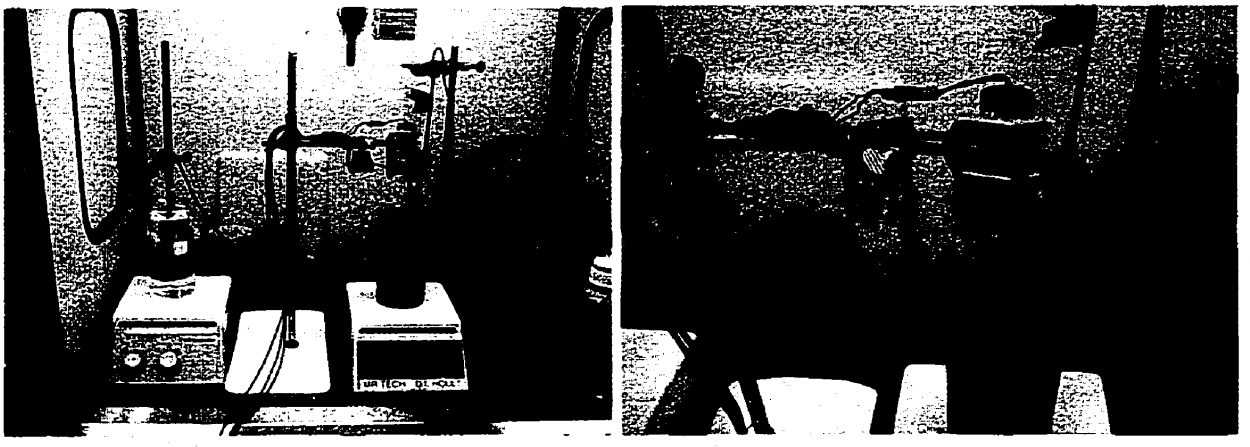

Fig. 4.7. A photograph of the arrangement for plating in separate cyanide and acid-based bath stations. In initial experiments, only one station was used due to a shortage of stirring plates. This obvious safety hazard (HCN) is reduced by having separate stations. The base plates are used for stirring the beaker contents as well as heating if needed. (Right) Close-up of the stirring motor and anode/cathode arrangement. The cathode is completely enclosed in a polypropylene bag to prevent the layer of dark deposit from being eroded from the anode. The cathode is electrically isolated from the stirring motor power supply. Electrical contact is made with a graphite "brush" pushing on a brass rotor. The wire and alligator clip seen wrapped around the rotor are attached only at one point on the brush and serve to increase the contact pressure between the brush and rotor.

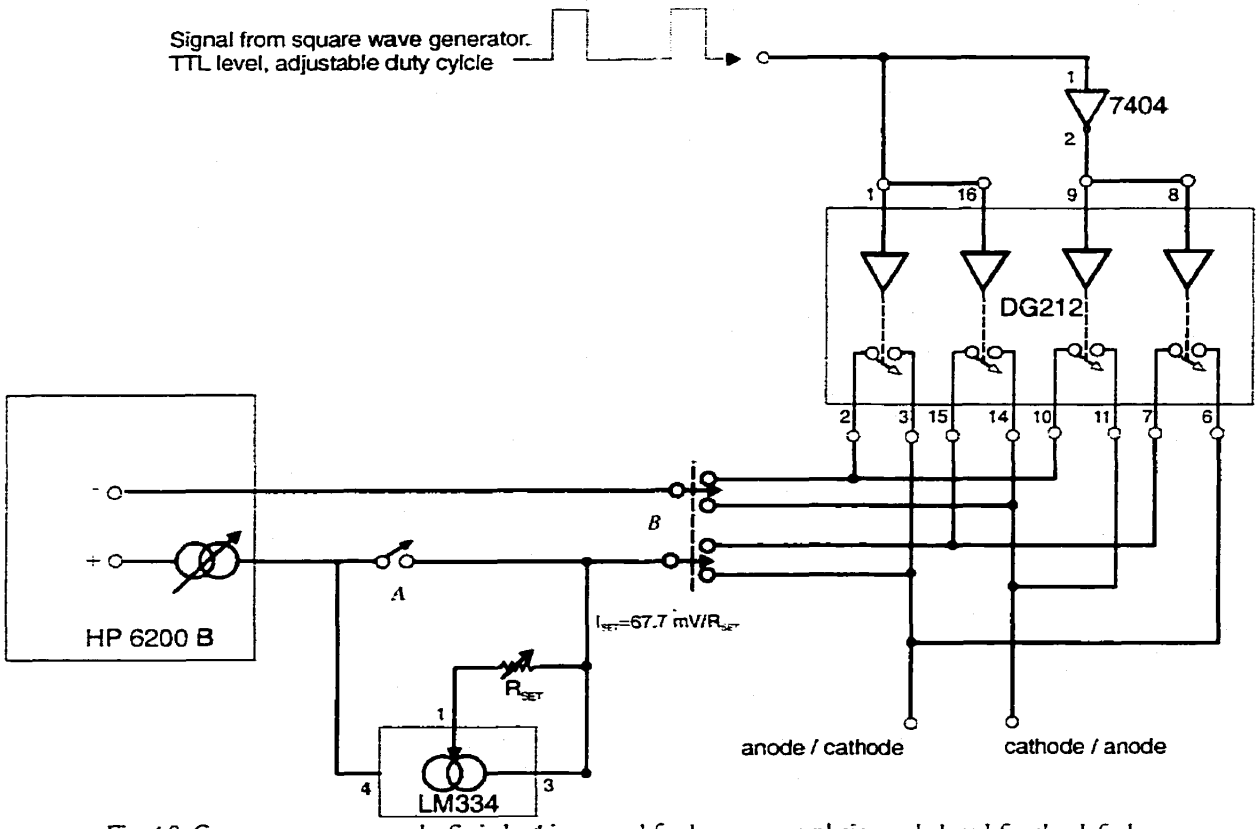

Fig. 4.8. Constant current supply. Switch *A* is opened for low current plating and closed for the default current set by the (Hewlett-Packard 6002) power supply. If current is periodically reversed then switches at *B* engage the current switching circuit based on the DG212 chip. Switches on the DG212 are shown for a logic "0" input. A square wave generator with an adjustable duty cycle controls the forward/reverse current plating times.

The plating procedure that follows has been obtained by trial and error with a great deal of introspection between trials. The difficulty in obtaining a simple protocol is the unusual requirements of: the absence of ferrous materials in the process, the high purity of the aluminium, the thickness of the copper to be plated, and the small starting diameter of the wire, as is appropriate for NMR microcoils. No solutions exist in industry for this unique combination. The procedure was initially developed for plating copper on aluminium wire with a starting diameter of 0.5 mm (required copper thickness for zero susceptibility: 194μm). The method has since been successful on initial aluminium wire diameters as small as 50 μm.

4.3.1 Step 1. The Need for Zinc Immersion

Initially, plating of copper directly onto aluminium was attempted, but was unsuccessful. The copper did not cover the aluminium evenly, but was deposited in small patches as shown in Fig. 4.9. The problem is the layer of aluminium oxide that inhibits a bond with another metal. The oxide layer may be stripped off in a strongly basic solution such as a 4M solution of sodium hydroxide. It is difficult, however, to transfer the wire out of the hydroxide solution, and then rinse it in water without reforming the oxide layer. If the wire can perchance be kept free of oxide (e.g. with a layer of NaCl solution), placing it in a standard copper sulphate-acid plating bath yields a brittle deposit due to an energetic immersion reaction (i.e. no external current employed) that rapidly heats the wire. No trace of this reaction has been found in the literature. The immersion reaction ends as soon as the surface of the aluminium has a complete thin covering of copper. A table of electrode potentials E_0 (sometimes called an *emf series*) can be used to determine when a metal will undergo an immersion reaction. In general, an oxidizing agent will oxidize a reducing agent that is more positive in the emf series. The kinetics of the process, e.g. speed, is not predicted by this generalization. In our case, aluminium (E_0 = –1.7 V) is the oxidizing agent and copper (E_0 =+0.34V) is the reducing agent (Boikess and Edelson 1981; Parthasaradhy 1989). It is a subtle but important fact that the electrode potential of any metal in solution depends on the specific nature of the bath, e.g. acid or alkaline, and the concentration of the dissolved species. Immersion reaction deposits typically adhere poorly, and copper plated upon such a base usually breaks during the coil winding process. Ductility is further affected since copper and aluminium do not form a ductile inter-metallic alloy at their interface (Lyman 1973). This

precludes using other techniques, such as physical or chemical vapour deposition, to coat the aluminium wire with copper and then further build up the required layer in a heavy electroplating solution.

Fig. 4.9. First results of electroplating copper from a copper sulphate (acid) bath directly onto aluminium. The copper plates onto the aluminium in nodules that form a column-like deposit when observed under high magnification. The copper seems to build up on the aluminium surface in places where the electroplating current has "punched through" the oxide layer.

To avoid these problems, we apply a thin coating of zinc by submerging the aluminium wire in a zinc immersion bath for 5 minutes (also known as zinc pickling), see Fig. 4.10. The aluminium wire should be cleaned beforehand, e.g. wiping the wire with a lint free cloth and good solvent such as acetone, in order to remove any traces of organic material that may remain from the manufacturing process. Zinc plated on aluminium in this way adheres well and the process is one of only a few successful immersion deposit reactions. Furthermore, zinc and aluminium form a ductile inter-metallic alloy at their interface (Lyman 1973) and the zinc prevents reformation of an oxide layer.

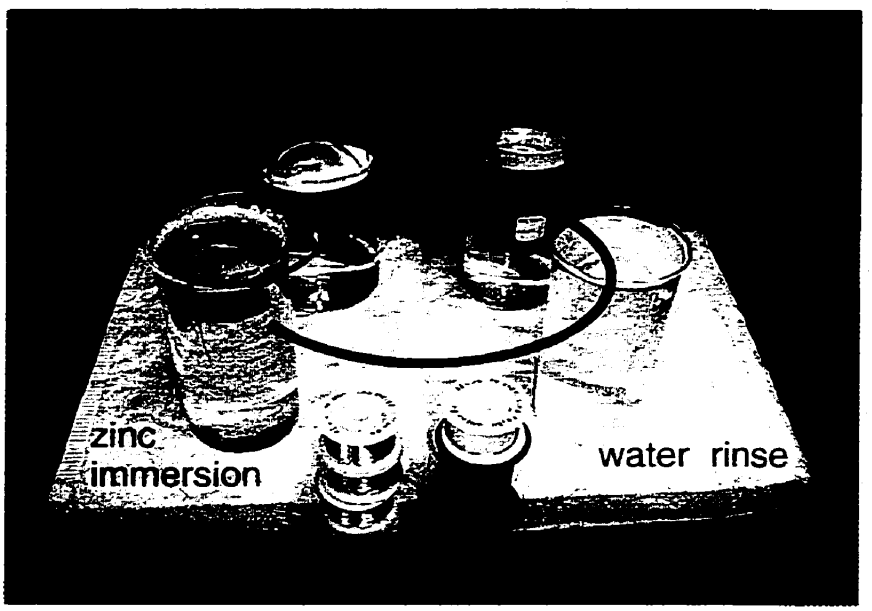

Fig. 4.10. Photograph of the zinc immersion plating station used to deposit a thin layer of zinc on the surface of the aluminium wire. The wire is physically cleaned and then immersed in the zinc immersion beaker for 5 minutes. The initial zinc deposit on the wire is quite irregular (see Fig. 4.11) so the zinc layer is stripped off in an 8M solution of nitric acid and the wire is then re-immersed in the zinc immersion solution. This cycle is repeated 6 times to yield an even layer on the aluminium wire that is suitable for further plating.

The immersion bath was strongly basic, containing 525g/L sodium hydroxide (13M), 100g/L zinc oxide, and 10g/L Rochelle salt formula. As aluminium oxide was etched off the wire, zinc was displaced from solution onto the aluminium surface. To improve the zinc-aluminium bond, the wire was rinsed in water and then dipped in an 8M solution of nitric acid to strip off the fresh zinc deposit. It was then rinsed again in water, and put back in the zinc immersion bath for another 5 minutes. (Two separate rinse basins are recommended, one for rinsing from the basic solution, and another for rinsing out the acid. Purified water, e.g. de-ionized water: resistivity $\geq$ 18MΩ-cm, is recommended in the rinse basins as well as for all other aqueous solutions.) This regimen was repeated six times, leaving finally, a silver-blue coloured layer of

zinc on the wire (see Fig. 4.11). The total time for the zinc immersion step was then approximately 6 cycles × 5 minutes/cycle ~30 minutes.

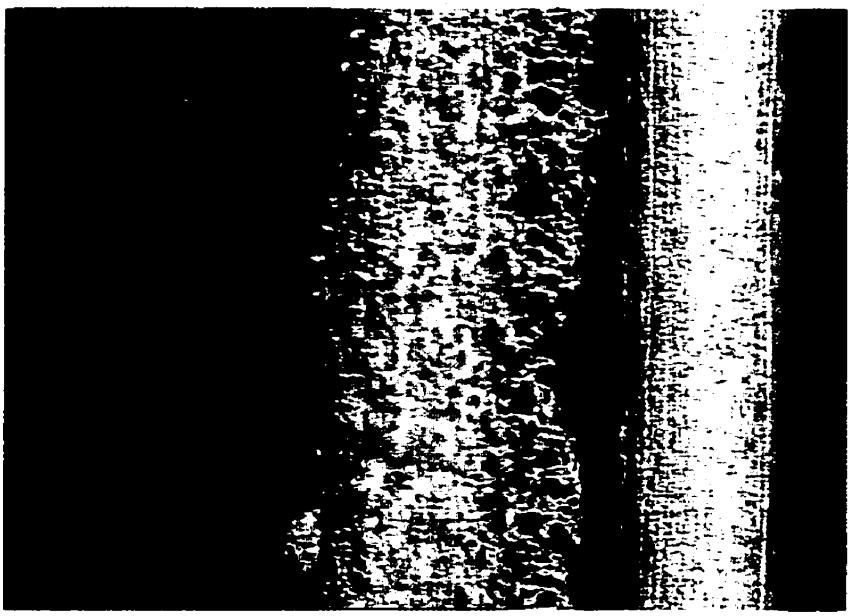

Fig. 4.11. Results from zinc plating in a zinc immersion solution. An aluminium wire 0.5mm diameter is successively coated with zinc from the zinc immersion solution: (left) bare; (middle) after one cycle; (right) after six cycles.

4.3.2 *Step 2. Copper Cyanide*

Unfortunately, subsequent copper plating in a standard sulphate-acid bath is not suitable. The zinc is quickly dissolved in the acidic environment while simultaneously undergoing a zinc-copper immersion reaction ($E_{0,Zn}$ =-0.76V). If the zinc is dissolved quickly enough, there is a risk of the immersion reaction involving aluminium and copper described earlier. Both the Zn/Cu and Al/Cu immersion reactions result in a poorly adherent copper layer, see Fig. 4.12. Thus, the first copper plating must be from an alkaline copper cyanide bath (also known as a copper strike). The bath composition is 40g/L cuprous cyanide, 45g/L sodium cyanide, 30g/L sodium carbonate, and 60g/L Rochelle salt(Parthasaradhy 1989). Here, the electrode potential of zinc in the solution of complexed copper-cyanide prevents an

immersion reaction (E_0 = −1.0 and −1.2 V for copper and zinc respectively). Possible immersion reactions are also kept to a minimum by applying potentials to the anode and cathode before the cathode is immersed in the bath (sometimes referred to as a "hot" start). For reproducible results, the anode was "cleaned" before the start of plating by immersion in an 8M HNO_3 solution for approximately 20 seconds and then water rinsed. Both the bath and the wire must be agitated (stirring the solution and rotating the wire) for an even deposit, as shown in Fig. 4.13. The speed of the stirring bar is important during the plating in the cyanide-based solution. If the stirring speed is too slow, then the plating potential rises due to the lack of fresh electrolyte at the surface of the wire. If the stirring speed is too high, the thin copper plate will peel away, thereby dooming further plating attempts.

Fig. 4.12. Acid-based copper electroplating results for aluminium (bottom left) and zinc immersion plated aluminium (top right) wires. Plating time was approximately 2½ minutes. Bare spots are visible on the aluminium wire and are also present on the zinc plated aluminium wire under higher magnification. However the improvement with zinc plating is substantial.

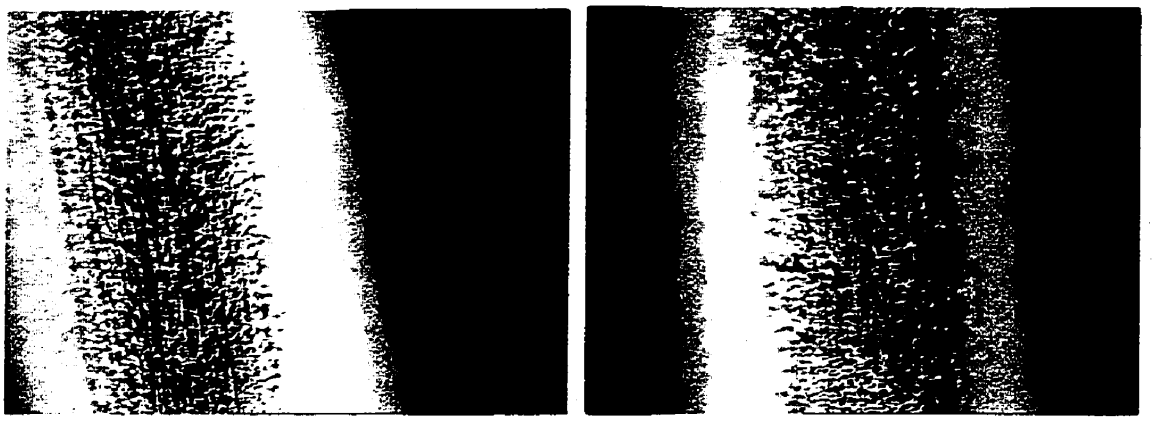

Fig. 4.13. Electroplating results for 0.5mm diameter aluminium wires that have been zinc plated with the zinc immersion process and then copper plated using cyanide-based copper. No bare aluminium regions are visible under magnification. The copper layer appears to distribute itself on the zinc-aluminium wire in such a way as to add a pink tint over the blue-silver coloured substrate. Plating time for the wires in the left and right photos was 1 minute and 10 minutes respectively.

With the aid of the constant current source, the zinc-coated aluminium wire was copper plated to a thickness of approximately 35nm, at a current density $J = 0.1\,\text{mA-cm}^{-2}$ (approx. 30 min.). The thickness of copper in this step was not an optimized value, but sufficient to prevent the zinc layer from reacting with the acid in the next copper sulphate (and sulphuric acid)-based solution. The thickness of copper deposited, the electrical current required, and plating time were estimated using the following equations. The charge, or number of electrons, that needs to be supplied to the cathode to displace a volume V of copper from solution onto the cathode is given by

$$\begin{aligned} Q &= VNze \\ &= VN_A \frac{\rho}{M} ze \end{aligned} \tag{4.14}$$

where N is the number of atoms per unit volume, z is the valence number for the chemical species, e is the electronic charge, N_A is Avagadro's number, ρ is the density, and M is the molar mass. In a plating operation, we expect the entire current passed to be utilized for

electroplating. If a fraction of the current is used for any other reaction (e.g. evolution of hydrogen gas) it is considered waste. The term *cathode efficiency* is used to express the mass of metal actually deposited relative to the mass which would be projected to be deposited based on the quantity of electric charge passed. In a copper cyanide bath the cathode efficiency is in the range of 30-60%(Parthasaradhy 1989), while in the copper acid bath, to be described shortly, the efficiency is 95-99%. The cathode efficiency is not explicitly written into Eq. (4.14), but must be included there if rigorous calculations are considered. The total charge is easily related to electrical current I, and time t, by $Q = It$. The volume of copper required to build up a copper layer starting on wire diameter a to a finished diameter b, is easily given by $V = \pi l\left(b^2 - a^2\right)$ where l is the length of the wire to be plated. Substituting these last two equations into Eq. (4.14) we have

$$I \times t = \pi l\left(b^2 - a^2\right) N_A \frac{\rho}{M} z e \quad . \tag{4.15}$$

In practice, the current is set by the required current density $J = I/A$, where A is the surface area of the wire immersed in the bath, i.e. $A = 2\pi r l$. Thus, the appropriate current setting is given by

$$I = J \times 2\pi r l \quad . \tag{4.16}$$

Note that if the current is fixed for the duration of the plating job, there will be an effective decrease in the current density as the wire increases in thickness from the starting diameter a to the finished diameter b. Changing the current to keep the current density constant throughout is possible, but complicates the estimate for the plating time. Finally, the plating time is given by

$$t = \frac{1}{2aJ_0}\left(b^2 - a^2\right) N_A \frac{\rho}{M} ze \tag{4.17}$$

where J_0 is the current density at the starting wire diameter at $r = a$.

The current density in this step ($J = 0.1\,\text{mA-cm}^{-2}$) is considerably lower than typical values found in the literature. (This is based mostly on experience). If too high a current density has been set, the cathode potential will be high (> ~400 mV) and the cathode will have a brownish "burnt" appearance. Incomplete water rinsing in passing from the zincate to the cyanide solution will also result in high plating potential and produce a brittle deposit. Thus, even though the power supply is operated in constant current mode, careful attention must be paid to the plating potential as well. Too low a potential (< ~80 mV) (usually due to abnormally low current density) will produce a dull finish that is not highly ductile. The plating potential varies substantially over the 30 minutes the wire remains in the cyanide bath. For example, using the apparatus described in this paper (see Fig. 4.6) and plating a 7 cm length of wire, the potential would initially be high (approx. 250 mV), would then fall dramatically (approx. 60 mV) and then settle somewhere in between (approx. 150 mV). This pattern of changing potential did not seem to depend on the wire thickness used in the development trials (i.e. 50 μm - 0.5 mm starting diameter). The finish of the wire coming out of this bath should be shiny and smooth to the naked eye. If this is not the case, inspect the wire under a good quality microscope with a power in the range of ×10 ~ ×40. If something has gone wrong, the copper deposits will appear to be forming small columns out of the surface of the wire with large patches of bare aluminium in between. Any further plating on this substrate would be pointless.

If a single stirrer and anode are used, then at the end of the copper cyanide plating, the wire cathode should be withdrawn from the electrolyte, water rinsed, and immediately placed in a temporary water bath to prevent the plated wire from drying. The beaker containing the copper cyanide solution is then withdrawn, the anode rinsed with water, and lastly the beaker with the copper sulphate solution put in place.

If a double stirrer and two anodes are being used, then the wire cathode should be withdrawn from the electrolyte, water rinsed, and immediately transferred to the copper sulphate plating solution.

Safety Precautions. Use of cyanide.

The electrolyte bath used in step 2 uses copper cyanide and sodium cyanide because of their unique effectiveness in electroplating copper on zinc. No attempts should be made to store, prepare, or handle mixtures of cyanide without a thorough understanding of the precautions that must be observed to avoid accidents. In the transition from step 2 to 3 (especially when only a single stirrer/anode are used), there is the possibility of a serious accident involving the generation of highly toxic hydrogen cyanide gas. This is due to the use of an acid-based electrolyte solution following the treatment with the cyanide-based solution. These solutions should never be allowed to mix. As a precaution, electroplating steps 2 and 3 should be conducted in a fume hood with a suitable spill kit and cyanide antidote kit (Supplier: Eli Lilly and Company, Indianapolis, IN) kept nearby.

4.3.3 Step 3. Copper Sulphate-Acid

The wire was next transferred with electrodes "hot" to a heavy plating solution based on one of two possible electrolytes. The first is a standard copper sulphate-acid bath: 200g/L copper sulphate and 50g/L sulphuric acid. The current density, $J = 20\text{mA-cm}^{-2}$, is suitable for

plating at room temperature on thin wires. Both the bath and the wire must be agitated as in Step 2. The stirring speed in the acid-based solution is not too critical as long as the plating potential does not rise due to a lack of fresh electrolyte. However, measures to enhance the surface smoothness (see Fig. 4.14) were found to be necessary. One method was to reverse regularly the direction of current (15s forward, 7.5s reverse) in order to reduce copper micro-crystal growth, see Fig. 4.15. The odd surface appearance obtained with this method did not seem to affect the ductility. However, the surface irregularities were unacceptably large and further work with this technique was not pursued.

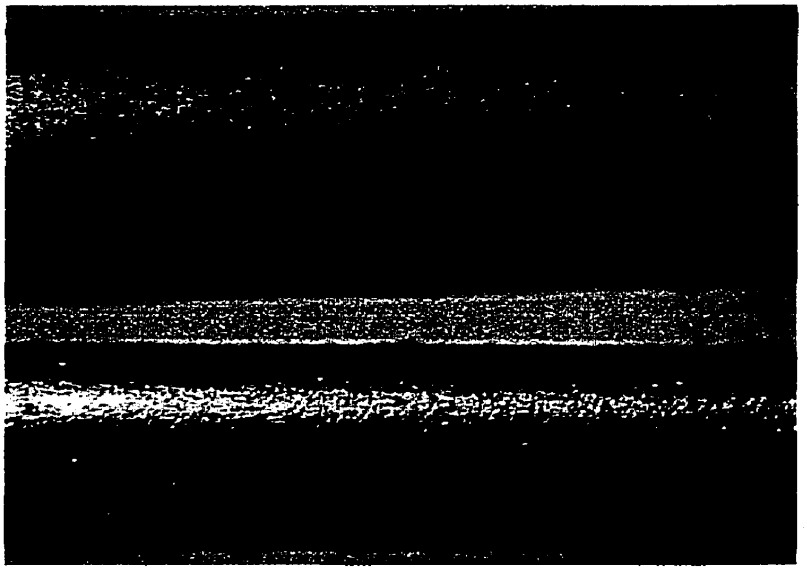

Fig. 4.14. Variation of surface appearance for different plating substrates. The photo shows heavy copper plating results on (top) a copper plated aluminium wire as prepared in Step 2, and (bottom) an ordinary copper wire. (No electroplating additives have been added yet.) Note the uneven surface obtained in both cases. An uneven surface precludes an accurate measurement of the wire's finished diameter. Any errors in the copper thickness will translate into susceptibility cancellation errors.

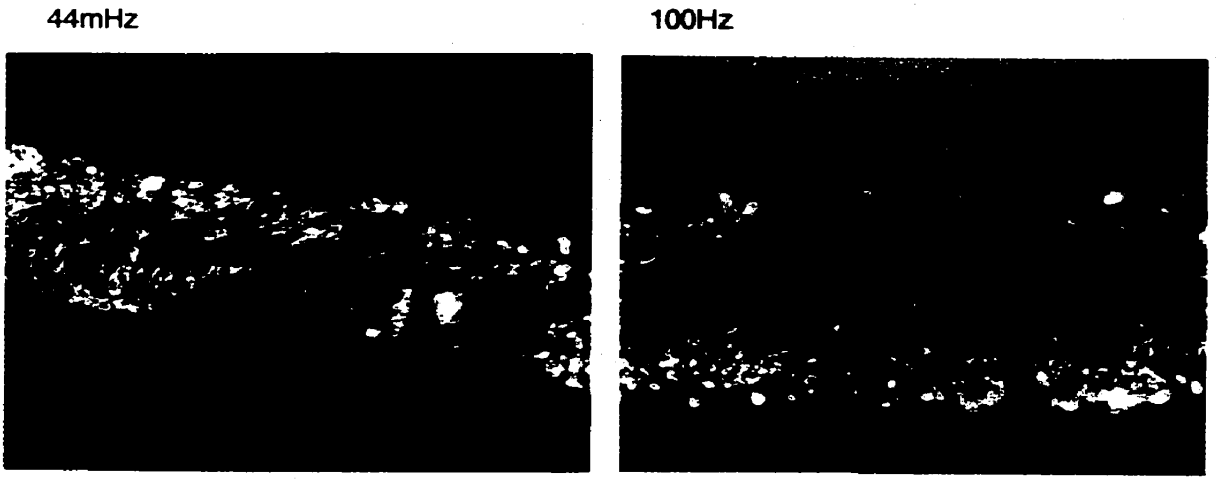

Fig. 4.15. Plating results from pulse plating experiments. In the left photo, the complete forward/reverse timing cycle was 22.7 seconds long. In the right photo, the cycle was 1millisecond long.

The second electrolyte is based on a slightly modified copper acid bath (180 g/L copper sulphate, 75g/L sulphuric acid, 0.2mL hydrochloric acid), current density $J = 20\text{mA-cm}^{-2}$, with the addition of commercial plating additives (Manufacturer: Enthone-OMI (Canada), Toronto, ON, Product: Udylite Bright Acid Copper (UBAC) Interplate). The additives enhance the grain refinement of the copper being deposited and a mirror smooth finish is possible as shown in Fig. 4.16. The proprietary UBAC Interplate Process normally includes three additives; (1)"Make-up", (2) "Maintenance", and (3) "Low". The "Low" additive is not used since its purpose is to increase surface hardness, which is the complement of ductility. As well, the "Maintenance" additive contains some of the "Low" and thus the "Maintenance" additive is used in the minimum useful concentration. The concentrations, given our ductility and surface smoothness requirements, are."Make-up"-1% and "Maintenance" - 0.02% (by volume). Plating current and time are set according to Eq.'s (4.16) and (4.17).

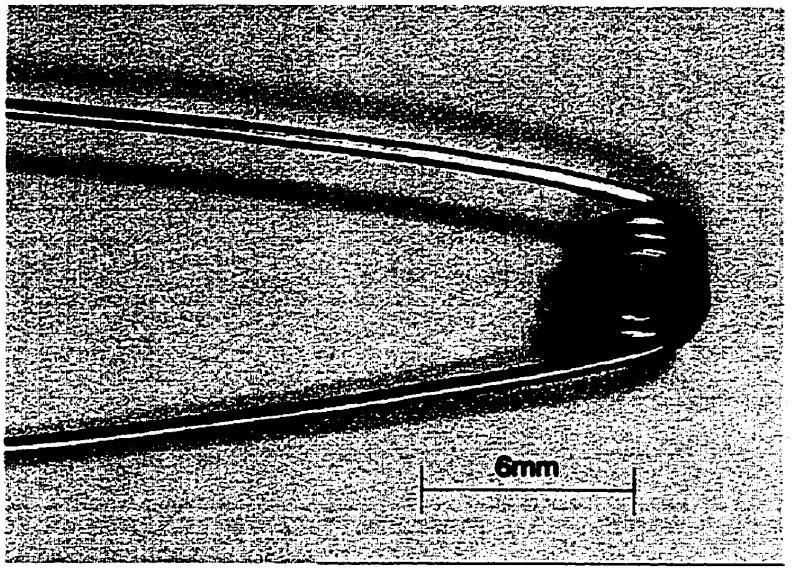

Fig. 4.16. An example of a finished solenoid winding made with copper plated wire using plating additives in the acid-based solution for heavy copper plating. (Note : The loop is formed after plating). The finished wire has a nearly mirror smooth finish although undulations on the scale of microns are still present when precise measurements are made.

When these additives are working properly, the anode develops a dark film on the surface. Watching for the presence of the film can be a useful aid in determining the correct operating conditions for the plating bath. For example, using the apparatus described in this chapter, the optimum potential in the copper/acid/additives bath was found to be around 200 $\pm$ 50mV ($J = 20\text{mA-cm}^{-2}$). Reducing the current density reduces the plating potential, but prevents a mirror smooth finish. It was also observed that with low current density the black film did not form on the anode. Reducing the current density further leads to problems with adhesion of the copper plate and an undesirable increase in the potential to around 400mV. Alternatively, if higher current densities are used, the wire has a mirror finish, but the deposit is not as ductile.

The UBAC Interplate additives are consumed during successive plating jobs, eventually leading to unsatisfactory results in both surface finish and ductility. One could begin each plating job with fresh solution, or if the same solution is used several times, keep a running log of current density, plating potential, and plated wire surface area. Then the operator will notice when the solution needs to be renewed by an unexplained increase in the plating potential, e.g. 50mV.

Strictly speaking, the UBAC Interplate additives are not "consumed" so much as decomposed during the operation of the bath as described. The reason for this is related to the operation of the anode. The anode is oxidized during plating and both Cu^{+} and Cu^{2+} ions are released into solution. When a fresh solution is prepared, including the proprietary additives, Cu^{+} ions released from the anode during plating will attack some organic components of the additives, thereby changing the formulation and overall effectiveness . The vulnerable organic additives (e.g. formaldehyde) can be destroyed within the first 10 minutes of operation. The ductility of the wire is not adversely affected by the early destruction of these organic components, but only a smooth, not a mirror smooth finish is possible. The solution can be used for quite some time before any significant changes are noticed in operating conditions (e.g. cathode potential). The cure for this problem has been mentioned earlier. The dark film that develops on the anode will selectively prevent Cu^{+} ions from entering the solution.

The filmed anode now becomes an important factor when making the choice to use a single stirring module/anode set-up or a double stirring module/anode set-up. In the case of a single stirring module/anode set-up, the anode must be cleaned thoroughly by wiping it with a tissue, briefly immersing it in 8M nitric acid, and rinsing it thoroughly with water. This is necessary to prevent contaminating the copper cyanide solution on the next plating job. The

effectiveness of the solution would have obviously been reduced by the initial operation of a "bare" anode, but not to the point that would be reached starting with an un-filmed anode in repeated plating jobs. If two stirring modules/anodes are used, then the anode in the copper sulphate solution does not need to be cleaned and can remain in the copper sulphate solution for the next job.

Another anode option for operation in the copper sulphate bath of the dual stirring modules/anodes set-up is the use of a copper phosphorised anode. Such an anode is specially designed for use in a copper sulphate bath with additives. The phosphorised anode should be conditioned, that is operated in such a way as to build up a dark film by running the anode in a dummy copper sulphate solution for half an hour or so. The formulation of the dummy solution is not too strict, e.g. 200g/L copper sulphate and 50g/L sulphuric acid, and current density, $J = 20 \sim 40 \text{mA-cm}^{-2}$. After conditioning, the filmed anode can be transferred to the working copper sulphate (with additives) solution. The film should be left undisturbed on the anode between successive experiments and the anode should remain immersed in solution at all times. A polypropylene mesh bag placed over the anode is sometimes used to prevent the film from being inadvertently removed or eroded.

The sequence of steps from the zinc immersion, the initial coating of copper from the cyanide bath, and finally heavy copper plating in the modified copper sulphate bath should be a continuous process. The wire under development should not remain out of solution for more than a few seconds if possible, especially between the zincate and first copper treatment. It must also be thoroughly rinsed between solutions. The most sensitive step in this respect is

the rinsing between the zincate and copper-cyanide based solution. All solutions are used at room temperature.

4.4 Wire Testing

After plating, the wires were evaluated for surface smoothness, ductility and nett susceptibility. (Surface smoothness was considered important only for accurate determination of the wire diameter, to be correlated later with susceptibility). Ductility was evaluated with a simple test. The finished wire was wound a half turn around a former just slightly larger in diameter than the finished wire (e.g. finished wire diameters in the range of 0.7-1.0 mm were bent around a 1mm diameter former), as shown in Fig. 4.17. The ductility test was considered successful if the wire did not crack or break. The evaluation of nett susceptibility was more involved.

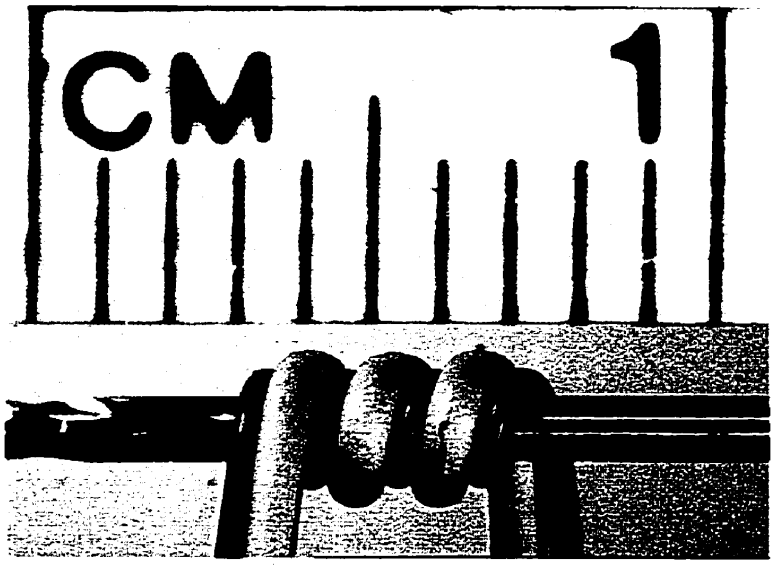

Fig. 4.17. Photograph of the bending involved in the test of ductility for finished plated wires. The test involved wrapping the wire around a 1mm steel twist drill and then inspecting the wire for any breaking or cracking. In practice a wire for a solenoid winding would never suffer this extreme bend radius, but the test was necessary to optimize the overall plating process on aluminium. A dummy wire is sometimes used to obtain a well-defined space between windings. (Note: The mark on the right winding is a scratch caused by the tools used in the winding process.)

4.4.1 *Test of Susceptibility: The Hairpin Loop Microprobe*

Since NMR is inherently sensitive to volumetric susceptibility (<.001ppm) (Fuks, Huang et al. 1992), we developed a special NMR probe for assessment of the plated wires (see Fig. 4.18).

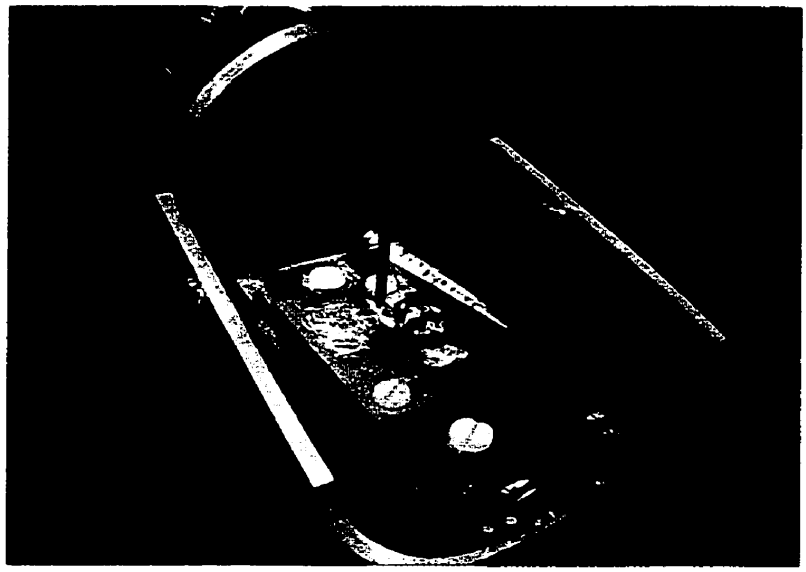

Fig. 4.18. Photo of the special NMR probe used to test susceptibility of the plated wires. The capillary containing water as a sample is *outside* the wire loop.

The probe incorporates the plated wire under test as the RF coil in the shape of a hairpin with long leads (~25mm) and an inside diameter (ID) of 1mm, connected to a tuning and matching network as shown in Fig. 4.19. A thin capillary tube (OD 1mm, ID 0.8mm, length 80mm, Manufacturer: Wilmad Glass, NJ), containing pure water is placed beside one of the long leads of the coil. The orientation of the tube is perpendicular to the main B_0 field. The intention here is to affect radically the NMR signal by perturbing the B_0 field by the close proximity of the wire with non-zero susceptibility under test. Placing the water-filled capillary *outside* the loop, as opposed to inside the loop, maximizes the distortion due to the wire alone. Other probe components are intended to affect the B_0 field minimally. The water-filled capillary tube will

not contribute any magnetic field non-uniformity in the water-filled interior, a property of right circular cylinders perpendicular to a magnetic field described in Chapter 2. The tuning and matching capacitors that could possibly perturb the B_0 field are kept at a safe distance by the long wire leads.

Several NMR experiments were possible with this probe to evaluate the effective susceptibility of the wire under test. The simplest was to use a single RF pulse to flip spins in the water-filled capillary near the wire and then acquire the NMR signal from the sample. The frequency spectrum of the signal depended, in a complicated way, on the distributions of static magnetic field $\mathbf{B}_{final}$, the magnetic B_1 field, and flip angle throughout the sample. A copper-aluminium wire constructed according to zero-susceptibility dimensions given in Eq. (4.3) should give the narrowest spectral width. The objective of the susceptibility test was therefore to verify experimentally the predicted dimensions of zero susceptibility copper-aluminium wire by plotting linewidth against overall wire diameter.

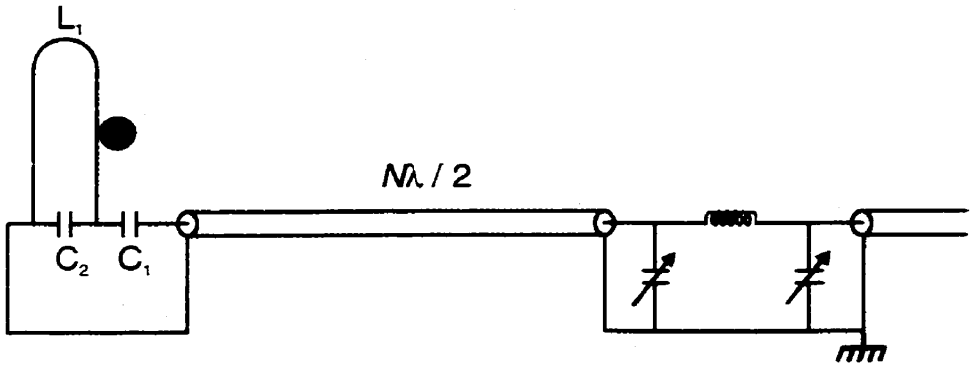

Fig. 4.19. Schematic drawing of the special NMR probe. The probe comprised two sections connected by an $N\lambda/2$ length of cable. The first section was the RF coil (test wire) with fixed-value tuning and matching capacitors. The second section was a π-section tuning and matching network that could be adjusted outside the magnet bore. The position of the water sample with respect to the test RF wire is shown in blue.

4.4.1.1 Magnetostatic description of the field perturbation due to the RF coil

The basic equations for the field perturbation due to the RF coil have been presented earlier in Chapter 4 (refer §4.2.1). Recall that for a single long wire (i.e. neglecting end effects) oriented perpendicular to the direction of the static magnetic field $\mathbf{B}_0$, the final magnetic field in a plane perpendicular to the axis of the wire was given by

$$\text{single wire only: } \mathbf{B}_{final}(r,\theta) = \mathbf{B}_0 + \frac{B_0 b^2}{2r^2}\chi\left[\cos\theta\,\hat{\mathbf{e}}_r + \sin\theta\,\hat{\mathbf{e}}_\theta\right], \qquad r \geq b \tag{4.18}$$

where b is the radius of the wire, and r is the distance from the centre of the wire (along the wire axis) to a field point in the plane. From Eq. (4.18) we see that the field is composed of the original static field $\mathbf{B}_0$ plus a perturbation term. The perturbation term is proportional to the susceptibility of the wire χ which, in the case of copper wire, means that the perturbation is roughly 10^{-5} times weaker than the static $\mathbf{B}_0$ field. Note that in Eq. (4.18) the magnetic field perturbation at the surface of the wire is independent of wire diameter, i.e.

$$\frac{\chi B_0}{2}\left(\frac{b}{b}\right)^2 = \frac{\chi B_0}{2} \quad . \tag{4.19}$$

For example, in a 9.4T field, the perturbation for copper is 45.3μT, or in terms of a shift in the resonance frequency, 1,927 Hz for the proton resonance. NMR spectral line broadening related to wire susceptibility is therefore dependent on the relative size of wire to capillary wall thickness and distance spanned by the sample, but independent of the absolute size of the wire.

The geometry for two wires is given in Fig. 4. 20. The magnetic field at any field point exterior to the conductors is simply the vector sum of the single wire perturbations. If we ignore the second order perturbations, i.e. χ^2 and higher, then the final magnetic field may be written as

$$\mathbf{B}_{final}(r_1,\theta_1,r_2,\theta_2)=\mathbf{B}_0+\frac{B_0\chi b^2}{2r_1^2}\left[\cos\theta_1\,\hat{e}_{r_1}+\sin\theta_1\,\hat{e}_{\theta_1}\right]+\frac{B_0\chi b^2}{2r_2^2}\left[\cos\theta_2\,\hat{e}_{r_2}+\sin\theta_2\,\hat{e}_{\theta_2}\right] \quad (4.20)$$

The unit vectors $\hat{e}_{r_1},\hat{e}_{r_2},\hat{e}_{\theta_1},\hat{e}_{\theta_1}$ are unique for each field point and must be rewritten in terms of the unit vectors $\hat{e}_y$ and $\hat{e}_z$. To do this we use the transformation equations

$$\begin{aligned}\hat{e}_r&=\hat{e}_z\cos\theta+\hat{e}_y\sin\theta,\\ \hat{e}_\theta&=-\hat{e}_z\sin\theta+\hat{e}_y\cos\theta.\end{aligned} \quad (4.21)$$

Finally, only the z component of the magnetic field is significant. It may be written in terms of r, z, and y as

$$B_{z,final}(r,z,y)=B_0+\frac{B_0\chi b^2}{r^4}\left[\left(z^2-y^2+c^2\right)\right], \quad (4.22)$$

where c is the distance each wire centre is displaced from the origin along the z-axis.

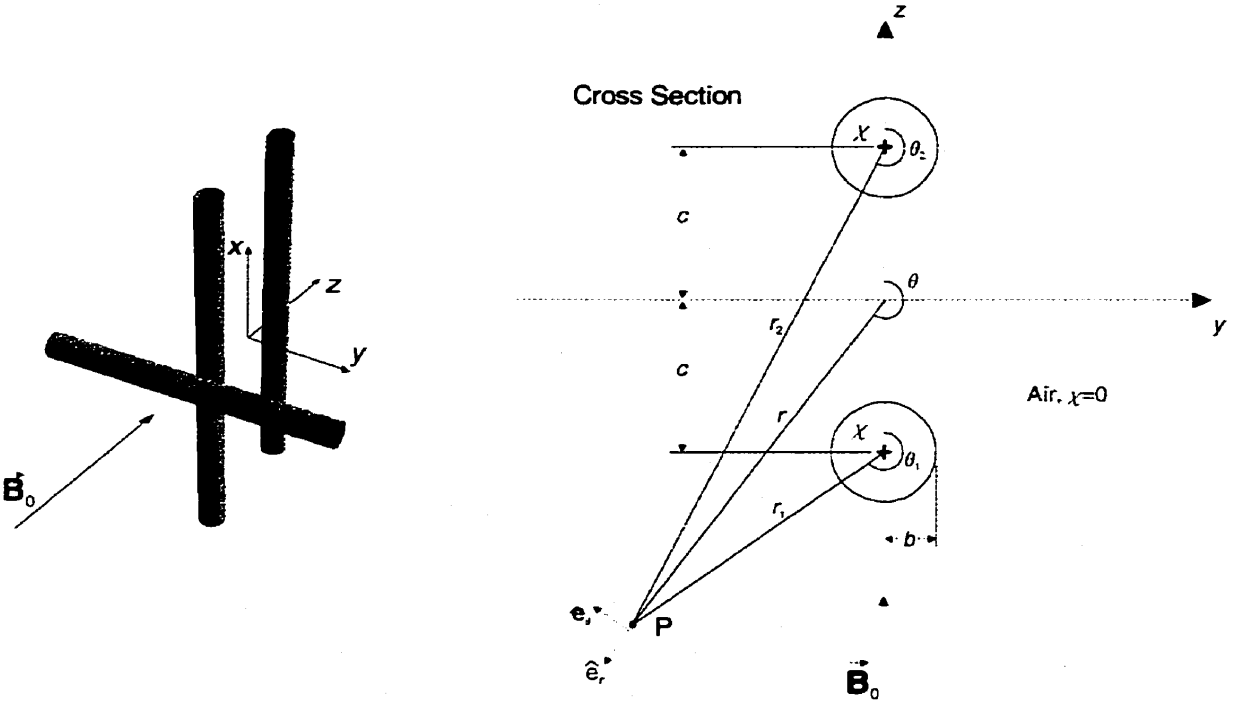

Fig. 4. 20. Cross-section of the wire pair in the y-z plane. A field point P is drawn to a point in the water sample inside the capillary tube.

A computer simulation of the observed NMR spectra

A computer program to calculate the magnetic field in the volume of interest, i.e. the sample, and hence the sample's NMR spectrum was written in the high-level language Mathematica. The program is based on the following algorithm. Field points are arranged on a grid in the $x=0$ plane as shown in Fig. 4. 21.

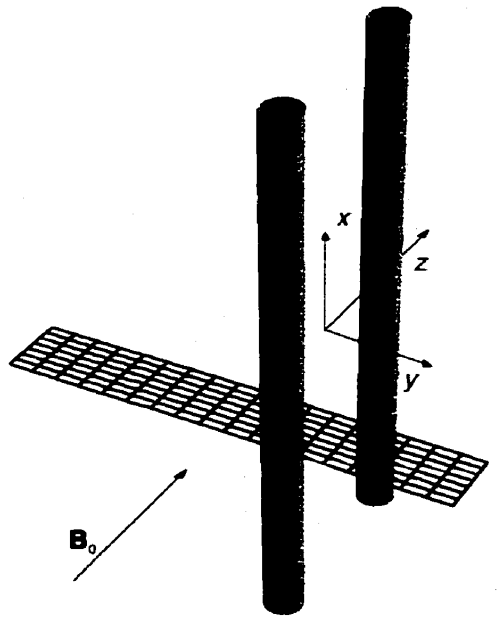

Fig. 4. 21. The grid indicates the field points positions for the magnetostatic calculations. The width of the grid corresponds to the inner diameter of the water-filled capillary tube and the length of the grid corresponds to the effective range of the B_1 field.

The z-component of the magnetostatic field was calculated at each field point using Eq. (4.22). An entire row of field points at a constant z value was calculated and stored in a one-dimensional array of length n where n is the number of field points. The magnetic values were then binned in order to build a histogram of the magnetic field values encountered in the row of field points. The histogram was then multiplied by a weighting factor. This factor was defined by the corresponding height of the capillary tube at that row position. In this way, the

weight factor reflected the "amount" of (water) sample above and below the $x=0$ plane. Due to symmetry in the magnetic field in the x-direction, and the symmetry of the sample vessel in the y-direction, the weighting was a function of the z-coordinate only. The weight function $w(z)$ for a capillary tube with a circular cross section is given by

$$w(z)=\sqrt{\rho^2-(z-d)^2} \tag{4.23}$$

where ρ is the (inner) diameter of the capillary tube, and $-d$ is the distance the between the centre of the long axis of the wire and the centre of the long axis of the capillary as shown in Fig. 4.22. Strictly speaking, the weight function $w(z)$ in Eq. (4.23) describes a half circle, and is therefore missing a factor of 2 for a circular cross section. This constant can be ignored for our purposes as it only has the uninteresting effect of doubling the height of the histogram.

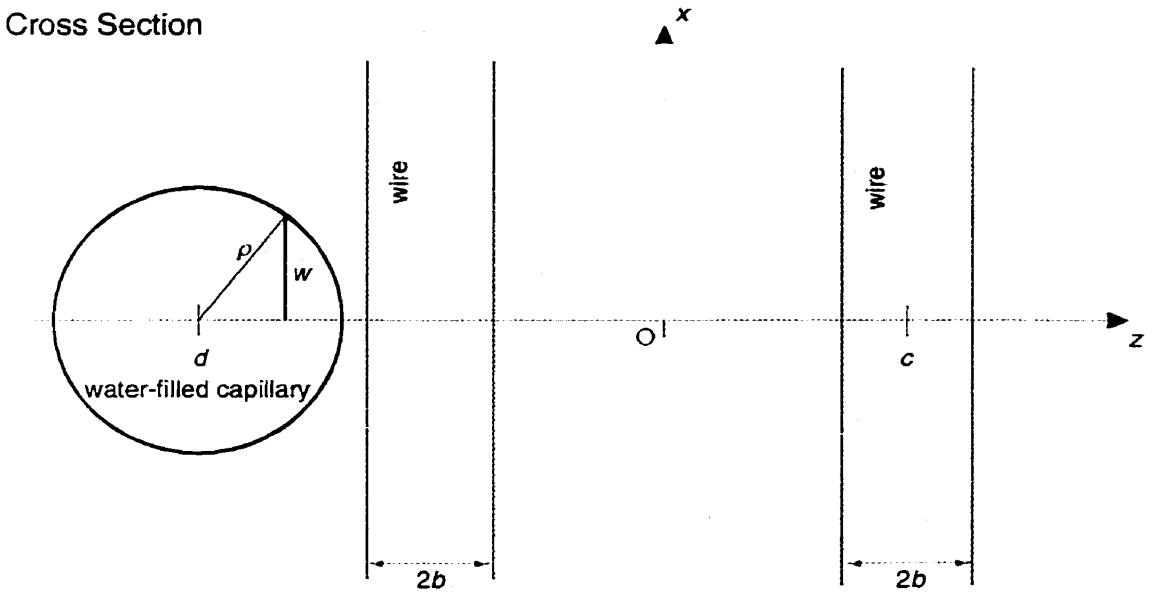

Fig. 4. 22. Cross section of the capillary tube and long wires. The wires extend to ±13 mm in the x-direction. The capillary tube extends into and out of the page (i.e. in the y-axis direction).

A histogram was determined for all rows in the field point grid and then all histograms were summed to represent the spectrum of field values over the entire grid. A sample spectrum is presented in Fig. 4. 23. We see from the figure that the line shape is highly dependent on the susceptibility of the wire used. The bimodal line shape results from two dominant magnetic environments in the water sample. One peak is related to *regions* in the sample that are highly perturbed from the initial $\mathbf{B}_0$ value. The other peak is related to the *regions* in the sample that are relatively unperturbed by the presence and proximity of the wire. This pattern is also observed in experimental data to be shown. The size of the field point grid is some arbitrary in this respect, and should be chosen to resemble the range of the B_1 field. The "noise" on the spectra arises from the grid size considered. Also, the peak at 0 Hz is due to a counting error in the program and is not meant to predict an spike in the experimental data.

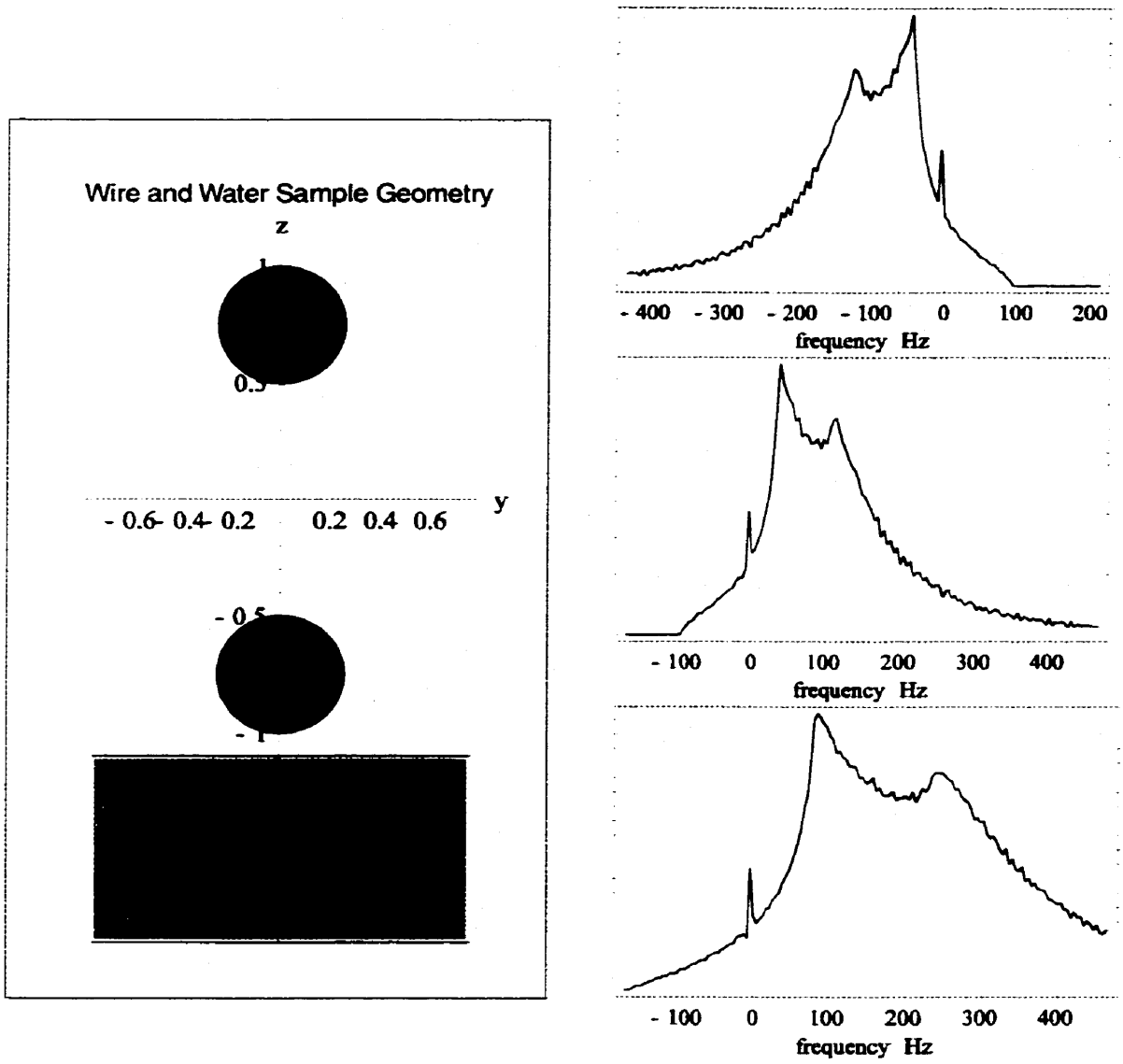

Fig. 4. 23. Sample spectra from the computer simulation. The top spectrum was obtained using copper wire conductors. As a check of the proper functioning of the program, the susceptibility of the metal was mathematically reversed which then produced the middle spectrum. The bottom spectrum was computed using the susceptibility of aluminium wire conductors. The full width at half maximum of this spectrum is roughly twice the FWHM of the copper wire spectrum as expected from a direct comparison of susceptibilities. The spike at 0Hz is related to an artefact in the program.

4.4.1.2 B_1

Current flowing in each leg of the RF coil produces a magnetic B_1 field in the form of concentric azimuthal circles as previously described in Chapter 3. However, the important

difference here is the orientation of the wires with respect to the static B_0 field. Since the wires are perpendicular to B_0 the azimuthal B_1 field is not in general perpendicular to B_0. We can see this by examining the individual fields produced by current flowing in each wire, and then their vector sum. Individually the B_1 field produced by the current in each wire is given by

$$\begin{aligned}\mathbf{B}_1(r_1,\theta_1) &= \frac{\mu_0 i}{2\pi r_1}\hat{\mathbf{e}}_{\theta_1} \\ \mathbf{B}_2(r_2,\theta_2) &= -\frac{\mu_0 i}{2\pi r_2}\hat{\mathbf{e}}_{\theta_2}\end{aligned} \tag{4.24}$$

where the geometry of Fig. 4. 20 has been used. The overall field is obtained by summing the $\mathbf{B}_1$ and $\mathbf{B}_2$ fields in Eq. (4.24). From the NMR perspective, only the component of B_1 that is perpendicular to the $\mathbf{B}_0$ field is relevant to the experiment, i.e. in this case the $\hat{\mathbf{e}}_y$ component. Thus we may use Eq.'s (4.21), (4.22) with Eq.(4.24) to derive the equation for the y-component of the B_1 field:

$$B_{1,y}(z,y) = \frac{\mu_0 i}{2\pi}\left(\frac{z-c}{(z-c)^2+y^2} - \frac{z+c}{(z+c)^2+y^2}\right) \tag{4.25}$$

If we set $B_{1,y}(z,y) = 0$ in Eq. (4.25) we can find the locus of points where the y-component of the B_1 field is zero. This yields the curves

$$y^2 = (z-c)(z+c) \tag{4.26}$$

Fig. 4. 24 show the curves defined by Eq. (4.26) overlaid on the geometry for the computed line shapes from Fig. 4. 23.

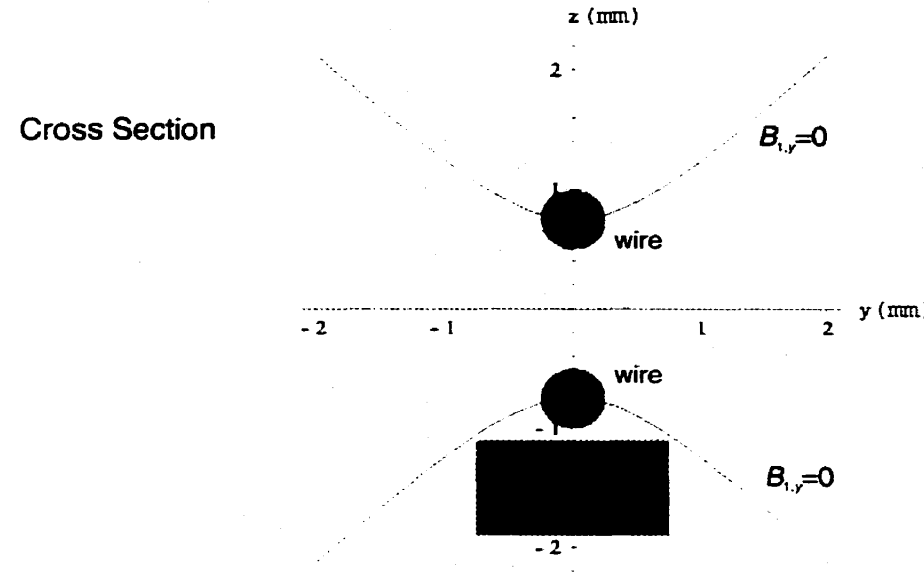

Fig. 4. 24. $B_{1,y}$=0 curves overlaid on the geometry used for the computer-simulated spectrum of 4.23.

4.4.2 *NMR experiments*

NMR experiments were performed on a 9.4T (400MHz) wide-bore (21cm) imaging magnet (Manufacturer: Magnex, Console: Bruker Biospec). The advantage of a high field system as stated earlier, is that the susceptibility artefacts scale as B_0 field strength, which for our non-traditional purposes, make them easier to detect. The initial task before the experiments could begin was to obtain a uniform B_0 field in the magnet. We obtained the closest approximation to such a field by carrying out several initial experiments with the special NMR probe and a collection of candidate zero susceptibility wires. Each wire was successively fitted in the special probe in an attempt to find the inherently narrowest associated water spectrum of the series. Transmitter power and pulse duration were the same for all samples and the effective flip angle was kept well below 90 degrees to ensure a linear response. Using the "best" candidate zero susceptibility wire, the magnetic field was shimmed using x, y, and z

shims only. The shim values were then held constant for further experiments. Drift of the field of the magnet was not a problem in the time scale of the experiments.

4.4.2.1 Data

Only copper-plated aluminium wires that passed the test for ductility were considered for further susceptibility analysis. This total came to twenty-three wires in various final plated diameters from 590-981 μm all based on a starting aluminium wire diameter of 0.5mm. However, 10 of these wires were disqualified because they had a rough, or uneven, plated surface. A rough surface makes the determination of wire diameter difficult since a determination with a micrometer will measure only the outside diameter of the rough wire. Thus, any attempt to correlate wire diameter and susceptibility would be flawed. Even the wires that appeared smooth had local surface irregularities smaller than the width of the jaw face of the micrometer used here. A blade micrometer (Manufacturer: Mitutoyo, Model: 422-341-30) with a blade width of 0.4 mm and resolution of 1μm was used for all measurements. Diameter measurements were made at several places along the length of the wire, especially in the region that would be near the sample in the NMR experiment. The average and approximate standard deviation of these measurements on the 13 remaining wires plus a bare aluminium wire with a diameter of 498 μm is given in Table 4.3.

Table 4.3. Data from the susceptibility testing experiments. Experiments used a 0.5mm diameter bare aluminium wire for the RF coil. Wires were manufactured with increasing thickness of copper on this starting diameter of aluminium. The final plated diameter is given in the "Wire diameter" column in the table.

Experiment Number	Wire diameter (μm)	Integral Width (Hz)
1 (Al wire)	498 ± 3	800 ± 85
2	590 ± 1	610 ±66
3	677 ± 1	549 ±60
4	756 ± 1	274 ±32
5	816 ± 3	122 ±17
6	877 ± 3	31 ±13
7	885 ± 2	23 ±12
8	912 ± 2	-46 ±15
9	914 ± 2	-62 ±16
10	925 ± 3	-87 ±14
11	937 ± 2	-101 ±15
12	961 ± 1	-171 ±22
13	972 ± 3	-159 ±21
14	981 ± 3	-195 ±25

Typical spectra from the copper-plated aluminium wire data set are shown in Fig. 4.25. As predicted by the computer simulations of the experiment in the previous section, we note that each spectrum has two peaks. As in the simulation, if we ignore the dependencies of signal shape on the B_1 field and related flip angle distribution, we may interpret the spectrum as an indication of magnetic field strength over the sample volume. In this light, we infer there are two dominant (static) magnetic environments represented by the two peaks. It is believed that one peak is due roughly to received signal within the range of the generated B_1 field, but out of the range of the B_0 perturbing effects of the wire under test. The second peak is due to the received signal in the volume nearest the test wire (refer Fig. 4.24). By this logic, one peak should change position depending on the susceptibility of the particular test wire in place and the other peak should not shift position. This may be seen to be the case in the sequence of spectra in Fig. 4.25 for three different copper-plated aluminium wires. Once the investigator is

familiar with the position of these peaks after a few initial experiments, it is obvious if too much or too little copper has been plated.

The inhomogeneity caused by the wire was quantitatively assessed from the spectral width, as measured between the 10% and 90% points in the spectra's integral. This width was then recorded in Table 4.3, together with the wire diameter and estimated uncertainties. Negative spectral widths are possible in the sense that they reflect the asymmetry of the spectral line (refer Fig. 4.25). The data are plotted in Fig. 4.26. An analytical expression for the fit to the data does not exist due to the complexity of the experimental situation. An empirical fit to the data is discussed in the Data Analysis Section.

A theoretical curve is also included in Fig. 4.26 based on the computer-generated lineshapes presented in Section 4.4.1.1. D. I. Hoult further developed the lineshape algorithm used there. in order to include the effect of the inhomogeneous B_1 field in the NMR sample. The B_1-corrected lineshapes were then integrated to determine integral width (as was done with the experimental data). The curve in Fig. 4.26 indicated, to a first approximation, that the variation is approximately linear but with slight curvature. The data fit well to a power-series polynomial of order two:

Fig. 4.25. (next page) Demonstration spectra for a water sample in the special NMR test probe using copper-plated aluminium wire for the RF coil in the "half-loop" position. The plots show a shifting peak in the spectrum that is correlated with the thickness of copper on the aluminium wires. For all three plots the starting thickness of the aluminium wire is 500μm. Then in (a) total plated thickness: 817μm: too little copper; (b) 863μm: still too little copper; and (c) 885μm: just a little too much copper. At the correct susceptibility cancellation, the peaks merge. To quantify the effect of the susceptibility of the RF coil, the water spectrum is integrated and normalized to 100%. The width between the 10% and 90% points is recorded and then correlated with the particulars of the RF coil.

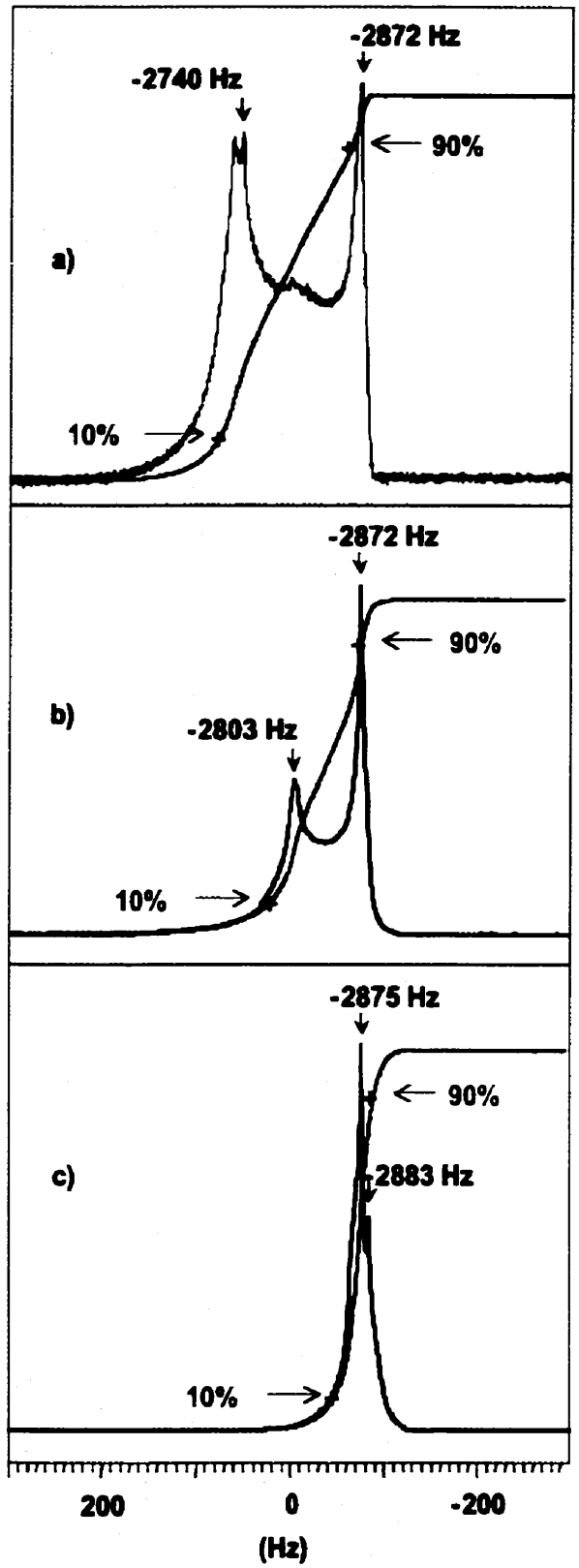
-2872 Hz
-2740 Hz
90%
a)
10%
-2872 Hz
90%
b)
-2803 Hz
10%
-2875 Hz
90%
c)
2883 Hz
10%
200
0
-200
(Hz)

$$y = 2787 - 4.785x + 1.805\times10^{-3}x^2 \qquad (4.27)$$

where x is the wire diameter in microns and y is the integral width in Hz.

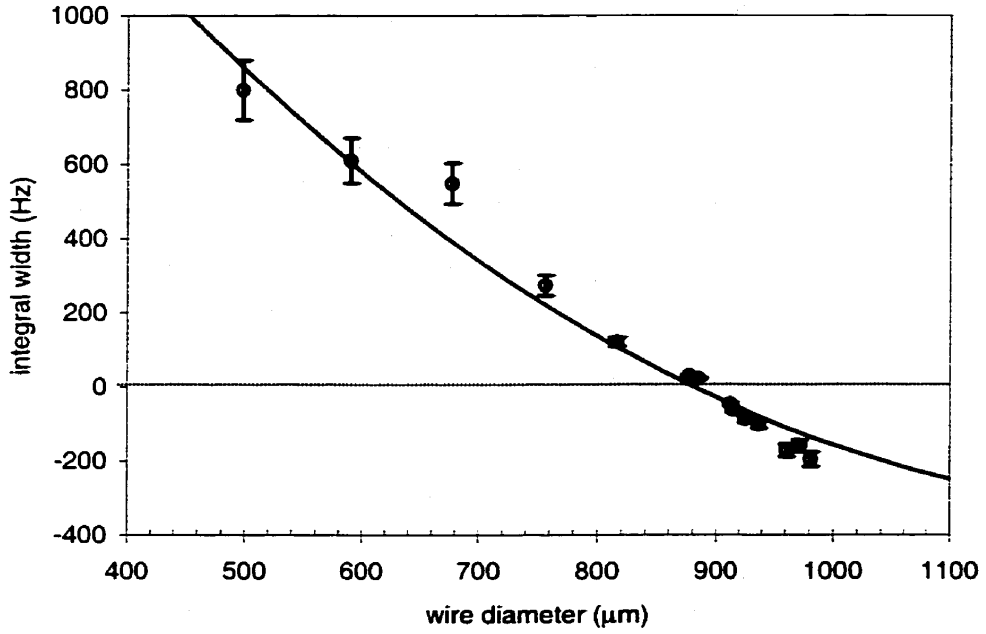

Fig. 4.26. Predicted and experimental Integral Width versus Wire Diameter for the 14 test wires that were used to study the change in susceptibility as the layer of copper on the aluminium wire increased. Error bars for the wire diameter are smaller than the central dot used to mark position. The $y = 0$ intercept corresponds to the copper-on-aluminium thickness that gives zero susceptibility wire.

Discussion of Data Uncertainties

Uncertainties in the wire diameter were discussed in the previous section. Uncertainties in the integral width may arise from several sources such as (1) changes in the flip angle distribution in the water-filled capillary due to a change in RF coil transmit current from RF coil to coil, (2) wire positioning errors when the coil is removed and substituted with the next test coil, (3) unanticipated changes in the plating chemistry that affects the susceptibility of the deposited copper metal, (4) data processing uncertainties arising from the finite resolution in

the water spectra and thereafter uncertainties in the spectral integral due to noise, and finally (5) scanner instabilities.

One of these sources of error was investigated for its possible effect on the spectral integral width, namely the flip angle distribution in the water-filled capillary. The relationship between flip angle and integral width was tested in a series of experiments where the transmitted power to the probe was changed in 1dB steps and the effect on the integral width was noted. The special NMR probe was fitted with the RF coil of diameter of 972μm. The wire used as the RF coil for this experiment generated a substantial amount of B_0 inhomogeneity when placed in the magnet. At each transmit-power setting, a free induction decay was obtained, then Fourier transformed, and then the integral width from 10% to 90% was found and recorded. The transmit-power was controlled with an external attenuation unit connected inline with the input to the RF power amplifier. The input attenuation was varied from –8dB to –15dB, representing an 80% reduction in power, with an equivalent reduction in the flip angle. The data are presented in Table 4.4.

Table 4.4. NMR data for the experiment to examine the relationship between flip angle distribution (or transmit power) and integrated peak width of the analyzed free induction decay.

Experiment Number	Input Attenuation (dB)	Integral Width (Hz)
1	-8	222.7
2	-9	236.5
3	-10	229.6
4	-11	247.1
5	-12	238.8
6	-13	249.4
7	-14	239.6
8	-15	233.8

The data in Table 4.4 are plotted in Fig. 4.27. By inspection of the data in this figure, we assumed that integral width is independent of flip angle – at least for the chosen power levels. Thus, we performed a fit of the data to a horizontal line. The fit parameters are plotted in Fig. 4.27 including the value of the average integral width (237Hz) and the sample standard deviation (9 Hz). We can also express the uncertainty in integral width as a fractional error, 9Hz/237Hz=4%. The assumption to fit the data in Table 4.4 to a horizontal line is checked by inspection of the spectra for experiments 1 (-8dB attenuation) and experiment 2 (-15dB attenuation). These two spectra taken from extreme values in the transmit power show that the overall peak shape does not change significantly.

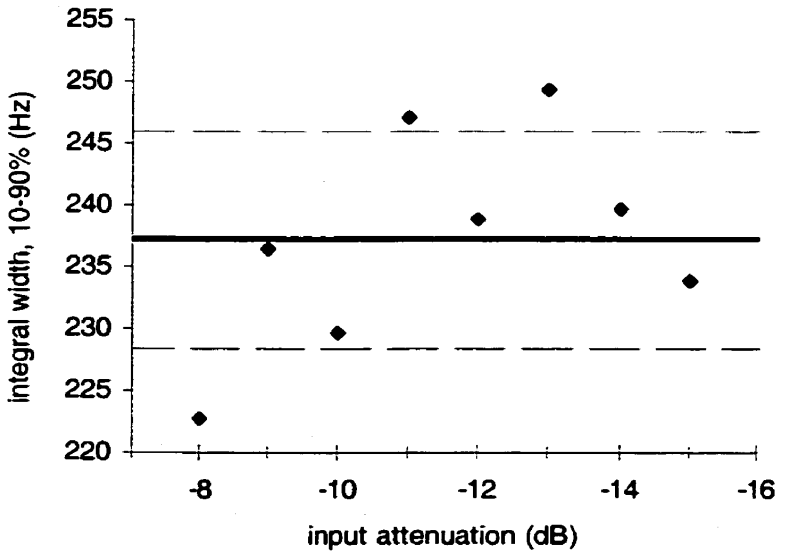

Fig. 4.27. Test results plotting the observed effect of transmit power to the probe (effectively changing the flip angle distribution) on integral width. Transmit power was adjusted by attenuating the input signal to the 300W power amplifier. Flip angles are much less than 90° although an exact calibration relating input attenuation and flip angle was not performed. The average value and the sample standard deviation (i.e. $n-1$ formula) are also indicated in the figure.

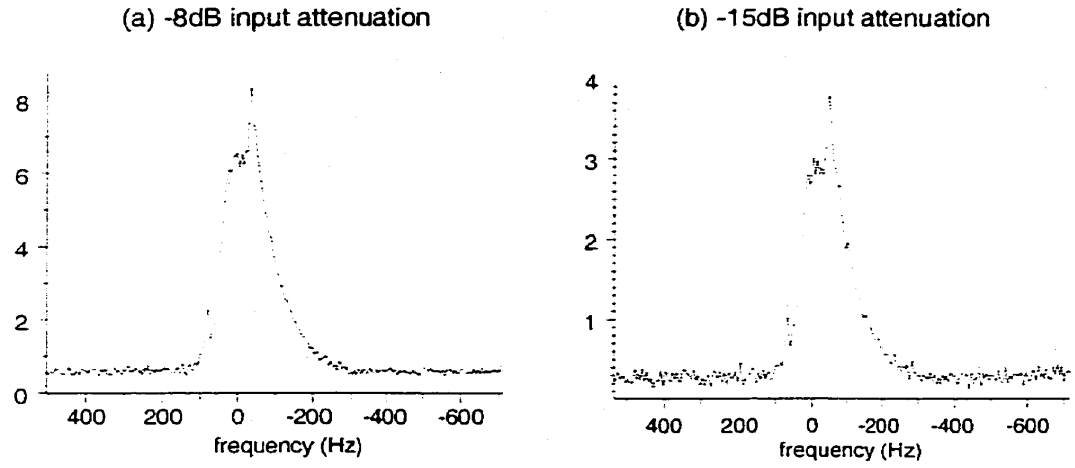

Fig. 4.28. Fourier transforms of the free induction decays in the flip angle-peak width experiments. In figure (a) the input attenuation was set to –8dB which results in a large flip angle (albeit <90°) and in figure (b) the power was reduced to 20% of the setting in (a). The peak shape was nearly unchanged but there was an increase in the noise level.

The advantage of the flip angle experiment is that it also implicitly included an estimate for the uncertainties arising from data processing (item 4) and scanner instabilities (item 5). However, uncertainties arising from data processing likely do not scale as a relative percentage of the integral width, but rather as a small fixed amount that is constant from experiment to experiment. We have estimated this uncertainty to be approximately ± 10Hz. Uncertainties related to wire and capillary positioning (item 2) and plating chemistry changes (item 3) were not explicitly assessed, but assumed to be on the order of 5%. Therefore, we combined these uncertainties according to

$$\text{integral width uncertainty} = (5\% + 5\%) \times \text{integral width} + 10\ \text{Hz} \tag{4.28}$$

to estimate the uncertainty in integral width in Table 4.3.

4.4.2.2 Data Analysis

The objective of the data analysis is to determine the *zero-crossing* at zero integrated peak width (i.e. $y = 0$). Based on the rudimentary computer simulation mentioned earlier (refer Fig. 4.26), we expect these data to fit a quadratic curve of the form,

$$y = c_0 + c_1 x + c_2 x^2 \tag{4.29}$$

where y is the integral width, x is the wire diameter, c_n are coefficients determined by fitting. The zero-crossing on the x-axis is obtained by setting $y = 0$ in Eq. (4.29) and solving for x:

$$x(y=0) = x_c = \frac{-c_1 \pm \sqrt{c_1^2 - 4c_0c_2}}{2c_2} \tag{4.30}$$

Input data for the fit are taken from Table 4.3 in the form $(x_i, y_i \pm \sigma_i)$ where $y_i \pm \sigma_i$ is the integral width including uncertainty, and x_i is the wire diameter. We assumed, for simplicity, that all the uncertainty of the measurement could be assigned to the dependent quantity, the integral width, as the error in the wire diameter is quite small. (The relative errors of the wire diameter measurement are ≤1%.)

We use the standard method of *least-squares* in order to optimize the values of the coefficients c_n in our fit to the quadratic curve (Bevington 1969). The method of least squares requires that we minimize χ^2, a measure of goodness of fit to the data.

$$\chi^2 \equiv \sum \left(\frac{\Delta y_i}{\sigma_i} \right)^2 = \sum \left[\frac{1}{\sigma_i^2} \left(y_i - c_0 - c_1 x_i - c_2 x_i^2 \right) \right] \tag{4.31}$$

where Δy_i is the difference between the each of the observed values y_i and the corresponding calculated values on the fitted curve. The optimum values for the coefficients are found in terms of determinants

$$c_0 = \frac{1}{\Delta}\begin{vmatrix} \sum\frac{y_i}{\sigma_i^2} & \sum\frac{x_i}{\sigma_i^2} & \sum\frac{x_i^2}{\sigma_i^2} \\ \sum\frac{x_i y_i}{\sigma_i^2} & \sum\frac{x_i^2}{\sigma_i^2} & \sum\frac{x_i^3}{\sigma_i^2} \\ \sum\frac{x_i^2 y_i}{\sigma_i^2} & \sum\frac{x_i^3}{\sigma_i^2} & \sum\frac{x_i^4}{\sigma_i^2} \end{vmatrix} \quad , \quad c_1 = \frac{1}{\Delta}\begin{vmatrix} \sum\frac{1}{\sigma_i^2} & \sum\frac{x_i y_i}{\sigma_i^2} & \sum\frac{x_i^2}{\sigma_i^2} \\ \sum\frac{x_i}{\sigma_i^2} & \sum\frac{x_i^2 y_i}{\sigma_i^2} & \sum\frac{x_i^3}{\sigma_i^2} \\ \sum\frac{x_i^2}{\sigma_i^2} & \sum\frac{x_i^3 y_i}{\sigma_i^2} & \sum\frac{x_i^4}{\sigma_i^2} \end{vmatrix}$$

$$c_2 = \frac{1}{\Delta}\begin{vmatrix} \sum\frac{1}{\sigma_i^2} & \sum\frac{x_i}{\sigma_i^2} & \sum\frac{x_i^2 y_i}{\sigma_i^2} \\ \sum\frac{x_i}{\sigma_i^2} & \sum\frac{x_i^2}{\sigma_i^2} & \sum\frac{x_i^3 y_i}{\sigma_i^2} \\ \sum\frac{x_i^2}{\sigma_i^2} & \sum\frac{x_i^3}{\sigma_i^2} & \sum\frac{x_i^4 y_i}{\sigma_i^2} \end{vmatrix} \quad , \quad \Delta = \begin{vmatrix} \sum\frac{1}{\sigma_i^2} & \sum\frac{x_i}{\sigma_i^2} & \sum\frac{x_i^2}{\sigma_i^2} \\ \sum\frac{x_i}{\sigma_i^2} & \sum\frac{x_i^2}{\sigma_i^2} & \sum\frac{x_i^3}{\sigma_i^2} \\ \sum\frac{x_i^2}{\sigma_i^2} & \sum\frac{x_i^3}{\sigma_i^2} & \sum\frac{x_i^4}{\sigma_i^2} \end{vmatrix} \tag{4.32}$$

The coefficient uncertainties are found by first determining the *curvature matrix* $\boldsymbol{\alpha}$ given by

$$\boldsymbol{\alpha} = \begin{bmatrix} \sum\frac{1}{\sigma_i^2} & \sum\frac{x_i}{\sigma_i^2} & \sum\frac{x_i^2}{\sigma_i^2} \\ \sum\frac{x_i}{\sigma_i^2} & \sum\frac{x_i^2}{\sigma_i^2} & \sum\frac{x_i^3}{\sigma_i^2} \\ \sum\frac{x_i^2}{\sigma_i^2} & \sum\frac{x_i^3}{\sigma_i^2} & \sum\frac{x_i^4}{\sigma_i^2} \end{bmatrix} \tag{4.33}$$

The inverse matrix $\boldsymbol{\varepsilon} = \boldsymbol{\alpha}^{-1}$ is called the *error matrix* because it contains the information needed to estimate the uncertainties

$$\begin{aligned} \sigma_{c_j}^2 &= \varepsilon_{jj} \\ \sigma_{c_j c_i}^2 &= \varepsilon_{ji} \end{aligned} \tag{4.34}$$

where $\sigma_{c_i c_j}^2$ is the covariance between variables c_i and c_j .The parameters of the fit are given in Table 4.5. The quality of the fit is found by examining the value of the reduced χ^2 :

$\chi_\nu^2 = \chi^2/\nu$

$$\chi_\nu^2 = \frac{1}{N-3}\sum\left[\frac{1}{\sigma_i^2}\left(y_i - c_0 - c_1 x_i - c_2 x_i^2\right)^2\right] \tag{4.35}$$

where ν is the number of degrees of freedom which is given by the number of data points N minus the number of parameters of the distribution determined from those data points. The expected value of χ_ν^2 should be approximately equal to 1. The reduced chi-squared value for the fit is 0.7 indicating that the assigned uncertainties correctly estimate the instrumental uncertainties in the experiment (Group 1998). However, we also observe that the uncertainty σ_{c_2} is larger than the value of the c_2 coefficient. Therefore, a quadratic fit to the data is not warranted, and we can only reasonably fit a straight line to the data.

Table 4.5. Least squares parameters, definitions, and values for a weighted fit to the quadratic function $y = c_0 + c_1 x + c_2 x^2$. The input data is taken from Table 4.3 in the form $(x, y \pm \sigma_i)$ where $y \pm \sigma$ is the integral width including uncertainty, and x is the wire diameter. The fitting of parameters c_0, c_1, and c_2 are weighted by the uncertainty in the integral width.

Parameter	Value	Parameter	Value
N	14	σ_{c_0}	397.981 506 Hz
Δ	1.083384×10^{7} μm^2	σ_{c_1}	0.967 020 Hz-μm^{-1}
χ_ν^2	0.709 932	σ_{c_2}	5.873501×10^{-4} Hz-μm^{-2}
c_0	1818.934 759 Hz	$\sigma^2_{c_0c_1}$	-382.18 Hz^2
c_1	-1.969 097 Hz-μm^{-1}	$\sigma^2_{c_0c_2}$	0.228 327 Hz^2-μm^{-2}
c_2	-8.53217×10^{-5} Hz-μm^{-2}	$\sigma^2_{c_1c_2}$	-5.65238×10^{-4} Hz^2-μm^{-3}

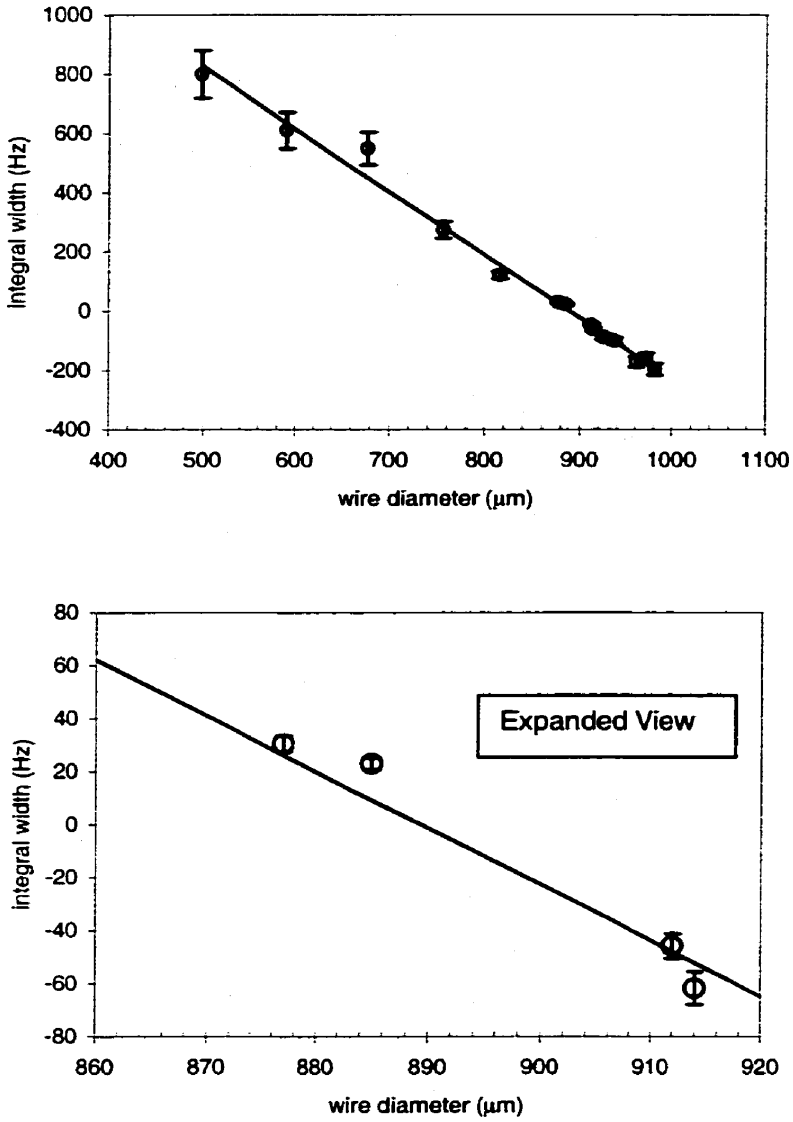

Fig. 4. 29. Data from Table 4.3 plotted with the least-squares fit of Table 4.5.

The equation for the straight line is given by

$$y = c_0 + c_1(x-a) = c_0 + c_1 x' , \quad x' = x - a \tag{4.36}$$

where a is a constant introduced to centre the data points at, or near, the origin to reduce the likelihood of unintended numerical rounding errors. (In this work, the computer program Excel was used for these particular calculations.)

The data can be shifted such that the weighted mean of the x data $\langle x \rangle$ is located approximately at $x \sim 0$. The weighted mean $\langle y \rangle$ is found first, and is given by

$$\langle y \rangle = \frac{\sum_i \frac{y_i}{\sigma_i^2}}{\sum_i \frac{1}{\sigma_i^2}} = -15.44099\,\text{Hz} \tag{4.37}$$

The weighted mean $\langle x \rangle$ can then be determined from $\langle y \rangle = c_0 + c_1 \langle x \rangle$, where c_0 and c_1 are taken from Table 4.5, i.e.

$$\langle x \rangle = \frac{\langle y \rangle - c_0}{c_1} = 896.60592\,\mu\text{m} \tag{4.38}$$

If we arrange for $\langle x \rangle = 0$ by a suitable change of the origin, then we also make the covariance $\sigma^2_{c_0 c_1} \sim 0$ (Lyons 1986). since

$$\sigma^2_{c_0 c_1} \sim -\langle x \rangle . \tag{4.39}$$

We arrange for $\langle x \rangle = 0$ by introducing the substitution $x \rightarrow x' = (x - a)$ where a is given by

$$a \sim \langle x \rangle = 896\,\mu\text{m} \tag{4.40}$$

Input data for the fit are taken from Table 4.3 in the form $(x_i', y_i \pm \sigma_i)$ where $y_i \pm \sigma_i$ is the integral width including uncertainty, and $x_i' = x_i - a$ is the wire diameter with negligible uncertainty minus the constant value *a*.

The determinants used to find the optimum values for the coefficients and the curvature matrix are given by

$$c_0 = \frac{1}{\Delta}\begin{vmatrix} \sum \frac{y_i}{\sigma_i^2} & \sum \frac{x_i'}{\sigma_i^2} \\ \sum \frac{x_i' y_i}{\sigma_i^2} & \sum \frac{x_i'^2}{\sigma_i^2} \end{vmatrix} \quad , \quad c_1 = \frac{1}{\Delta}\begin{vmatrix} \sum \frac{1}{\sigma_i^2} & \sum \frac{x_i' y_i}{\sigma_i^2} \\ \sum \frac{x_i'}{\sigma_i^2} & \sum \frac{x_i'^2 y_i}{\sigma_i^2} \end{vmatrix},$$

$$\Delta = \begin{vmatrix} \sum \frac{1}{\sigma_i^2} & \sum \frac{x_i'}{\sigma_i^2} \\ \sum \frac{x_i'}{\sigma_i^2} & \sum \frac{x_i'^2}{\sigma_i^2} \end{vmatrix} \quad , \quad \alpha = \begin{bmatrix} \sum \frac{1}{\sigma_i^2} & \sum \frac{x_i'}{\sigma_i^2} \\ \sum \frac{x_i'}{\sigma_i^2} & \sum \frac{x_i'^2}{\sigma_i^2} \end{bmatrix}. \qquad (4.41)$$

The parameters of the fit are given in Table 4. 6. The quality of the fit is found by examining the value of the reduced χ^2 : $\chi_\nu^2 = \chi^2/\nu$

$$\chi_\nu^2 = \frac{1}{N-3}\sum\left[\frac{1}{\sigma_i^2}\left(y_i - c_0 - c_1(x_i - a)\right)^2\right] \qquad (4.42)$$

The reduced chi-squared value for the fit is 0.7 indicating that the assigned uncertainties correctly estimate the instrumental uncertainties in the experiment.

Table 4. 6. Least squares parameters, definitions, and values for a weighted fit to the linear function $y = c_0 + c_1(x - a)$. The input data is taken from Table 4.3 in the form $(x_i - a, y_i \pm \sigma_i)$ where $y_i \pm \sigma_i$ is the integral width including uncertainty, and x_i is the wire diameter. The fitting of parameters c_0 and c_1, are weighted by the uncertainty in the integral width.

Parameter	Value (a=896μm)
N	14
Δ	3.747 455 μm^2
χ^2_ν	0.711 850
c_0	-14.163 151 Hz
c_1	-2.108 893 Hz-μm^{-1}
σ_{c_0}	5.803 882 Hz
σ_{c_1}	0.130 910 Hz-μm^{-1}
$\sigma^2_{c_0c_1}$	-0.185 150 Hz^2

The zero-crossing on the x-axis is obtained by setting $y = 0$ in Eq. (4.36) and solving for x:

$$x'(y=0) = x'_c = \frac{-c_0}{c_1} = x_c - a$$
$$\therefore x_c = \frac{-c_0}{c_1} + a \tag{4.43}$$

Using the coefficients in Table 4. 6, we found the zero crossing to be x_c = 889.28 μm. The uncertainty Δx_c is given by

$$\Delta x_c^2 = \left(\frac{\partial x_c}{\partial c_0}\right)^2 \sigma_{c_0}^2 + \left(\frac{\partial x_c}{\partial c_1}\right)^2 \sigma_{c_1}^2 + 2\left(\frac{\partial x_c}{\partial c_0}\right)\left(\frac{\partial x_c}{\partial c_1}\right)\sigma^2_{c_0c_1}$$
$$= \left(\frac{1}{c_1}\right)^2 \sigma_{c_0}^2 + \left(\frac{x}{c_1}\right)^2 \sigma_{c_1}^2 + 2\left(\frac{-1}{c_1}\right)\left(\frac{c_0}{c_1^2}\right)\sigma^2_{c_0c_1} \tag{4.44}$$

Thus, using the coefficients in Table 4. 6 we found Δx_c = 2.831 684 μm. The value of the zero-crossing is therefore x_c = 889 ± 3 μm. This value is in good agreement with the theoretically predicted value of 888 ± 2 μm (starting aluminium wire diameter of 500 μm).

4.4.2.3 Half-Loop RF coil

The applicability of the straight wire model was investigated for a non-straight wire RF coil geometry by simply repositioning the water-filled capillary to lie inside the half-loop of the RF coil as shown in Fig. 4.30.

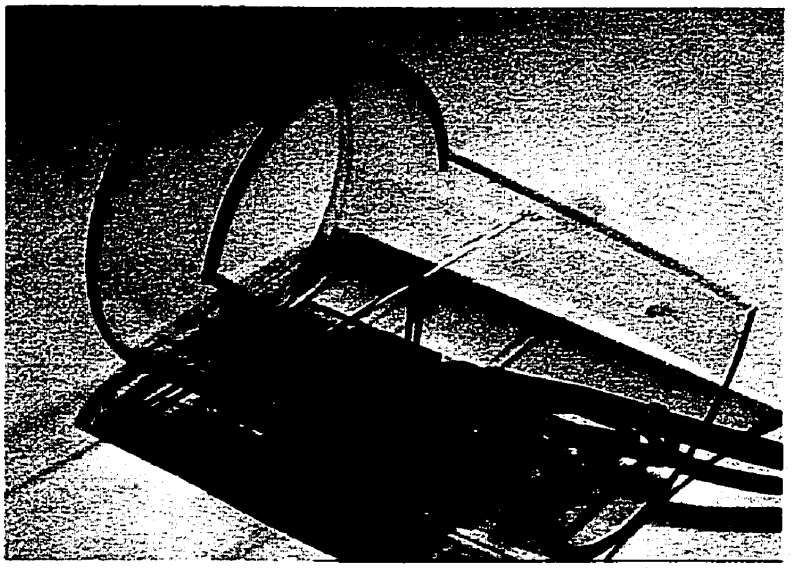

Fig. 4.30. Photograph showing the placement of the wire under test in the "half-loop" position.

One of the copper-plated wires used in previous experiments (diameter: 885 μm) was installed in the probe as described and then positioned at the iso-centre of the magnet. We then shimmed to the narrowest linewidth using only x, y, and z shims and obtaining a minimum peak width of 20 Hz (FWHM). The spectrum is shown in Fig. 4.31. For comparison, spectra corresponding to RF coils made of pure copper and pure aluminium wires (diameter 1mm) are also included in Fig. 4.31. The copper and aluminium spectra are

insensitive to changes in the shim settings due to the large static inhomogeneity of the materials used. The FWHM of the spectrum corresponding to the RF coil made of pure copper wire is 1140Hz and for the aluminium wire, 2280Hz. If we scale these results to a wire diameter of 885μm (i.e. FWHM $\times^{885}/_{1000}$), then the equivalent FWHM of the spectrum corresponding to the pure copper wire coil would be 1010Hz. Comparing copper and copper-plated-aluminium results, we therefore estimate a susceptibility reduction in the copper-aluminium wire of 250 over that of pure copper (or less than 0.5% the susceptibility of copper).

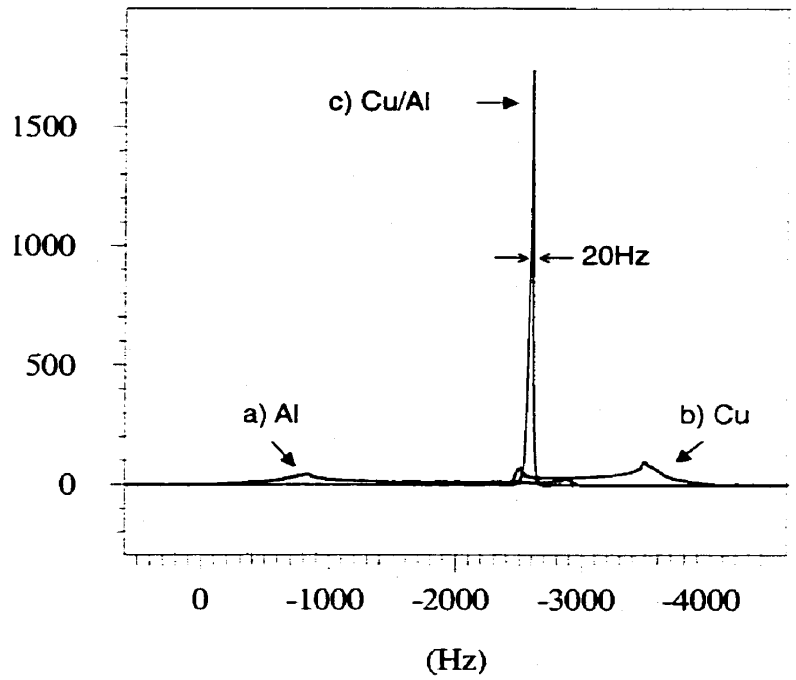

Fig. 4.31. Water spectra at 400MHz from the probe of Fig. 4.30 (i.e. "half-loop" position). (a) The RF coil is made from 1mm diameter, 99.999% pure aluminium wire; (b) 1mm diameter, 99.999% pure copper wire; (c) 885μm diameter copper plated aluminium wire (starting aluminium diameter 500μm).

4.5 Chapter Summary

We have indicated the need for zero magnetic susceptibility wire in the construction of small NMR microprobes. Desirable wire characteristics such as conductivity, ductility, surface finish, diffusion, and temperature dependence for a diamagnetic and paramagnetic metal-pair were discussed. A simple magnetostatic field model was used to predict the correct dimensions for a zero susceptibility co-axial wire combination. We then described in detail how to plate copper on high purity aluminium wire for zero susceptibility in wire sizes that are appropriate for building NMR microcoils. Copper-plated aluminium wires were then assessed for ductility and susceptibility. The theoretically predicted dimensions for zero susceptibility wire were verified in the specific instance of copper plating on a 500 μm diameter of pure aluminium wire.

The simple NMR probe and one-pulse NMR experiment used here may also be applicable to general susceptibility testing of other wire samples of off-the-shelf materials. e.g. ordinary copper wire or suspected/claimed zero susceptibility wire alloys. However, it is unfortunate that in spite of the apparent accuracy in experimentally determining the correct zero susceptibility thickness for copper-aluminium, the associated precision is poor. This affects reproducible susceptibility results from wire to wire in the manufacturing process.

On a positive note, we have shown the gains achievable by using zero susceptibility wire as indicated by the results from our special NMR test probe. Clearly zero susceptibility wire can be made, and to date we have reduced the susceptibility of a copper-aluminium wire to less that 0.5% that of pure copper wire.

Chapter 5

PROBE DESIGN 3. A SOLENOID WINDING

5.1 Introduction

A solenoid winding used as the RF coil in a NMR probe is often the best choice for a practical field measurement probe. This coil gives good signal-to-noise and is relatively simple to construct. The greatest signal-to-noise ratio is obtained when the coil is wound directly on the sample vessel. However, coil-induced magnetic field perturbations almost always then result in significant spectral linewidth broadening and thus poor measurement resolution. This chapter therefore describes the construction of two solenoid RF coils. The first coil is made of ordinary copper wire and the second is made of zero-susceptibility wire. The solenoids were installed in the special NMR probe discussed in Chapter 4 and NMR spectra acquired, analyzed, and compared with spectra predicted from a simplistic theory.

5.2 Theory

5.2.1 Magnetostatic description of the field perturbation due to the RF coil

In principle, we could solve the magnetostatic problem of a permeable solenoid in a uniform field using Laplace's equation in an appropriate coordinate system and apply boundary conditions, as was done for the straight wire in Chapter 4. However, there is not a coordinate system in which a solenoidal geometry becomes particularly simple. A full computer simulation using numerical techniques would have required a very powerful and expensive computer-aided engineering package (e.g. "Amperes 3D" magnetostatic field

modeling software, Manufacturer: Integrated Engineering Software, Winnipeg, Canada, Cost: 12,900 USD) Thus, we considered simpler approaches.

5.2.1.1 Laplace's equation in Toroidal Coordinates for a permeable ring of material

The first is a geometric simplification of the solenoid to multiple permeable closed loops or rings. A suitable coordinate system does exist for this geometry, called the toroidal coordinate system (Moon and Spencer 1971) as shown in Fig. 5.1.

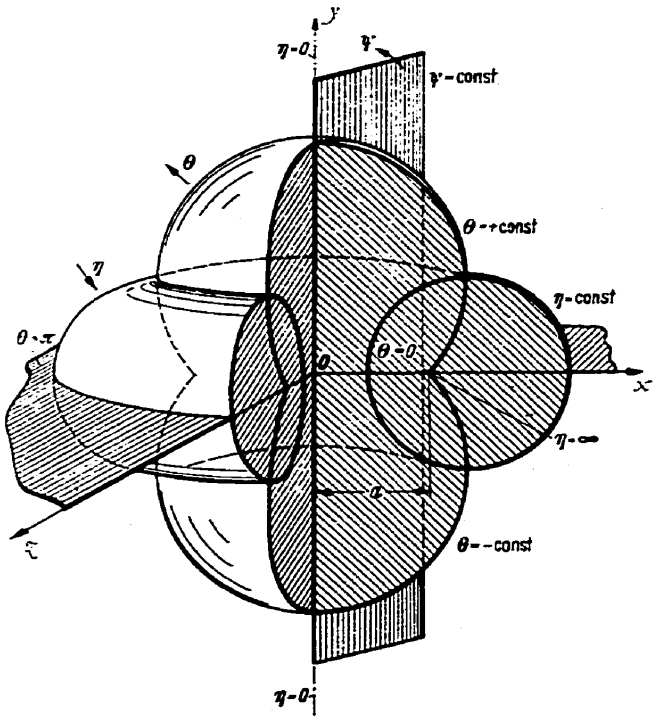

Fig. 5.1. Toroidal coordinates (η,θ,ψ). [Moon, 1971 #418]Coordinate surfaces are toroids (η = constant), spherical bowls (θ = constant), and half-planes (ψ = constant).

Laplace's equation is not "simply separable" in toroidal coordinates, but can be made "R-separable" with appropriate substitutions as described in references (Morse and Feshbach 1953; Moon and Spencer 1971). Thus, Laplace's equation and its series solution in toroidal coordinates are given as (Morse and Feshbach 1953)

$$\nabla^2\Phi_M(\eta,\theta,\varphi)=\frac{(\cosh\eta-\cos\theta)^3}{a^2\sinh\eta}\left\{\frac{\partial}{\partial\eta}\left(\frac{\sinh\eta}{\cosh\eta-\cos\theta}\frac{\partial\Phi_M}{\partial\eta}\right)+\sinh\eta\frac{\partial}{\partial\theta}\left(\frac{1}{\cosh\eta-\cos\theta}\frac{\partial\Phi_M}{\partial\theta}\right)\right\}+\frac{(\cosh\eta-\cos\theta)^2}{a^2\sinh^2\eta}\frac{\partial^2\Phi_M}{\partial\varphi^2} \tag{5.1}$$

$$\Phi_M(\eta,\theta,\varphi)=\sqrt{\cosh\eta-\cos\theta}\cdot\sum_{m=0}^{\infty}\sum_{n=0}^{\infty}a_m\cos(m\varphi)\cdot c_n\cos(n\theta)\cdot\left[A_{mn}P^m_{n-\frac{1}{2}}(\cosh\eta)+B_{mn}Q^m_{n-\frac{1}{2}}(\cosh\eta)\right] \tag{5.2}$$

where the $P^m_{n-\frac{1}{2}}(\cosh\eta)$ and $Q^m_{n-\frac{1}{2}}(\cosh\eta)$ are toroidal harmonics (described in references (Morse and Feshbach 1953; Abramowitz and Stegun 1964)). Unfortunately, at the time of writing, despite several months' effort, the complete analytical solution (with coefficients evaluated from boundary conditions) has not been obtained.

5.2.1.2 Laplace's equation in spherical coordinates for a permeable ring of material

The ring problem was also considered by examining the perturbing effect on an initially homogenous field B_0 at a field point $P(r,\theta,\phi)$ due to an elementary volume dV of permeable material of susceptibility χ at position $Q(r',\theta',\phi')$ as (Chen and Hoult 1989)

$$dB_z(\mathbf{r},\mathbf{r}')=\frac{\chi B_0 dV}{4\pi}\sum_{n=0}^{\infty}\sum_{m=0}^{n}\left[\varepsilon_m\frac{(n-m+2)!}{(n+m)!}\times\left(\frac{1}{r'^{n+3}}P_{n+2,m}(\cos\theta')\cos m(\phi-\phi')\right)r^nP_{nm}(\cos\theta)\right] \tag{5.3}$$

where ε_m is called the Neumann factor, $\varepsilon_0=1$, $\varepsilon_{m\neq0}=2$, and $P_{n,m}$ is Ferrer's associated Legendre polynomial. (In NMR usage, integer n is usually termed the order of the polynomial, m the degree) We therefore considered the field at the origin from a ring whose plane is parallel to the xz plane and whose axis is the y-axis, where the ring is built up of elementary volumes.

The geometry of this problem is shown in Fig. 5. 2. With the ring's centre at $(0, y_0, 0)$ a plane of rotation, initially coincident with the xy plane, is rotated in a negative sense about the y-axis by an angle $d\gamma$. It intersects the ring in a disc whose centre O'' is at a radial distance σ_0 from the y-axis. The disc has two primary axes: the w-axis, coincident with the radial direction σ from the y-axis to O'', and an axis y'' parallel to the y-axis. A point of interest Q in the disc, relative to the disc's centre, is at (ρ, β) where ρ is the radial distance from the centre point O'' and β is the angle relative to the y''-axis.

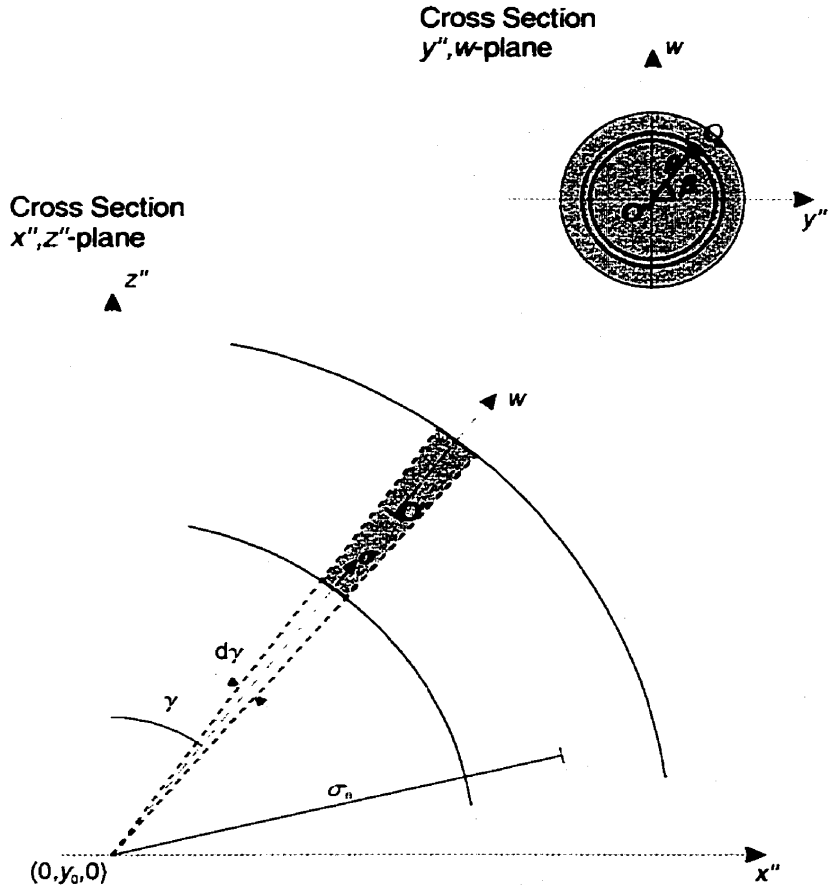

Fig. 5. 2. Two cross sections based on the ring in Fig. 5.1 with the centre of the ring at a position y_0 along the along the y-axis.

We can now define the size and location of an elementary volume at point Q. The width of the disc at declination γ varies as $\sigma\, d\gamma$. Within the disc, the elementary area at radius ρ is $dA = \rho\, d\beta\, d\rho$ at angle β. Thus the elementary volume in terms of ρ, σ is

$$dV = \rho\, d\beta\, d\rho\, \sigma\, d\gamma \tag{5.4}$$

Now $\sigma = \sigma_0 + \rho \sin\beta$. Therefore in terms of ρ, σ_0, and β,

$$dV = \rho\, d\beta\, d\rho (\sigma_0 + \rho \sin\beta)\, d\gamma \tag{5.5}$$

The coordinates of our elementary volume at point Q in terms of x'', y'', and z'' are

$$\begin{aligned} x'' &= \sigma \sin\gamma = (\sigma_0 + \rho \sin\beta)\sin\gamma \\ y'' &= \rho \cos\beta \\ z'' &= \sigma \cos\gamma = (\sigma_0 + \rho \sin\beta)\cos\gamma \end{aligned} \tag{5.6}$$

The double primed coordinate system and the unprimed coordinate system are related by a translation in the y-axis direction by an amount y_0. Therefore

$$\begin{aligned} x &= x'' \\ y &= y'' + y_0 = \rho \cos\beta + y_0 \\ z &= z'' \end{aligned} \tag{5.7}$$

The elementary volume Q may also be partially located in spherical harmonic coordinates in terms of its distance r' from the origin O of the unprimed coordinate system $\mathbf{O} = (x, y, z) = (0, 0, 0)$ and the cosine of the declination to the z-axis

$$\begin{aligned} r' &= \left[(\sigma_0 + \rho \sin\beta)^2 \sin^2\gamma + (y_0 + \rho \cos\beta)^2 + (\sigma_0 + \rho \sin\beta)^2 \cos^2\gamma \right]^{1/2} \\ &= \left[y_0^2 + \rho^2 + \sigma_0^2 + 2\rho\, y_0 \cos\beta + 2\rho\, \sigma_0 \sin\beta \right]^{1/2} \end{aligned} \tag{5.8}$$

and

$$\cos\theta' = \frac{z}{r'}. \tag{5.9}$$

where, for our purposes, we have ignored the azimuth ϕ'.

We now return to our expression for the field perturbation dB_z, Eq. (5.3), due to the presence of the elementary volume dV. If we consider only $n = 0$ in Eq. (5.3), the field at the origin O involves only one term in r' and $\cos\theta'$

$$dB_{z,n=0}(\mathbf{O},(r',\theta')) = \frac{\chi B_0 dV}{4\pi} 2\times\left(\frac{1}{r'^3}P_{2,0}(\cos\theta')\right)$$
$$= \frac{\chi B_0 dV}{2\pi}\frac{1}{r'^3}\left(3\cos^2\theta'-1\right)$$
$$dB_{z,n=0}(\mathbf{O},(\beta,\gamma,\rho)) = \frac{\chi B_0 \rho\, d\beta\, d\rho(\sigma_0+\rho\sin\beta)d\gamma}{2\pi\left[y_0^2+\rho^2+\sigma_0^2+2\rho\, y_0\cos\beta+2\rho\sigma_0\sin\beta\right]^{3/2}}\times \tag{5.10}$$
$$\left(3(\sigma_0+\rho\sin\beta)^2\frac{\cos^2\gamma}{y_0^2+\rho^2+\sigma_0^2+2\rho\, y_0\cos\beta+2\rho\sigma_0\sin\beta}-1\right)$$

where $P_{2,0}(\cos\theta') = 3\cos^2\theta'-1$. Direct integration of dB_z would be difficult. Rather, we expand $dB_{z,n=0}$ as a power series in ρ to fifth order.

$$dB_{z,n=0}(\mathbf{O},(\beta,\gamma,\rho)) = \sum_{i=0}^{5} c_i(\beta,\gamma)\rho^i \tag{5.11}$$

The resulting coefficients' solutions are not given explicitly here since they are quite lengthy and would not conveniently fit in this document. In practice, the coefficients were determined by a calculation in Mathematica. We now integrate the coefficients in the angles β and γ

$$d_i = \int_{\gamma=0}^{2\pi}\int_{\beta=0}^{2\pi} c_i(\beta,\gamma)\,d\beta d\gamma, \qquad i=1,\ldots,5 \tag{5.12}$$

where

$$
\begin{aligned}
d_0 &= d_2 = d_4 = 0 \\
d_1 &= \frac{\pi B_0 \chi \sigma_0 \left(\sigma_0^2 - 2y_0^2\right)}{2\left(\sigma_0^2 + y_0^2\right)^{5/2}} \\
d_3 &= -\frac{3\pi B_0 \chi \sigma_0 \left(\sigma_0^2 - 4y_0^2\right)}{8\left(\sigma_0^2 + y_0^2\right)^{7/2}} \\
d_5 &= -\frac{15\pi B_0 \chi \sigma_0 \left(\sigma_0^2 - 6y_0^2\right)}{128\left(\sigma_0^2 + y_0^2\right)^{9/2}}
\end{aligned}
\tag{5.13}
$$

Finally, for "zero-susceptibility wire", integration over ρ is carried out in two parts: $0 < \rho \le a$ and $a < \rho \le b$ where the outer dimension of b is given by Eq. (4.3)

$$
\begin{aligned}
e_i &= d_i(\chi_1) \int_{\rho=0}^{a} \rho^i d\rho + d_i(\chi_2) \int_{\rho=a}^{b} \rho^i d\rho \,, \qquad b = a\sqrt{\frac{\chi_2 - \chi_1}{\chi_2}} \\
B_z(\mathbf{O}) &= \sum_i e_i
\end{aligned}
\tag{5.14}
$$

where the coefficients e_i are given by

$$
\begin{aligned}
e_1 &= e_2 = e_4 = 0 \\
e_3 &= \frac{3\pi B_0 \chi_1 \sigma_0 a^4 (\chi_2 - \chi_1)\left(\sigma_0^2 - 4y_0^2\right)}{32\chi_2\left(\sigma_0^2 + y_0^2\right)^{7/2}} \\
e_5 &= \frac{5\pi B_0 \chi_1 \sigma_0 a^6 \left(\chi_1^2 - 3\chi_1\chi_2 + 2\chi_2^2\right)\left(\sigma_0^2 - 6y_0^2\right)}{256\chi_2^2\left(\sigma_0^2 + y_0^2\right)^{9/2}}
\end{aligned}
\tag{5.15}
$$

Recall the value for b in Eq. (5.14) was the result from Chapter 4 where we had an infinitely long co-axial wire perpendicular to B_0. There we saw that all perturbations vanished for that wire configuration and orientation for all field points external to the wire. In contrast, we see that for the ring, perturbations do not vanish at the origin for the elementary case of $n = 0$ of Eq. (5.3), for e_3, e_5, ... are not zero. In contrast to popular belief (Doty 1996; Hill 1996) it is

evident that the co-axial wire that worked so well in Chapter 4 for the perpendicular-wire probe is, in principle, unsuitable as a zero-susceptibility wire for the solenoid winding.

The effect on the field due to an error in wire dimension b, e.g. a plating error, can be estimated by re-examining the e_1 coefficient in Eq. (5.15). Let us introduce an error in the outer dimension of the co-axial of $b \rightarrow b + \delta b$. Consider the effect of this error in the integral evaluation in Eq. (5.14) for the coefficient e_1 :

$$\begin{aligned} e_1' &= d_1(\chi_1)\int_0^a \rho\, d\rho + d_1(\chi_2)\int_a^{b+\delta b} \rho\, d\rho \\ &= 0 + \frac{\pi B_0 \sigma_0 \left(\sigma_0^2 - 2y_0^2\right)}{2\left(\sigma_0^2 + y_0^2\right)^{5/2}} a\sqrt{\chi_2(\chi_2 - \chi_1)}\,\delta b, \quad b = a\sqrt{\frac{(\chi_2 - \chi_1)}{\chi_2}} \end{aligned} \tag{5.16}$$

$$i.e.\ \ \delta e_1 = \frac{\pi B_0 \sigma_0 \left(\sigma_0^2 - 2y_0^2\right)}{2\left(\sigma_0^2 + y_0^2\right)^{5/2}} a\sqrt{\chi_2(\chi_2 - \chi_1)}\,\delta b$$

The value of the coefficients for δe_1, e_3 and e_5 in two worked examples are presented in Fig. 5.3. Of course, these coefficients are only crude indicators of the final homogeneity and higher order and degrees in the expansion of Eq. (5.3) should be calculated. However, the labour involved is very great. Further, the results of Eq. (5.15) and (5.16) suggest that deformation of the wire when it is wound into a solenoidal form will have further detrimental effects on the homogeneity.

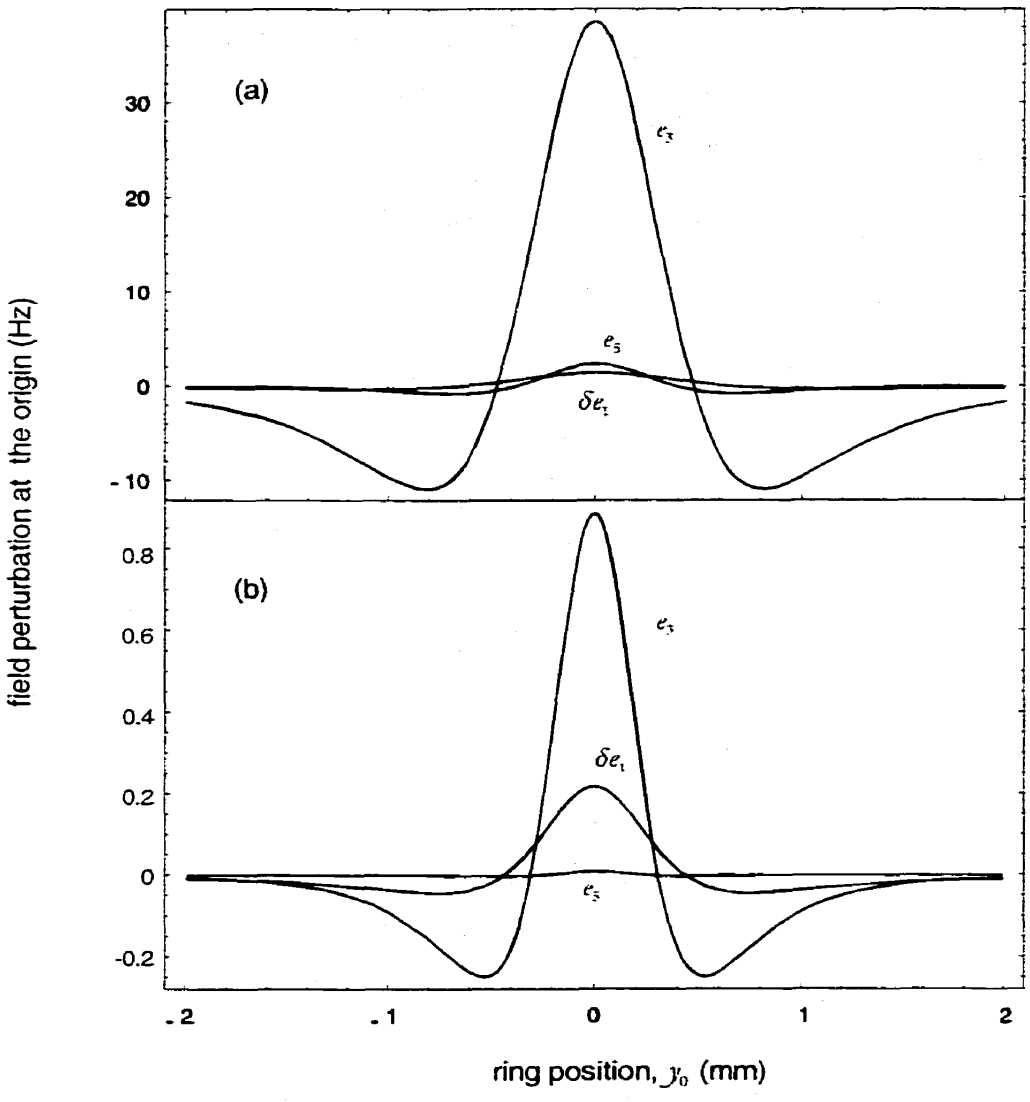

Fig. 5.3. Coefficients from Eq. (5.15) and Eq. (5.16) of the perturbation in a 9.4 T field at the origin due to (a) thick ring of "zero-susceptibility" co-axial wire and (b) a thin ring of "zero-susceptibility" co-axial wire (refer Fig. 5. 2) at $y = y_0$. In both cases, the inner diameter of the ring is 1mm (for a capillary tube OD=1mm) and $\delta b = 1\% b$. In example (a), the coaxial wire is made of an aluminium wire core of diameter 500 μm with an outer layer of copper to give a final diameter of 888 μm. In example (b), the coaxial wire is made of an aluminium wire core of diameter 127 μm with an outer layer of copper to give a final diameter of 226 μm. By way of comparison, if we consider a copper wire of diameter 888 μm, the perturbing field it produces at the origin is 600 Hz when $y_0 = 0$. A copper wire of diameter 226 μm produces a perturbing field at the origin of -100 Hz at the same y_0=0.

5.2.2 B_1

The magnet field (B_1) produced by passing current through a short solenoid has been described in several standard electricity and magnetism texts. The important point here was that the B_1 field was predominantly in the direction of the axis of symmetry of the solenoid. In practice, the solenoid was positioned with its axis of symmetry perpendicular to the direction of the $\mathbf{B}_0$ field so that B_1 field was perpendicular to $\mathbf{B}_0$.

5.3 Microprobe construction

We wound two 4-turn solenoids with an inner diameter of 1mm; one using zero-susceptibility copper-plated aluminium (Cu/Al) wire, and the other pure copper wire. Inter-turn spacing was approximately $3r$ as shown in Fig. 5.4 in order to obtain optimum signal-to-noise (Hoult and Lauterbur 1979).

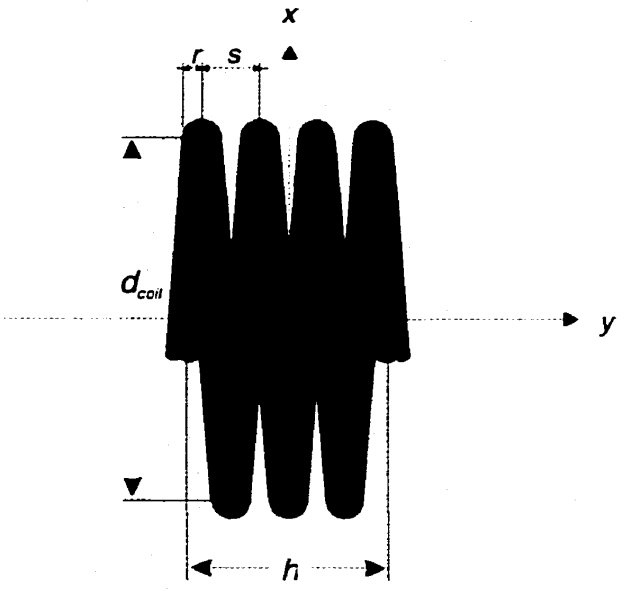

Fig. 5.4. Winding geometry for a solenoidal coil. For optimal signal-to-noise the inter-wire spacing s should be $3r$, and height h should be equal to $0.8d_{coil}$ (Chen and Hoult 1989).

The Cu/Al wire was obtained by plating copper on pure aluminium wire using the method described in Chapter 4. Using a starting aluminium diameter of 127μm, the predicted

final diameter for zero magnetic susceptibility (refer Eq. 4.3) and uncertainty (refer Eq. 4.6) was 225.6 ± 1.8μm. Sources of error include uncertainties in the susceptibilities of aluminium and copper, and the precision related to the measurement micrometer. If we consider a susceptibility reduction to 1% that of pure copper as predicted by Eq. (4.6), the final diameter must be 225.6 ± 1.2μm. Thus, we see that the best possible susceptibility reduction is on the order of a few percent. Experimentally, the measured final diameter of the plated wire was 225 ± 2 μm. The overall length of the coil was 1.24mm.

A second four-turn coil using pure copper wire (99.9985%) with a diameter of 220μm (Manufacturer: Califomia Fine Wire, Grover Beach, CA) with nearly the same spacing was made in order to perform a linewidth comparison to the zero susceptibility coil. The overall length of the copper coil after winding was 1.27mm.

Each coil was successively mounted in the special NMR probe as shown in Fig. 5.5, with minor changes to the values of capacitors used for tuning and matching. The tuning and matching circuit of Fig. 2.1 was used to obtain a good 50 Ω match at 400MHz, corresponding to the Larmor frequency for protons.

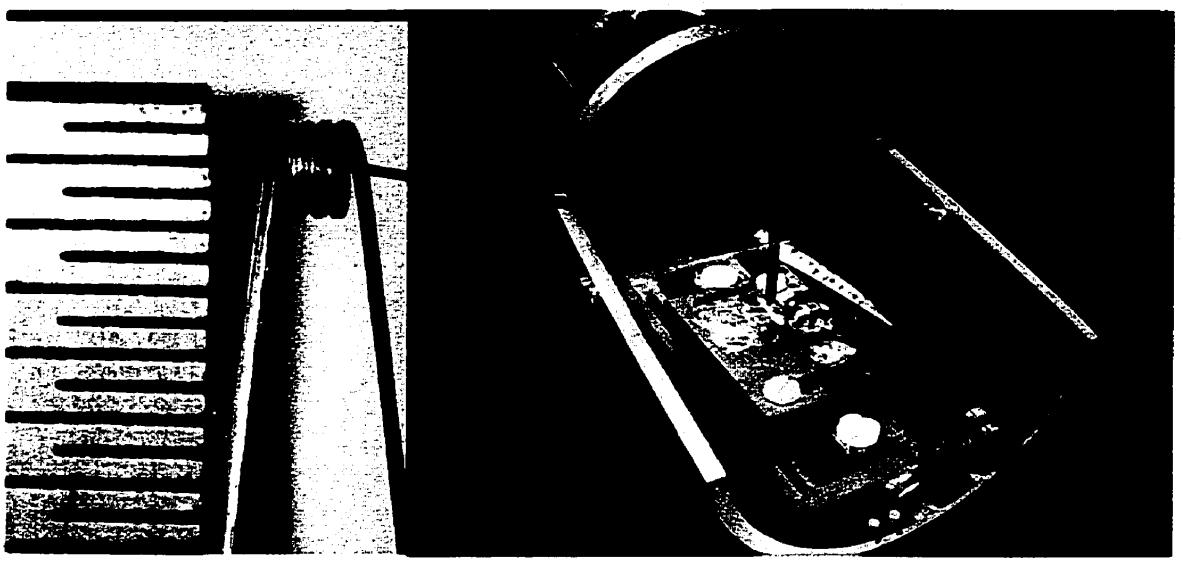

Fig. 5.5. Installation of the 4-turn solenoid into the special NMR probe. The hairpin loop of the special NMR probe is removed and the 4-turn solenoid is installed with the loop surrounding the 1mm O.D. water-filled capillary tube. The rule on the left is marked in 0.5mm increments. The wire in the photograph on the left is copper plated aluminium.

5.4 NMR experiments

5.4.1 Spectrometer set-up

The experiments were performed on the 9.4T 21cm horizontal bore magnet described earlier. The probe was placed at the iso-centre of the magnet and an FID acquired from a single pulse experiment.

The single pulse experiments were carried out in a similar manner to that described in Chapters 3 and 4. The frequency bandwidth was unchanged at 50,000Hz but the flip angle was increased from 10° to 90°. This was verified by fixing transmitter power and slowly increasing the pulse duration while observing the effect on the free induction decay. The NMR signal is a maximum for a 90° flip angle, which would normally be the flip angle used in a practical field mapping exercise. The transmit pulse power and duration were 300mW and 12μs respectively. Thus, the associated frequency bandwidth for this pulse width was approximately 80kHz. In

the signal receive chain, the delays and filter settings were unchanged from the description given in Chapters 3 and 4. All transmit and receive parameters were the same for each solenoid coil test.

The magnetic field was shimmed in for each coil to give the narrowest linewidth using only the x, y, and z shims, i.e. only 3 of 14 shim windings were used to obtain a uniform field in the NMR sample volume. Each linear shim winding was adjusted in turn to obtain a maximum in the area in the free induction decay envelope (a method described in Section 3.4.4). The linear shims were adjusted until no further increase in free induction decay area was observed. The free induction decay was then Fourier transformed to obtain the spectral line shape.

5.4.2 Results and Discussion. Overview of Results

The Fourier transform of the free decay induction decays are shown in Fig. 5.6 and linewidths are tabulated in Table 5.1.

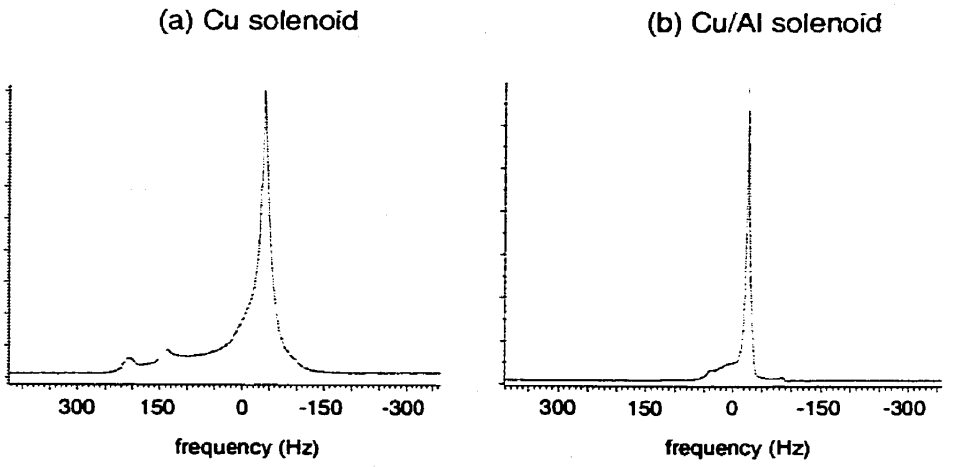

Fig. 5.6. Four-turn solenoid coil results. Experimentally observed NMR spectrum from the 4-turn solenoid coils using (a) copper wire to wind the solenoid, and (b) copper plated aluminium zero susceptibility wire.

Table 5.1. Experimental results. Observed NMR line shape widths from solenoid coils built with copper and copper-plated aluminium wire in a 9.4T magnet.

	Cu solenoid	Cu/Al solenoid
Observed width at 10% of maximum peak height.	213 Hz	21 Hz
Observed width at 50% of maximum peak height.	20 Hz	5.6 Hz

5.4.3 Specific Results

Copper Solenoid

The experimentally-observed line shape Fig. 5.6(a) consists of a tall relatively narrow peak with smaller peaks at a higher frequency (i.e. higher magnetic field). The large dominant peak indicates that a large portion of the NMR signal was acquired from regions in the sample where the field was relatively homogeneous. This would likely be about the origin, in the middle of the solenoid. The two minor peaks may tentatively be associated with homogenous fields at a large distance from the solenoid and at the minima in Fig. 5.3. The spectral signal-to-noise of the peak obtained with the copper wire solenoid was 250. Signal-to-noise was not optimized by application of a filter nor by adjustment of coil parameters such as lead lengths, etc..

Copper-Aluminium Solenoid

The observed line shape consists of a large narrow peak with a shoulder on the higher frequency (higher magnetic field) side. This is similar to the observed line shapes in the single perpendicular wire RF coil experiments of Chapter 4 (refer Fig.4.25). As observed in Fig. 4.25, features in the line shape due to static field inhomogeneity are shifted in frequency as the susceptibility of the wire changes. When the wire is close to zero susceptibility, the line shape

component(s) due to field inhomogeneity begin to overlap the peak due to unperturbed static field. Therefore, in the present case when the wire used to build the solenoid is near, but not equal, to zero susceptibility the peak width at 50% of half maximum can be larger than the extremes of significantly non-zero susceptibility wire and identically zero susceptibility wire.

The unfiltered spectral signal-to-noise obtained with the Cu/Al wire solenoid was 5660. This performance exceeds our goal in Chapter 1 of a spectral signal-to-noise of 1000.

Comparison between Copper and Copper-Aluminium Solenoid Results

The asymmetry observed in the copper/aluminium spectrum is similar to the asymmetry observed in the copper solenoid spectrum. This indicates that the "zero-susceptibility" wire of Chapter 4 (i.e. the long straight wire case), appears to take on a diamagnetic nature when it is used to form a solenoid winding.

At 50% of maximum peak height, the peak width associated with the copper solenoid is 3.5 times greater than the peak width associated with the Cu/Al wire solenoid. At 10% of maximum peak height, the copper solenoid peak width is 10 times greater. Not surprisingly, the experimental results do not reflect the susceptibility cancellation based on the precision of the final plated diameter of the Cu/Al wire used here, i.e. 225±2μm, as in the case of a long straight wire perpendicular to the static $\mathbf{B}_0$ field. A plating uncertainty of 2μm is equivalent to a susceptibility of $\leq 2.5\%$ of the susceptibility of pure copper wire (using Eq.(4.3)) in the perpendicular long wire model. However, the peak widths at 50% and 10% indicate an equivalent susceptibility cancellation somewhere in the range of 10-30% of the susceptibility of pure copper wire. This difference between the expected and observed peak width reductions likely reflects the predicted shortcomings of co-axial wire to perform well in a solenoid coil

winding plus the effects of deformation. This can only be confirmed after a better theoretical understanding of the perturbations in the field when using co-axial wire is obtained.

Comparing the signal-to-noise between pure Cu and Cu/Al wire solenoids, the signal-to-noise improves by a factor of 22. Roughly speaking, one would expect the signal-to-noise to scale inversely with the linewidth performance of the two solenoids. That is, a ten-fold reduction in the linewidth should imply a 10-fold increase in signal-to-noise. By this rule-of-thumb, we appear to gain more signal-to-noise than warranted by observing the lineshapes in Fig. 5.6. However, a linewidth and SNR comparison is valid only when the lineshapes are identical, which is not strictly the case here. As far as possible, the parameters for the pure copper wire solenoid experiment and the copper/aluminium wire solenoid experiments were similar except for changes in receiver gain, and magnetic field shimming. Perhaps coincidently, the inverse of the improvement in signal-to-noise is approximately equal to the predicted susceptibility cancellation in the perpendicular long straight wire model, i.e. $1/22 = 4.5\%$ This value is roughly in line with the expected susceptibility cancellation of $0 \pm 2.5\%$ when using data from the perpendicular long straight wire model.

5.5 Chapter summary

The solenoid RF coil made of co-axial zero susceptibility wire was examined in this chapter to determine its suitability for use in a NMR-based microprobe for magnetic field measurements. This coil design is associated with good signal-to-noise and experimental results showed that high signal-to-noise in the spectral line shape is possible. However, co-axial zero-susceptibility wire was found not to be a suitable material to eliminate the well-known disadvantage with the solenoid design of susceptibility-induced line broadening.

The nature of susceptibility-induced line broadening, was investigated by an analytical approach to determine how the solenoid perturbs the static magnetic field. A solution of the magnetostatic equations for the solenoid shape was difficult. In its place, the simpler problem of a toroid or ring in a uniform field was studied. However, the solution of Laplace's equation in toroidal coordinates and applying the appropriate boundary conditions proved difficult as well. As an alternative, dividing the ring into elementary volumes and then using standard spherical harmonic techniques was successful, to a limited extent, in determining the perturbation in the field along the central axis of the ring. Of course deformations in the wire during the coil-forming process have been judiciously ignored!

Line shape comparisons between the experimental copper wire solenoid results and the experimental co-axial susceptibility-reduced wire solenoid results indicate that the copper plated aluminium wire had an effective susceptibility somewhere in the range of 10-30% of the susceptibility of copper. It is obvious that the next research effort should be toward the production of zero susceptibility wire by an alloy technique, or its like, where the alloy is formed of a suitable combination of diamagnetic and paramagnetic metals, e.g. copper doped with platinum.

In conclusion, based on the experiments performed here, it was found that the solenoid RF coil design is a suitable design to achieve a spectral signal-to-noise of greater than 1000. However, the goal of obtaining a line width of less than 1Hz at half of peak maximum was not achieved.

Chapter 6

CONCLUSION

We have shown that NMR-based microprobes are well suited to high precision measurement of magnetic fields. This suitability is based on four important criteria: small sample volume, narrow spectral linewidth of less than 1Hz on a 400 MHz spectrometer (i.e. <2.5 ppb), signal-to-noise performance better than 1000:1, and a favourable size-scaling in order to miniaturize the probe dimensions for operation in inhomogeneous fields.

It was shown in Chapter 1 that in order to make high precision measurements in an inhomogeneous field, the NMR sample must necessarily be small. For example, if the precision of the measurement is 1Hz at the base of the spectral line shape, we showed that in a 9.4T field with an average inhomogeneity gradient of 10 parts per million/10cm, the active measurement volume (sample volume) of the probe must be less than 25μm in the direction of the field inhomogeneiety. Since this small volume was impractical as a starting size for development work, a 1mm sample volume was chosen. In order to retain the 1Hz frequency resolution (at 9.4T) in the spectral line shape, the average field inhomogeneity must not exceed 0.25 parts per million/10cm or 2.5 parts per billion/1mm. (A linear gradient is assumed.)

Static magnetic field gradients were assumed to arise from two independent sources: one, the global inhomogeneity due to the magnet, and two, the local inhomogeneity due to the presence of the probe in the strong magnetic field. The global inhomogeneity due to the magnet was studied and characterized in a spherical harmonic description in Chapter 1 and then annulled by the adjustment of room temperature shims as demonstrated in Chapter 3.

The local inhomogeneity due to the presence of the probe was studied in detail in Chapters 3-5.

The probe designs of Chapters 3-5 all originated, essentially, as part of a study on the performance of the solenoid coil winding as a suitable coil design for magnetic field measurements. As an aid to understand the magnetostatic behaviour of a solenoid, the solenoid was theoretically "deconstructed" into straight wire lengths (Chapters 3 and 4) and a single ring of wire (Chapter 5). In Chapter 3, we studied the magnetostatic properties of a long wire parallel to the $\mathbf{B}_0$ field. In Chapter 4, we studied the magnetostatic properties of a long wire perpendicular to the $\mathbf{B}_0$ field. In Chapter 5, we studied the magnetostatic properties of a ring of wire where the axis of the ring was perpendicular to the $\mathbf{B}_0$ field.

In the experiments that followed, the linewidth performance was assessed in homogeneous and probe-specific shimmed fields (refer "Magnetic Field Protocols, §3.4.3). The best results came from the parallel wire probe (Chapter 3), with a full width at half maximum of 1.05Hz and an associated signal-to-noise of 600 in a homogeneous field, and a full width at half maximum of 0.60Hz and an associated signal-to-noise of 20 in a probe-specific shimmed field.

Signal-to-noise was observed in the spectrum corresponding to the solenoid probe built with susceptibility-reduced copper-plated aluminium wire (Chapter 5). In a shimmed field, the full width at half maximum was 5.6Hz with an associated signal-to-noise of 5660. Honourable mention should go to another result obtained with the parallel wire probe, where the full width at half maximum was 5.5Hz with a signal-to-noise of 1930. (Note: all signal-to-noise values are merely observed during data analysis and should be interpreted not as the limits of the design, but as indicators only. Optimal filters can improve signal-to-noise

performance.) Linewidth and signal-to-noise performance for the probe designs of Chapters 3-5 are summarized in Table 6.1. As we can see from this summary, the parallel wire probe design gives the best linewidth performance, while the solenoid design with susceptibility-reduced wire gives the best signal-to-noise performance.

Table 6.1. Review of probe performance results from the 3 designs presented in this thesis. Entries marked with an asterisk represent the best resolution obtained with that particular design (and the observed signal-to-noise).

Probe Design	**Resolution (*FWHM*)**	**SNR**
Parallel wire probe (refer Fig. 3.2b)	1.5 ppb*	20:1
Parallel wire probe (refer Fig. 3.2a)	14 ppb	2000:1
Perpendicular wire probe (refer Fig. 4.31) (half-loop result)	50 ppb*	1860:1
Solenoid winding probe (refer Fig. 5.5)	14 ppb*	5660:1

Other technical highlights

In the development of the probes described in this thesis, several novel techniques have been developed. All of these are new contributions to the body of NMR physics knowledge and have not been previously reported or published in the literature.

Firstly, there is the magnetostatic property of a long straight wire applied in a NMR application. This surprisingly simple design allows the measurement of very narrow spectral linewidths in homogenous and inhomogeneous magnetic fields. The parallel wire probe can also be constructed with ordinary copper wire as opposed to something more involved like susceptibility-reduced wire.

Secondly, susceptibility-reduced co-axial wire has been developed in this work, and demonstrated to be of benefit in the construction of solenoid RF coils. The electroplating procedure, with the exception of one step involving a cyanide-based solution, is fairly straightforward and can be accomplished in any modestly equipped lab (with a fume hood just in case!). The wire has an effective zero magnetic susceptibility when it is oriented perpendicular to the $\mathbf{B}_0$ field.

Lastly, the co-axial wire developed in Chapter 4 does not exhibit zero susceptibility behaviour when it is wound as a ring or solenoid. This was shown by calculating the magnetostatic perturbation along the axis of a ring made of a co-axial wire. This calculation demonstrates that the dimensions appropriate for co-axial zero-susceptibility wire oriented in a uniform $\mathbf{B}_0$ field (Chapter 4) are not suitable when the wire is used in a ring geometry.

Future directions

Further testing of materials, e.g. capacitors, would be possible with a new probe that is fundamentally built around the long parallel wire probe of Chapter 3. In a homogeneous field we could examine the magnetostatic nature/effect of test components by bringing them close to the active volume of the NMR sample. Further work on zero-susceptibility wire for use with a solenoid winding is also warranted to obtain the best linewidth without compromise to achievable signal-to-noise.

BIBLIOGRAPHY

Abragam, A. (1961). The Principles of Nuclear Magnetism. Oxford, Oxford Univeristy Press.

Abramowitz, M. and I. A. Stegun (1964). Handbook of Mathematical Functions with Formulas, Graphs, and Mathmatical Tables. Washington, National Bereau of Standards.

Anderson, W. A. and J. N. Shoolery (1963). Gyromagnetic resonance method and apparatus. United States, Varian Associates.

Arnold, J. T. (1956). "Magnetic resonances of protons in ethyl alcohol." Physical Review **102(1)**: 136-150.

Belorizky, E., M. Gorecki, et al. (1990). "Sample-shape dependence of the inhomogeneous line broadening and line shift in diamagnetic liquids." Chemical Physics Letters **175 (6)**: 579-584.

Bevington, P. R. (1969). Data reduction and error analysis for the physical sciences. New York, McGraw-Hill Book Company.

Binns, K. J., P. J. Lawrenson, et al. (1992). The analytical and numerical solution of electric and magnetic fields. Toronto, John Wiley & Sons.

Bloch, F. (1946). "Nuclear induction." Physical Review **70(7,8)**: 460-474.

Bloch, F., W. W. Hansen, et al. (1946). "Nuclear Induction." Physical Review **69**: 127.

Bloch, F., W. W. Hansen, et al. (1946). "The nuclear induction experiment." Physical Review **70(7&8)**: 474-485.

Boikess, R. S. and E. Edelson (1981). Chemical Principles. New York, Harper Row.

Burachynsky, V. and J. R. Cahoon (1997). "A theory for solute impurityu diffusion, which considers Engel-Brewer valances, balancing the Fermi energy levels of solvent and solute, and differences in zero point energy." Metallurgical and Materials Transactions A **28A**: 563-582.

Callaghan, P. T. (1991). Principles of nuclear magnetic resonance spectroscopy. New York, Oxfor University Press Inc.

Chen, C.-N. and D. I. Hoult (1989). Biomedical Magnetic Resonance Technology. Bristol, England, Adam Hilger.

Conover, W. W. (1984). Pratical gide to shimming superconducting NMR magnets. Topics in Carbon-13 NMR Spectroscopy. G. C. Levy. New York, Wiley. **4:** 37-51 (Ch.2).

Cope, P. (1994). Susceptibilty of Wilmad Glass NMR tubes.

Doty, D. (1999). Susceptibilty compensated wire.

Doty, D. F. (1996). Probes design and construction. Encyclopedia of nuclear magnetic resonance. D. M. Grant and R. K. Harris. Chichester, England, John Wiley & Sons Ltd.: 3753-3762.

Ernst, R. R., G. Bodenhausen, et al. (1992). Principles of nuclear magnetic resonance in one and two dimensions. New York, Oxford University Press Inc.

Figgis, B. N. and J. Lewis (1965). Magnetochemistry. Technique of Inorganic Chemistry. H. B. Jonassen and A. Weissberrger, Interscience Publishers. **4:** 137-248.

Flynn, C. P., D. A. Rigney, et al. (1967). "Magnetic Plarization of transitional impurities in aluminum." Phil. Mag. **15**: 1255-1273.

Fuks, L. F., F. S. C. Huang, et al. (1992). "Susceptibility, lineshape, and shimming in high-resolution NMR." Journal of Magnetic Resonance **100**: 229-242.

Fukushima, E. and S. B. W. Roeder (1979). "Spurious ringing in pulse NMR." Journal of Magnetic Resonance **33**: 199-203.

Germain, C. (1963). "Bibliographical review of the methods of measuring magnetic fields." Nuclear Instruments and Methods **21**: 17-46.

Gerothanassis, I. P. (1987). "Methods of avoiding the effects of acoustic ringing in pulsed fourier transform nuclear magnetic resonance spectroscopy." Progress in NMR Spectroscopy **19**: 267-329.

Grant, I. S. and W. R. Phillips (1975). Electromagnetism. New York, John Wiley & Sons.

Group, P. D. (1998). "Review of Particle Physics." The European Physical Journal **3**(1-4): 9-12.

Hauser, W. (1971). Introduction to the Principles of Electromagnetism, Addison-Wesley Publishing Company.

Henry, W. G. and J. L. Rogers (1956). "The magnetic susceptibilities of copper, silver, and gold and error in the Gouy method." Philosophical Magazine **1**: 223-236.

Hill, H. D. W. (1996). Probes for High Resolution. Encyclopedia of Nuclear Magnetic Resonance. D. M. Grant and R. K. Harris. Chichester, West Sussex, John Wiley & Sons Ltd. **6**.

Hill, H. D. W. (1996). Spectrometers: A general overview. Encyclopedia of nuclear magnetic resonance. D. M. Grant and R. K. Harris. West Sussex, England, John Wiley & Sons Ltd.: 4505-4518.

Hoult, D. I. (1978). "The NMR receiver: a description and analysis of design." Progress in NMR Spectroscopy **12**: 41-77.

Hoult, D. I. (1996). Sensitivity of the NMR experiment. Encyclopedia of nuclear magnetic resonance. D. M. Grant and R. K. Harris. Chichester, England, John Wiley & Sons Ltd.: 4256-4266.

Hoult, D. I. and B. Bhakar (1997). "NMR Signal Reception: Virtual photons and coherent spntaneous emmision." Concepts in Magnetic Resonance **9(5)**: 277-297.

Hoult, D. I., C. N. Chen, et al. (1983). "Elimination of baseline artifacts in spectra and their integrals." Journal of Magnetic Resonance **51(1)**: 110-117.

Hoult, D. I. and N. S. Ginsberg "The quantum origins of the free induction decay signal and spin noise." Journal of Magnetic Resonance.

Hoult, D. I. and P. C. Lauterbur (1979). "The sensitivity of the Zeugmatographic experiment involving human samples." Journal of Magnetic Resonance **34**: 425-433.

Hoult, D. I. and R. E. Richards (1976). "The signal-to-noise ratio of the nuclear magnetic resonance experiment." Journal of Magnetic Resonance **24**: 71-85.

Hurd, C. (1966). "The magnetic susceptibility of silver and gold in the range of 6-300K." Journal of Physics and Chemistry of Solids **27**: 1371-1374.

Jackson, J. D. (1975). Classical Electrodynamics. Toronto, John Wiley and Sons.

Kellogg, J. M. B., I. I. Rabi, et al. (1939). "The magnetic moments of the proton and hte deuteron. (The radiofrequency spectrum of H2 in various magnetic fields)." Phys. Rev. **56**: 728-743.

Kittel, C. (1971). Ontroduction to Solid State Physics. New York, John Wiley & Sons.

Lacey, M. E., R. Subramanian, et al. (1999). "High-resolution NMR spectroscopy of sample volumes from 1nL to 10uL." Chemical Reviews **99**(10): 3133-3152.

Landau, L. D. and E. M. Lifshitz (1984). Electrodynamics of Continuous Media. Oxford, England, Pergamon Press.

LeClaire, A. D. (1983). Diffusion in Metals. Smithells Metals Reference Handbook. E. A. Brandes. London, Butterworths.

Lyman, T. (1973). Metallography, Structures and Phase Diagrams. Metals Park, Ohio, American Society for Metals.

Lyons, L. (1986). Statistics for Nuclear and Particle Physicists. Cambridge, Cambridge Univerisity Press.

Moon, P. and D. E. Spencer (1971). Field Theory Handbook: Including Coordiante Systems, Differential Equations and their Solutions. New York,NY, Spinger-Verlag.

Morse, P. M. and H. Feshbach (1953). Methods of Theoretical Physics. New York, Mcgraw-Hill Book Company, Inc.

Ohanian (1988). Classical Electrodynamics. Boston, Allyn and Bacon, Inc.

Olson, D. L., T. L. Peck, et al. (1995). "High-resolution microcoil 1H-NMR for mass-limited, nanoliter volume samples." Science **270**: 1967-1970.

Parthasaradhy, N. V. (1989). Practical Electroplating Handbook. New Jersey, Prentice Hall.

Peck, T. L., R. L. Magin, et al. (1994). "NMR microscopy using 100um planar RF coils fabricated on gallium arsenide substrates." IEEE Transactions on Biomedical Engineering **41**(7): 706-709.

Peck, T. L., R. L. Magin, et al. (1995). "Design and analysis of microcoils for NMR microscopy." Journal of Magnetic Resonance, Series B **108**: 114-124.

Purcell, E. M., H. C. Torey, et al. (1946). "Resonance absorption by nuclear magnetic moments in a solid." Physical Review **69**: 37,38.

Romeo, F. and D. I. Hoult (1984). "Magnetic Field Profiling: Analysis and correcting coil design." Magnetic Resonance in Medicine **1**: 44-65.

Segre, E. (1977). Nuclei and Particles. New York, Addison-Wesley Publishing Company, Inc.

Shewmon, P. G. (1963). Diffusion in Solids. New York, McGraw-Hill Book Company, Inc.

Simpson, R. E. (1987). Introductory Electronics for Scientists and Engineers. Boston, Allyn and Bacon, Inc.

Slichter, C. P. (1992). Principles of magnetic resonance. New York, Springer-Verlag.

Symonds, J. L. (1955). "Methods of measuring strong magnetic fields." Reports on Progress in Physics **18**: 83-126.

Unger, P. P. and D. I. Hoult (1997). Zero susceptibility wire for the construction of high resolution of NMR mircocoils. International Society for Magnetic Resonance in Medicine, Fifth Scientific Meeting and Exhibition, Vancouver, British Columbia, Canada, ISMRM.

Unger, P. P. and D. I. Hoult (1999). A simple NMR probe for magnetic field measurements. International Society for Magnetic Resonance in Medicine, Seventh Scientific Meeting and Exhibition, Philadelphia, Pennsylvania, USA, ISMRM.

Vogt, E. (1933). "Zum Dia- und Paramagnetismus in metallischen mischkristallreihen." Annalen der Physik **18(5)**: 771-790.

Walden, R. H. (1999). "Analog-to-digital converter survey and analysis." IEEE Journal on Selected Areas in Communications **17**(4): 539-550.

Weast, R. C. (1987). CRC handbook of chemistry and physics. Boca Raton, Florida, CRC Press, Inc.

Webb, A. G. and S. C. Grant (1996). "Signal-to-Noise and magnetic susceptibility trade-offs in solenoidal microcoils for NMR." Journal of Magnetic Resonance, Series B **113**: 83-87.

White, R. L. (1992). "Giant Magnetoresistance: A primer." IEEE Transactions on Magnetics **28**(5): 2482-2487.

Zelaya, F. O., S. Crozier, et al. (1995). "Measurement and compensation of field inhomogeneities caused by differences in magnetic susceptibility." Journal of Magnetic Resonance, Series A **115**: 131-136.